

The Pennsylvania State University

The Graduate School

ELASTODYNAMIC AND MECHANICAL PROPERTIES OF SMECTITE-RICH FAULT

GOUGE

A Dissertation in

Geosciences

by

Abby R. Kenigsberg

© 2019 Abby R. Kenigsberg

Submitted in Partial Fulfillment

of the Requirements

for the Degree of

Doctor of Philosophy

December 2019

The dissertation of Abby R. Kenigsberg was reviewed and approved* by the following:

Demian Saffer
Department Head and Professor of Geosciences
Dissertation Co-Advisor
Chair of Committee

Chris Marone
Professor of Geosciences
Dissertation Co-Advisor

Charles Ammon
Professor of Geosciences

Parisa Shokouhi
Associate Professor of Engineering Science and Mechanics

Jacques Rivière
Associate Professor of Engineering Science and Mechanics

Mark Patzkowsky
Professor of Geosciences
Associate Head for Graduate Programs and Research

*Signatures are on file in the Graduate School

ABSTRACT

Shear fabrics and smectite clay-rich gouges have been found to cause significant weakening in major crustal faults, increasing the seismic hazard of fault zones such as the San Andreas Fault. While the effects of shear fabrics throughout shear in smectite rich gouge on mechanical properties are well studied, the role that these fabrics play in controlling elastic properties and permeability of fault gouge remains unclear. In this study, I focus on the role that shear fabrics and smectite rich gouge composition play on elastic and mechanical properties by running and evaluating experiments using a biaxial stress apparatus as well as an ultrasonic pulsing system. For a subset of experiments, I follow this procedure within a pressure vessel to determine the evolution of permeability and elastic properties as fabrics form. Throughout the experiments in this study, I am able to measure and/or calculate a combination of the coefficient of friction, degree of fabric formation, porosity evolution, permeability evolution, elastic wavespeeds, and elastic moduli to ultimately understand how fabric formation affects important fault properties such as fault stiffness and sliding stability.

While it is difficult to measure absolute wavespeeds in our experimental set up, it is vital that we are able to obtain them as that allows us to directly apply our results to field data and in situ conditions. We developed a new method to calibrate our system which allows us to calculate absolute V_p and V_s and, therefore, bulk (K) and shear (G) modulus throughout shear. Using this method, we were able to run experiments on gouge composed of 50% smectite mixed with 50% granular quartz and calculate V_p , V_s , K , and G to determine what micromechanical processes were controlling the evolution of elastic properties. We found that, though porosity loss is often cited as the dominate control of elastic properties, shear fabrics can temporarily dominate both the mechanical and elastic response of smectite rich gouge to shear if fabrics are preferentially oriented perpendicular to the direction of elastic wave propagation, causing a

mechanical weakening via the coefficient of friction as well as a decrease in elastic properties and stiffness even as porosity is lost. This has implications for assessing fault stiffness and sliding stability as well as interpreting seismic data and brings to light the need to consider shear fabrics when assessing fault stability and structure.

To determine the extent of control that fabrics have on mechanical and elastic properties, we conducted further experiments on smectite rich gouges that ranged from 10% - 100% smectite mixed with granular quartz as well as experiments with input sediment from off the coast of Sumatra obtained during IODP (Integrated Ocean Drilling Program) expedition 362. Previous studies have indicated that a larger amount of smectite leads to more pervasive fabric formation, in agreement with our results. We found that, in some cases with high amounts of smectite, fabrics almost entirely controlled the mechanical *and* elastic response of gouges at all shear strains causing dramatic weakening of the gouge paired with decreasing elastic properties even as porosity is lost. We also found that even at low percentages of smectite, gouges are temporarily controlled by fabric formation as is evidenced by gouge weakening as well as decreasing elastic properties. Furthermore, based on the IODP samples from Sumatra, we discovered that smectite percentage, not clay or phyllosilicate percentages, largely controls the mechanical and elastic response to shear.

Though many studies have hypothesized that fabric formation may be a control of permeability reduction during shear, few have directly tried to link the two properties. We conducted experiments to link permeability, the coefficient of friction, and ultrasonic property changes throughout shear to confirm that shear fabrics are a primary control of permeability reduction. Not only did we observe that shear fabrics are one of the main controls of permeability reduction, but we also determined that ultrasonic amplitudes can be used in concert with the coefficient of friction to track fabric formation. This has important implication for faults in

natural settings as we have determined that not only does the amount of smectite within the fault gouge control the permeability, but the maturity and development of the shear fabrics are also a very important characteristic to consider when evaluating fault zone permeability.

Collectively, the results from these experiments provide insight into the roles that shear fabric and gouge composition play in controlling mechanical and elastic properties and, therefore, important fault properties such as fault stiffness and hazard assessment. We found that shear fabrics control the mechanical and elastic properties of smectite rich fault gouges to different degrees depending largely, if not solely, on the amount of smectite within the gouge. We also determined that, when analyzing fault zone permeability, smectite content and maturity of shear fabrics in a fault zone are vital controls. Overall, this is extremely important when processing seismic data as it indicates that fabrics could cause lower velocities than expected. Fabrics should also be considered when determining seismic hazard risks in general as they can greatly weaken the fault system. These results have serious implications for understanding the micromechanical processes and large scale fault properties in natural fault systems.

TABLE OF CONTENTS

LIST OF FIGURES	viii
LIST OF TABLES	xiv
ACKNOWLEDGEMENTS.....	xv
Chapter 1 Introduction	1
Chapter 2 A Method for Travel Time Calibration and Determination of Absolute Ultrasonic Velocities in Experimental Shear Zones	7
2.1 Abstract	7
2.2 Introduction	8
2.3 Methods.....	10
2.3.1 Experimental Configuration and Materials.....	10
2.3.2 Ultrasonic Measurements and Travel Time Calculations.....	11
2.4 Calibration Method for Travel Times and Absolute Velocities	13
2.4.1 Travel Time Corrections.....	13
2.4.2 Velocities and Errors	15
2.5 Discussion and Conclusions.....	16
Chapter 3 The Effects of Shear Strain, Fabric, and Porosity Evolution on Elastic and Mechanical Properties of Clay-Rich Fault Gouge.....	30
3.1 Abstract	30
3.2 Introduction	31
3.3 Materials and Methods.....	34
3.3.1 Experimental Configuration for Shearing and Friction Measurements	34
3.3.2 Computation of mass loss and porosity	35
3.3.3 Ultrasonic velocity measurements.....	37
3.3.4 SEM Imaging and High-Resolution X-ray CT Scans.....	39
3.4 Results.....	40
3.4.1 Evolution of friction, porosity, and layer thickness.....	40
3.4.2 Ultrasonic velocities	41
3.4.3 SEM and CT scan shear fabric observations.....	42
3.5 Discussion	43
3.5.1 Evolution of friction and wavespeeds.....	44
3.5.2 Elastic moduli and fabric development	45
3.5.3 Implications for Shear Fabrics and Micromechanical Processes	48
3.6 Conclusions	50
Chapter 4 Evolution of Elastic and Mechanical Properties during Fault Shear: The Roles of Clay Content, Fabric Development, and Porosity	63
4.1 Abstract	63

4.2 Introduction	64
4.3 Materials and Methods.....	66
4.3.1 Shearing Experiments.....	66
4.3.2 Mass Loss and Porosity Calculations	68
4.3.3 Ultrasonic Velocities and Elastic Moduli	70
4.4 Results.....	71
4.4.1 Coefficient of Friction	71
4.4.2 Ultrasonic Velocities and Elastic Moduli	72
4.5 Discussion	74
4.5.1 Friction Strength and Stress-strain Behavior	74
4.5.2 Porosity Reduction, Fabric Evolution, and Elastic Properties	76
4.5.3 Shear Planes and Clays in Natural Fault Gouges	79
4.6 Conclusions	79
 Chapter 5 Evolution of Permeability During Shear of Fault Gouge: Effects of Composition and Fabric.....	 93
5.1 Abstract	93
5.2 Introduction	94
5.3 Materials and Methods.....	96
5.3.1 Friction Measurements and Permeability Tests	96
5.3.2 Ultrasonic Measurements	98
5.4 Results.....	98
5.4.1 Friction and Permeability Evolution as a Function of Clay Content and Shear Strain.....	98
5.4.2 Ultrasonic Amplitudes.....	100
5.5 Discussion	100
5.5.1 Coevolution of Permeability, Friction, and Amplitude	100
5.5.2 Implications for Fault Hydraulic and Mechanical Processes	103
5.6 Conclusions	103
 References	 112

LIST OF FIGURES

Figure 2-1: Left: Schematic of biaxial stress apparatus and double direct shear (DDS) sample. Right: Schematic of steel blocks and gouge samples with piezoelectric transducers (PZTs) in black.	19
Figure 2-2: Coefficient of friction and layer thickness changes with shear strain. Layer thickness changes are accounted for when calculating velocities and calibrations.	19
Figure 2-3: Example waveform in a.u., arbitrary units, from p4912 (50% smectite / 50% granular quartz). Mean (black line), ± 1 standard deviation (green line), and ± 2 standard deviation (red line) are calculated based on a portion of the waveform right before the P-wave arrival and then again right before the S-wave arrival. When the waveform crosses the 2 standard deviation red line, the arrival time is picked at the zero crossing of the mean line (black) before the signal crossed the red line.	20
Figure 2-4: Example P-wave arrival times vs layer thickness of two layers for shear strains of 2, 6, 12, and 17. At a shear strain of 2, the arrival time is much slower. However, the lines converge at higher shear strains and all have similar P-wave arrival times. Bottom: 50% smectite 50% quartz example of a calibration curve. The red envelope is \pm RMSE. The pink, blue, red, and green points correspond to the lines in the top portion of this figure for shear strains of 2, 6, 12, and 17.	21
Figure 2-5: P-wave and S-wave calibration curves for 10%, 30%, 50%, 70%, 90%, and 100% smectite synthetic mixtures as well as two natural, Sumatra samples (dotted lines). For the most part, by a shear strain of ~ 4 , the calibration curves reach a steady state. The dots on each line represent zero thickness arrival time at the given shear strain as shown in the top portion of figure 2-4.	22
Figure 2-6: Uncalibrated and calibrated P-wave arrival times. The calibrated times are calculated by subtracting the "zero gouge thickness" value obtained from the calibration curve from the uncalibrated arrival time.	23
Figure 2-7: Uncalibrated and calibrated S-wave arrival times. The calibrated times are calculated by subtracting the "zero gouge thickness" value obtained from the calibration curve from the uncalibrated arrival time.	24
Figure 2-8: Absolute velocity achieved through the calibration process for p4912, 50% smectite. The red envelope represents the error imposed by the RMSE from figure 2-4.	25
Figure 2-9: P- and S- wave absolute velocities for all synthetic smectite gouge mixtures as well as the Sumatra samples.	26
Figure 3-1: Left: Schematic of biaxial deformation apparatus with double direct shear sample. Right: Double direct shear sample with ultrasonic cables connected to piezoelectric transducers.	52

- Figure 3-2: Example waveform from experiment p4830. P and S wave arrivals times are picked at the zero-crossing (relative to the signal mean, black line). A master wave is picked for each experiment and the evolution of arrival times as a function of shear are determined via cross correlation. 53
- Figure 3-3: Travel times for P- and S-waves through two layers of fault gouge. These data are determined from waveforms (Figure 3-2) and calibrations to account for the travel time through the loading platens and sample assembly. Note that wave speed increases rapidly during initial shear, up to strain of ~ 3 , due to shear enhanced gouge compaction and then evolves more gradually with strain. Gaps in the data are associated with mechanical offsets of the experimental apparatus. 54
- Figure 3-4: Coefficient of friction, porosity, and layer thickness as a function of shear strain for three complete experiments. Changes in porosity mirror changes in the coefficient of friction, showing rapid evolution followed by gradual changes. Gouge layers thin rapidly upon initial shear and then exhibit steady state thinning associated with geometric spreading. 55
- Figure 3-5: Data for three complete experiments showing four stages of evolution in friction and elastic wave speed. Stage 1 (red) shows an increase in all properties during shear loading. Stage 2 (black) begins when friction first decreases after the peak strength, which coincides with increases in V_p , V_s , and V_p/V_s that are interpreted to result from shear fabric formation. Stage 3 (green) begins at the peak value of V_p and occurs during frictional weakening which is interpreted to result from fabric intensification and alignment parallel to the shear direction. The beginning of Stage 4 (gray), is defined when V_p begins increasing again. In State 4, friction has reached a steady state value and wave speeds increase as the layer compacts and densifies. 56
- Figure 3-6: Left: Images of sheared wafers at peak friction (at the onset of stage 2). Right: Images of sheared wafers at residual friction. The top image on the left and right is modified from Haines et al., 2013 and is an image of sheared chlorite schist sheared at a normal stress of 20 MPa and shearing velocity of $\sim 11 \mu\text{m/s}$. The middle two images are SEM images of sheared wafers from experiments in this study (p4915 and p4913). The bottom images are also from p4915 and p4913 and are CT scans of the same face that is shown in the middle images. Quartz grains are highlighted in red. The top two images on the left and right show possible shear planes evolving with shear. The left images, before peak friction and at the onset of stage two show the formation of a few Riedel shears as shown by the red arrows. The CT scan shows large aggregates of smectite forming, indicating that while there are likely some fabrics, they are not throughgoing enough for all of the clay in the sample to line them. The right images, at residual friction, show many shear planes as shown by the red arrows. As these fabrics rotate more perpendicular to the direction of wave propagation and become more through-going, they cause a decrease in the ultrasonic velocities. The CT scan of p4913 shows that the clay has smeared throughout the sample and is likely lining throughgoing fabrics. 57

- Figure 3-7: Evolution of elastic wave speeds with porosity for three complete experiments, showing the four stages defined in Figure 3-5. The dashed blue curves show V_p and V_s evolution as a function of change in porosity for an experiment (p5243) where only normal stress was increased (0 - ~65 MPa) and there was no shear. Therefore, the trend shown in the blue curves is the change in velocity due only to compaction. Any trend that deviates from p5243 indicates that processes other than compaction are occurring. Both V_p and V_s increase during porosity reduction except for Stage 3 (green). The reduction in V_p and V_s during bulk gouge densification (Stage 3) suggests that shear fabric formation can reduce elastic modulus or density locally within the shear bands. 58
- Figure 3-8: Shear and bulk modulus as a function of shear stress showing the four stages defined in Figure 3-5. Evolution of the moduli provide insight into micromechanical processes within the layer. Bulk and shear modulus are relatively constant during Stage 1 and then begin to increase as grains rearrange and contact quality and quantity increase. Stage 2 exhibits an increase in bulk and shear modulus as fabrics initially develop and force chains form. Increased fabric formation also may enhance grain contacts. Stage 3 displays the only decrease in shear and bulk modulus as fabrics become more pervasive and longer force chains formed in Stage 2 begin to break down, decreasing the stiffness and rigidity of the layer. Stage 4 exhibits a large increase in shear and bulk modulus as fabrics become more pervasive and the layer further compacts, creating an increase in grain contact quantity and quality. 59
- Figure 3-9: After Haines et al., 2013 and Logan and Rauenzahn, 1987. Hypothesized micromechanical processes occurring with the gouge layer during shear. During stage 1 (red) few fabrics have formed and grains are reorganizing during shear stress load up. Compaction controls the mechanical and elastic responses of stage 1. Stage 2 (black) begins at peak friction and marks the onset of Riedel shears, boundary shears, and Y-shears, causing a decrease in the coefficient of friction. It is possible that long, compliant force chains form during stage 2. While fabric formation weakens the coefficient of friction and controls mechanical properties, compaction still controls elastic properties. During stage 3 (green), we observe further weakening within the layer causing a decrease in V_p and V_s as Riedels, P-shears, boundary shears, and Y-shears grow throughout the layer rotate to become perpendicular to the direction of wave propagation. The evolution of fabrics controls both mechanical and elastic properties during stage 3. Stage 4 (gray) marks steady state friction and a continuous increase in V_p and V_s as Riedels, Y-shears, and boundary shears are throughgoing and well developed. Further compaction controls the mechanical and elastic properties of stage 4. 60
- Figure 4-1: Left: Schematic of the biaxial shear apparatus and double direct shear sample. Right: Schematic of the double direct shear configuration with piezoelectric transducers within the side blocks (black rectangles). 82
- Figure 4-2: Example waveform in a.u., arbitrary units (p4830 - 50% smectite/50% quartz). P- and S-wave arrivals are picked at the zero crossing (black line) right before the signal has exceeded 2 standard deviation of the noise (red line). 83

- Figure 4-3: The coefficient of friction and change in porosity as a function of shear strain. The coefficient of friction decreases with increasing clay content in synthetic gouge mixtures. High smectite mixtures (50% and greater) exhibit a distinctive peak and subsequent decay due to fabric formation. Porosity decreases throughout the entire experiment for all mixtures. Porosity decreases most rapidly before peak friction and fabric formation and then reaches as steady state decrease as fabrics are formed. 100% and 90% smectite exhibit a more rapid decrease in porosity than other mixtures at intermediate shear strains (~0-8). 84
- Figure 4-4: Absolute P- and S-wave velocities as a function of shear strain. In general, velocities decrease with increasing clay content. Decreases in velocities with increasing shear strain indicate that fabrics are controlling velocities as opposed to porosity loss. Due to the high portion of illite, the Sumatra sediments behave differently than the synthetic gouge mixtures. 85
- Figure 4-5: Shear and bulk moduli as a function of shear strain. High smectite synthetic gouge mixtures primarily exhibit decreasing elastic moduli as fabrics are weakening the gouges. Low smectite synthetic gouges have short periods of decrease due to optimally oriented fabrics, but are primarily controlled by porosity loss and shear enhanced compaction as is shown by the increasing elastic moduli. The Sumatra sediments exhibit increases in elastic moduli except for the shear modulus of one of the samples indicating that fabrics may be pervasive as high shear strains for this sample. 86
- Figure 4-6: The coefficient of friction, V_p , V_s , and bulk (K) and shear (G) modulus as a function of smectite percentages at a shear strain of 0, local peak coefficient of friction (immediately after shear stress load up) and velocity/modulus, and at a shear strain of 20. Low smectite gouge mixtures exhibit an increase in the coefficient of friction (green arrow indicates increasing shear strain), V_p , V_s , K and G as a function of shear strain whereas high smectite synthetic gouge mixtures exhibit a decrease in V_p , V_s , and the coefficient of friction (green arrow indicates increasing shear strain) as a function of shear strain due to fabrics weakening the gouge. K and G reach a peak and then decrease by a shear strain of 20. The Sumatra samples largely behave similarly to the low smectite synthetic gouge samples with the exception of V_s and G of the Sumatra sample with 19% smectite. 87
- Figure 4-7: P-wave velocity as a function of change in porosity. Shear strain is increasing as porosity is reducing. Changes in ultrasonic velocity throughout shear are generally attributed to porosity loss and compaction. The thick black line shows the compaction trend for an experiment (p5243) that was only compacted and was not sheared. However, we observe a deviation from this trend for our sheared experiments with decreases in velocity even as porosity decreases indicating that another processes in controlling velocity. We interpret decreases in velocity as porosity decreases as periods in which fabrics are controlling the velocity. High smectite synthetic gouges largely exhibit decreasing velocities as porosity decreases, indicating that fabrics are controlling these gouges for the majority of shear. Low smectite synthetic gouges exhibit short term decreases in velocity. We attribute these decreases to periods in which fabrics are preferentially oriented perpendicular to the

- direction of wave propagation and, therefore, behave as barriers to the ultrasonic waves. The Sumatra sediments increase throughout shear indicating that they are largely controlled by porosity loss..... 88
- Figure 5-1: Left: Schematic of the biaxial shear apparatus and double direct shear sample inside of the true triaxial pressure vessel. Top Right: Schematic of the pressure vessel with pore fluid and confining pressure lines shown. Piezoelectric transducers are shown within the side blocks – black rectangles - and rubber jackets to seal the samples are shown around the sample in yellow. Bottom right: Example waveform in a.u., arbitrary units (p5298 - 50% smectite/50% quartz). The amplitude is picked as the first peak amplitude after the P-wave arrival..... 105
- Figure 5-2: The coefficient of friction and permeability as a function of shear strain. Both the coefficient of friction and permeability decrease with increasing clay content. The coefficient of friction exhibits a local peak around a shear strain of 5, corresponding to the development of pervasive shear fabrics and then decays to a steady state value. The permeability decreases dramatically immediately after this local peak in the coefficient of friction and then also reaches a near steady state. This indicates that fabric formation is an important factor in decreasing permeability. 106
- Figure 5-3: Coefficient of friction (A), permeability (B), and normalized amplitude (C), as a function of smectite in the gouge at specified shear strains values. All three variables decrease with increasing smectite content and shear strain..... 107
- Figure 5-4: The shear stress divided by effective normal stress (our defined coefficient of friction) vs. permeability. Shear increases along the arrows. Permeability is nearly stable until peak friction where it quickly decreases. 108
- Figure 5-5: The top show shear strain vs. shear stress divided by effective normal stress (our defined coefficient of friction) and the bottom shows the coefficient of friction vs. normalized amplitude. Peak coefficient of friction (μ), peak amplitude, and the onset of steady state μ are shown on both plots with the black and gray points. The bottom plot is colored based on shear strain values. At the initiation of shear during the shear stress load up, μ is increasing whereas the amplitude is relatively stable. This is because the layer is stiffening as grains are rearranging. As shear continues and the peak μ is approached, amplitude slowly starts to increase. After peak μ , pervasive fabric formation is initiated causing a decrease in μ . However, the fabrics are not yet pervasive enough to control the amplitude as the amplitude still increases as the layer compacts (figure 5-7). As μ continues to decrease due to continued fabric formation and evolution, amplitude finally reaches a peak as the fabrics become pervasive enough to control the response of amplitude as the fabrics are rotating near perpendicular to the direction of ultrasonic wave propagation. As the fabrics continue to evolve and rotate, the coefficient of friction reaches steady state values while the increasing complexity and geometry of the shear fabrics causes the amplitude to decrease significantly. 109
- Figure 5-6: The coefficient of friction and normalized amplitude as a function of shear strain. The trend of the normalized amplitude largely mimics the coefficient of

friction. However, there is a slight delay in the peak and decay of amplitude relative to the coefficient of friction as the shear fabrics become more pervasive and cause a decrease in the amplitude after the initial fabric formation which causes a decrease in the coefficient of friction. Amplitude decreases with increasing clay content.

(Supplementary figure in publication draft)..... 110

Figure 5-7: Single layer thickness in millimeters as a function of shear strain. During initial shear, layer thickness changes slowly. However, once the peak coefficient of friction is reached and fabrics form, layer thickness decreases more rapidly.

(Supplementary figure in publication draft)..... 111

LIST OF TABLES

Table 2-1 : List of Experiments	27
Table 3-1 : List of experiments, including calibration experiments (bolded experiment numbers are shown in the figures).....	61
Table 4-1 : List of Experiments	89

ACKNOWLEDGEMENTS

First and foremost I thank my mom, dad, sisters and brother, my partner Shelby Lyons, my best friend Beth Hoagland, and my dog Kirby for their endless patience, love, and support. There is no doubt in my mind that I would not have finished my Ph.D. without them. I have depended on them endlessly, whether it was to talk for hours about the many frustrations of graduate work or to help distract me from the stresses that a Ph.D. comes with. Thank you all for letting me always count on you as my support system. I love y'all.

I would like to thank my co-advisors, Demian Saffer and Chris Marone, for their support and guidance. They both constantly challenged me and helped me to grow as a scientist and I have them to thank for getting me to the end of this degree. They both always encouraged and supported me, even when I utilized a rifle cleaner in lab to obtain porosity measurements. Thank you for your patience over the last 5 years.

I also have to thank my committee, Charles Ammon, Parisa Shokouhi, and Jacques Rivière. I was lucky enough to have a committee that was truly involved in all aspects of my dissertation and graduate work. I thank my committee for always providing feedback and stepping in to help any time I needed it. The help they provided through exams, lab work, and draft discussions were invaluable.

I owe much of my success in lab to Steve Swavely and my labmates over the years. I thank Steve for the enormous amount of patience he needs to help us on a day to day basis. Our lab certainly couldn't function without him. I would not have even been able to run the biax without the careful teachings and patient friendship of Kerry Ryan, even if she drank my coffee sometimes in lab. In addition, I thank Kerry for being my teammate in the chili cook-off that we won 5 years in a row. I thank Chas Bolton and Sharan for being such amazing sounding boards and for always letting me come into their office, shut the door, and talk endlessly about

whatever it was I needed to get off my chest. I thank Clay Wood for your guidance and help with running experiments, even if it was against your will. I owe you duck donuts for life. I thank Ben Madara, Tim Witham, Peter Miller, Alex Santos, John Leeman, and Katie Carroll for their friendship, entertainment, and help both in the beginning and end of my Ph.D.

Finally, I cannot stress enough how much how important my grad school family has been throughout the years. There is no way I could have made it through without such a great support system around me at all times. Thank you to my PSU fellow grad students and alumni. Specifically, thank you to Virginia Marcon, Helen Gall, Victoria Fortiz, Jen Estrada, Zena Cardman, Kendall Wnuk, Austin White-Gaynor, Nana Bear Xu, Perry Oddo, Jamie Neely and many many more. You've all been a shoulder to lean on at various points throughout the last 5 years.

This dissertation was supported by multiple funding sources including the NSF U.S. science support program post expedition award, the DOE geothermal program (DOE EERE DE-EE0006762), the NSF geophysical program (NSF awards EAR-1215856, EAR-1520760, and EAR-1547286/1547441), the Geological Society of America graduate research grant, the Chevron graduate student scholarship, the ConocoPhillips graduate student fellowship, the Shell geosciences energy facilitation award and the GDL foundation fellowship.

Chapter 1

Introduction

The low mechanical strength of major crustal faults remains a fundamental problem in geophysics and earthquake mechanics. This weakness has been explained in part by frictionally weak clays such as smectite (μ ranging from as low as $\sim 0.1 - 0.3$), which are abundant in many major fault zones (Wu et al., 1975; Wu, 1978; Wang et al., 1980; Morrow et al., 1984, 2017; Vrolijk and van der Pluijm, 1999; Kopf and Brown, 2003; Moore and Lockner, 2004; Ikari et al., 2007, 2009; Niemeijer et al., 2010; Tembe et al., 2010; Carpenter et al., 2011, 2012; Behn and Faulkner, 2013). In particular, smectite clay has been linked to fault weakness in both the San Andreas fault zone and the Tohoku-Oki earthquake (Wu et al., 1975; Carpenter et al., 2011, 2012; Ujiie et al., 2013; Wojatschke et al., 2016). Laboratory and field studies have also observed substantial frictional weakening in gouge and fault rocks due to the development of clay fabrics, shear plane development, and force chain evolution over a range of stresses, clay types, and humidity conditions (Wu et al., 1975; Wu, 1978; Saffer et al., 2001; Saffer and Marone, 2003; Niemeijer et al., 2010; Carpenter et al., 2012). As faults accommodate displacement and shear planes develop, clays align along shear surfaces, consequently causing macroscopic weakening.

Fictional weakness in clay minerals is commonly attributed to weak interlayer bonds (Summers and Byerlee, 1977) or the presence of water layers within the smectite chemical structure (Wu, 1978; Moore and Lockner, 2004). Haines et al. 2013 attributed clay-rich fault gouge weakness to additional factors, including particle morphology, development of Riedel shears and other shear planes, and fine grain size (Haines et al., 2013). The role and development of fabrics has been observed both directly, by using scanning electron microscope (SEM) or other techniques to image the development of shear planes (Haines et al., 2013), and indirectly, by

observing the coefficient of friction reach a peak value and then decay, as a result of fabric formation as shear progresses (Logan and Rauenzahn, 1987; Saffer and Marone, 2003; Ikari et al., 2009; Knuth et al., 2013; Haines et al., 2013).

In addition to mechanically weakening fault zones, clay alignment and fabric formation have been shown both in laboratory settings and natural faults to significantly decrease fault gouge permeability (Byerlee, 1990; Rice, 1992; Faulkner and Rutter, 2001; Moore and Saffer, 2001; Ikari et al., 2009; Behnsen and Faulkner, 2013; van der Elst et al., 2013; Ellsworth, 2013; Walsh and Zoback, 2015; McGarr et al., 2015; Segall and Lu, 2015; Elsworth et al., 2016). Decreased permeability due to increased clay alignment can in turn promote excess pore fluid pressure, which can further weaken faults, affect fault structure, and modulate the style of slip and updip limit of seismicity (Hubbert and Rubey, 1959; Knipe, 1992; Rice, 1992; Yielding et al., 1997; Faulkner and Rutter, 2001; Wibberley and Shimamoto, 2005; Segall and Rice, 2006; Vrolijk et al., 2016). Fault permeability is also a key parameter controlling induced seismicity due to waste water disposal, and reservoir compartmentalization and seal capacity (Byerlee, 1990; Rice, 1992; Faulkner and Rutter, 2001; Moore and Saffer, 2001; Ikari et al., 2009; Behnsen and Faulkner, 2013; van der Elst et al., 2013; Ellsworth, 2013; Walsh and Zoback, 2015; McGarr et al., 2015; Segall and Lu, 2015; Elsworth et al., 2016).

Directly observing the evolution of fabrics, strength, and permeability of faults in the subsurface can be challenging. Seismic waves have been widely used for probing fault zone mechanical (gouge composition, frictional strength, density, permeability) and elastic (V_p , V_s , bulk and shear moduli) properties, as they can provide insight into key processes and fault properties during shearing (Hadley, 1976; Nur et al., 1998; Popp and Kern, 1998; Jia et al., 1999; Schubnel et al., 2003; Fortin et al., 2005, 2007; Khidas and Jia, 2012; Knuth et al., 2013; Kaproth and Marone, 2014). In past studies, porosity loss and compaction have been cited as the dominant factors controlling the changes in ultrasonic and mechanical properties throughout

shear (Nur et al., 1998; Popp and Kern, 1998). However, recent studies have also suggested intergranular cracking, force chain development, and fabric formation as additional mechanisms controlling these properties (Hadley, 1976; Popp and Kern, 1998; Jia et al., 1999; Schubnel et al., 2003; Fortin et al., 2005, 2007; Khidas and Jia, 2012; Knuth et al., 2013; Kaproth and Marone, 2014). In particular, Fortin, Schubnel, and Guéguen, 2005 and Fortin, Guéguen, and Schubnel, 2007 cite that elastic properties are dominated by competing forces of porosity loss and crack formation; and Haines et al. 2013 hypothesize that a decrease in V_p and V_s during shear in a clay-rich gouge may be due to fabric formation (Fortin et al., 2005, 2007; Haines et al., 2013). While shear planes and fabrics have been hypothesized as a possible control on elastic properties, no previous work has been done to systematically analyze the relationship between fabrics, fault strength, hydrological properties, and elastic properties.

This study aims to analyze and quantify the effects of shear fabrics within clay rich gouges on the evolution of mechanical and elastic properties throughout shear, including strength, ultrasonic velocity, permeability, and elastic moduli. This work addresses the following fundamental questions:

- 1. As fabrics form and presumably weaken fault gouge, how do they affect its elastic properties?*
- 2. How does clay/smectite abundance affect fabric formation and, therefore, fabric's controls on elastic and mechanical properties?*
- 3. How do shear fabrics affect the permeability of fault gouge?*

Here, I provide insight into the relationships between fabrics, elastic properties, clay abundance, and permeability to illuminate the importance of smectite clay abundance and shear fabric evolution on fault zone properties. We have found that throughgoing shear fabrics, which weaken fault gouge with shear, disrupt the gouge layer and result in decreased stiffness within the layer leading to a reduction in ultrasonic velocities and elastic moduli. In addition, we

observed that weaker gouges – whether due to strain, fabric formation, or increased smectite content – also have lower permeability, up to 2 orders of magnitude for our test conditions.

I do this in the following chapters:

Chapter 2: A Method for Travel Time Calibration and Determination of Absolute Ultrasonic Velocities in a Direct Shear configuration

The double direct shear configuration paired with piezoelectric transducers (PZTs) in the biaxial stress apparatus has been used in a large variety of experiments to study fault gouge strength, porosity evolution, and elastic properties. However, to ensure that shear occurs within the gouge layers and not between the gouge and the forcing blocks, the forcing blocks have grooves oriented perpendicular to the direction of shear (Saffer and Marone, 2003; Anthony and Marone, 2005; Knuth and Marone, 2007). These grooves and the complex geometry of the experiments make it difficult to determine absolute ultrasonic velocities in shear experiments. Absolute velocities allow us to compare our experimental results to in situ measurements. To combat this issue, we have developed a method using gouge layers of various thicknesses to determine how travel time through the steel blocks and grooves changes as a function of shear strain. This allows us to continuously calculate absolute velocities as we can subtract the travel time of our ultrasonic signal through the steel blocks and grooves from the total travel time. We use this calibration method for chapters 3 and 4.

Chapter 3: The Effects of Shear Strain, Fabric, and Porosity Evolution on Elastic and Mechanical Properties of Clay-Rich Fault Gouge

I ran a suite of experiments on 50% smectite / 50% granular quartz synthetic gouge mixtures to determine the effects of fabric and porosity evolution on the mechanical and elastic properties throughout shear. I find that as fabrics form within the clay-rich gouge, porosity and

fabric evolution compete as the two dominant processes controlling P-wave and S-wave velocities as well as bulk and shear moduli. Though porosity decreases throughout shear, fabrics cause a decrease in ultrasonic velocities indicating that porosity and compaction are not the only controls on elastic properties. I define four stages of mechanical and elastic property evolution based on the inferred micromechanical processes controlling the gouge layer behavior.

Chapter 4: Evolution of Fault Gouge Elastic and Mechanical Properties during shear: The Roles of Clay Content, Fabric Development, and Porosity

I ran a suite of double direct shear experiments in the biaxial stress apparatus on a range of synthetic smectite-rich gouges composed of 10 – 100 wt% smectite mixed with granular quartz as well as experiments using Sumatra subduction zone input material obtained on Integrated Ocean Drilling Program (IODP) expedition 362. These experiments analyzed how the abundance of smectite controlled fabric formation and, therefore, the effects of fabrics on elastic properties. We found that elastic properties for synthetic gouges with greater abundances of smectite ($\geq 70\%$) are almost entirely controlled by fabric formation whereas gouges with 50% smectite or less are controlled by a combination of porosity loss, shear enhanced compaction, and fabric formation. The samples from IODP exp 362 have relatively low smectite and higher amounts of illite, a non-swelling clay, and therefore are controlled largely by porosity loss and shear enhanced compaction. We also found that, for these clay-rich gouges, S-wave velocity (V_s) and shear modulus (G) may be more sensitive to fabric formation than P-wave velocity (V_p) and bulk modulus (K).

Chapter 5: Evolution of Permeability During Shear of Fault Gouge: Effects of Composition and Fabric

Though some previous studies have hypothesized or alluded to shear fabrics in smectite-rich gouge being the cause for permeability reduction throughout shear, few have attempted to directly correlate the two (Morrow et al., 1984, 2017; Faulkner and Rutter, 2003; Crawford et al., 2008; Ikari et al., 2009; Behnsen and Faulkner, 2013; Kaproth et al., 2016). Furthermore, none have connected permeability, shear fabrics, friction, and ultrasonic properties. I ran a suite of experiments on synthetic smectite gouge ranging from 10% - 90% Ca-montmorillonite smectite mixed with granular quartz in a true triaxial pressure vessel within a biaxial deformation apparatus. Through these experiments, I was able to determine that while smectite percentage is an extremely important control on permeability, the evolution and maturity of fabrics is possibly equally important in controlling permeability in fault zones.

The overarching goal of this research is to further our understanding of how clay causes such dramatic weakening of fault zones by investigating, in depth, the relationships and links between clay (smectite) abundance, fabric formation and evolution, elastic properties, permeability, and macroscopically measured frictional strength. The implications of this work are that, while it was known that smectite in fault gouge has large effects on the mechanical properties and permeability, it is now clear that shear planes and fabrics formed during shear also have an important effect on elastic properties (V_p , V_s , K , G). This implies that fabrics not only affect frictional properties but also affect sliding stability and stiffness of fault zones. In addition, fabric formation should be considered when interpreting seismic data as indicators of fault zone properties. We also determined that not only is smectite percentage a major driver in permeability reduction, but the exact evolution of shear fabrics is an equal, if not greater control on permeability reduction. This has important implications for elevated pore pressures and fault stability within fault zones as well as reservoir seal potential of smectite-rich faults.

Chapter 2

A Method for Travel Time Calibration and Determination of Absolute Ultrasonic Velocities in Experimental Shear Zones

Abby R. Kenigsberg¹, Jacques Rivière², Chris Marone¹, Demian M. Saffer¹

¹Department of Geosciences and Center for Geomechanics, Geofluids, & Geohazards, The Pennsylvania State University, University Park, Pennsylvania 16802, USA

²Department of Engineering Science and Mechanics, The Pennsylvania State University, University Park, Pennsylvania 16802, USA

2.1 Abstract

Rock mechanics experiments are a vital tool in assessing mechanical, elastic, and chemical properties of Earth materials. These experiments inform geomechanical models and provide data on rock properties and underlying processes; however, apparatus design often limits the ability to report absolute values of elastic wave properties and their evolution during deformation. In particular, accurate measurements of elastic properties and ultrasonic velocity in experimental shear zones are generally difficult to obtain. Here, we describe a method that can be used for any material in a range of machines to calculate absolute P- and S-wave velocities through rigorous calibration experiments. Our method yields absolute velocities and also the possibility of calculating elastic (bulk and shear) moduli and works even for small, thin test samples.

2.2 Introduction

Rock mechanics experiments have been used for decades to measure the mechanical and elastic properties of Earth materials, including rock, soil, sediment, and ice (Logan and Rauenzahn, 1987; Zhang et al., 1990; Scott et al., 1993; Tullis, 1996; Marone, 1998; Goldsby and Kohlstedt, 2001; Scholz, 2002; Saffer and Marone, 2003; Di Toro et al., 2004; Brantut et al., 2008, 2014; Erguler and Ulusay, 2009; Ikari et al., 2009; David et al., 2012; Heap et al., 2015; Savage et al., 2018). In particular, monitoring of ultrasonic wavespeed and its evolution during deformation has proven successful in illuminating the micromechanical processes and role of fabrics and composition in governing elastic properties, rock strength, and fault zone processes (Hadley, 1976; Scott et al., 1993; Jia et al., 1999; Schubnel et al., 2003; Fortin et al., 2005, 2007; Khidas and Jia, 2012; Knuth et al., 2013; Kaproth and Marone, 2014; Rivière et al., 2018; Ryan et al., 2018; Durán et al., 2018; Bolton et al., 2019; Uyanık et al., 2019; Garia et al., 2019; Shreedharan et al., 2019). Elastic properties measured via ultrasonic waves provide sensitive proxies for processes that are difficult to observe directly, including changes in porosity, contact stiffness, and foliation and fabric (Hadley, 1976; Baud et al., 2004; Gettemy et al., 2004; Brenguier et al., 2008; Knuth et al., 2013; Carpenter et al., 2014; Scuderi et al., 2017; Garia et al., 2019). Absolute velocity and elastic property measurements of rock and sediment are also of particular value because they inform upscaling efforts and allow direct comparison with field data and theoretical models.

While relative changes in velocity can be retrieved without knowledge of the absolute wavespeed when changes in time of flight and sample thickness are small (Rivière et al., 2016; Durán et al., 2018), lab experiments often involve large changes in elastic properties as deformation progresses (e.g., Scuderi et al 2016; Tinti et al., 2016), which necessitates information about absolute wavespeed and travel time. One of the challenges – particularly in

small samples or crossing thin layers for which the travel time within the test specimen is on the order of a few μs – is the calibration of travel times to account for apparatus and loading geometry. Indeed, in many experimental configurations the time taken for signals to propagate through forcing blocks, platens, or other elements of the testing system constitute a large fraction of the total travel time, and must be measured and corrected with high accuracy (Fortin et al., 2005, 2007; Knuth et al., 2013; Brantut et al., 2014; Browning et al., 2017).

Here, we describe a method to obtain absolute elastic wave velocities during direct shearing experiments. The method provides instantaneous velocities under load, which can be used to track the evolution of friction, compaction, permeability and other rock properties with progressive deformation. We describe the method using data from friction experiments performed in a double direct shear configuration, on synthetic fault gouge composed of a range of mixtures of Ca-montmorillonite and quartz powder, as well as on marine sediment that represents the protolith for material entrained along the subduction plate boundary offshore Sumatra, obtained by drilling during International Ocean Discovery Program (IODP) Expedition 362 (McNeill, Dugan, Petronotis, & Expedition 362 scientists, 2017). We successfully: 1) calibrate our system to determine the arrival time of ultrasonic waves through the experimental configuration and sample as a function of shear strain, 2) calculate absolute velocities for a range of materials tested, and 3) present an empirical approach for generalizing our method for a variety of loading configurations, apparatuses, and materials.

2.3 Methods

2.3.1 Experimental Configuration and Materials

We conducted double direct shear experiments using a servo-controlled, biaxial deformation system (Figure 2-1). The double direct shear (DDS) configuration allows two layers of fault gouge, sandwiched between three forcing blocks, to be sheared simultaneously under a range of loading conditions (Dieterich, 1972; Mair and Marone, 1999). In our configuration, shear forcing blocks have grooves oriented perpendicular to the shear direction (Figure 2-1) to ensure that shear occurs within the gouge layers and not between the gouge layers and the forcing blocks (Mair and Marone, 1999; Saffer and Marone, 2003; Anthony and Marone, 2005; Knuth and Marone, 2007). In addition, guide plates are secured to the front and back of the sample to contain the sample during shear. The center block is longer than the two side blocks, allowing the surface area (10 cm × 10 cm) to remain constant throughout shear. Gouge layers were prepared using a leveling jig, and single layer thicknesses ranged from 2 mm to 23 mm prior to application of normal stress (Table 2-1).

We used in-house built load cells with a resolution of ± 0.1 kPa (Mair and Marone, 1999) to measure shear and normal stresses. Direct current displacement transducers (DCDTs) with a resolution of ± 0.1 μm were used to measure layer thickness and sliding velocity continuously during shear (Figure 2-2). We report layer thickness from the tops of the ridges between grooves in the DDS forcing blocks (Figure 2-1). We calculate the coefficient of friction by dividing the shear stress by the normal stress (assuming negligible cohesion within the layer) (Figure 2-2). We began experiments by applying a 25 MPa normal stress and then allowing the layers to compact for 20–90 minutes or until the layer thickness stabilized. After initial compaction, we sheared layers to displacements of ~ 40 – 60 mm (shear strains of ~ 20 – 100). All

experiments were conducted at room humidity (11.8-72.6%) and temperature, at a normal stress of 25 MPa, and at a shear velocity of 21.45 $\mu\text{m/s}$. We focus here on data for shear strains $< \sim 20$.

We describe our method using data from sheared layers of synthetic fault gouges composed of varying proportions of smectite and granular quartz, and natural samples of marine sediment collected by drilling off the Sumatra subduction zone (Table 2-1). The Sumatra samples represent protolith for faults in the subduction zone, and are composed of ~ 20 wt% quartz, ~ 12 - 13 wt% plagioclase, and minor ($< 3\%$) calcite; these samples also contain abundant clay minerals, including ~ 15 wt% kaolinite + chlorite, 8-19 wt% smectite, and 32-41 wt% illite (McNeill et al., 2017; Rosenberger et al., 2019 *in prep.*). For comparison with our two-phase synthetic mixtures, we categorize the natural samples based on the combined abundance of smectite + illite. However, it is important to note that illite has different swelling and interlayer properties than smectite, so the Sumatra samples (with $\sim 50\%$ smectite + illite) should behave differently than our synthetic gouges.

2.3.2 Ultrasonic Measurements and Travel Time Calculations

In addition to mechanical data, we measured elastic wavespeed continuously during shear using 1.27 cm-diameter, 500 kHz shear wave piezoelectric (PZT) transducers embedded in the side forcing blocks (Kaproth and Marone, 2014). The PZT in one side forcing block – used as a source – is excited by a 5.3 V half sine-wave shaped pulse, while the PZT in the second side forcing block is used as a receiver (e.g., Knuth et al., 2013). The PZTs generate shear waves, and P-waves are generated via mode conversion. We excite the source PZT every 10 milliseconds throughout the experiment to obtain continuous records of elastic wavespeed. Waves are transmitted and received using a 15-bit data acquisition system. To increase the signal to noise ratio we stacked 25-500 individual waveforms to produce a record every 0.25–5 seconds.

Typically, gouges with higher percentages of quartz have lower signal to noise and require more waveforms to be stacked.

To define travel times, we pick P- and S-wave arrival times in each waveform (Figure 2-3). To do this consistently and accurately, we characterize the signal noise before the P-wave arrival and then again before the S-wave arrival. The arrival times are then picked at the zero-crossing of the mean noise before the signal exceeds two standard deviations (Figure 2-3). To ensure that our picks are accurate, we also compared them to arrivals calculated via cross correlation using a master waveform chosen at zero shear strain. Cross correlation yields a difference in arrival time relative to the master wave, and these are generally within $\pm 0.2 \mu\text{s}$ of our manual picks.

Our travel time measurements document the elastic wave speed through the steel forcing block assembly and gouge layer in aggregate. However, to define absolute travel times and wave velocity for the fault gouge alone, we must independently determine the travel times through the forcing blocks. This presents two challenges: 1) Because the blocks are grooved, we cannot simply place them in contact and apply a load; the grooves acquire microscopic damage during use at high pressure and thus they do not mate perfectly even under load; and 2) The gouge material trapped and entrained within the grooves of the forcing blocks evolves and densifies as the layer is compacted and sheared, yet this material has different properties from the bulk gouge layer itself. As a result, the remnant material in the grooves must be treated as part of the forcing block assembly (i.e. it affects the total travel time but is not part of the gouge layer of interest), with the added complication that – unlike the steel forcing blocks themselves – the velocity and travel time through this material varies as a function of shear strain. To address these issues, we developed an empirical method to determine the travel time through just the forcing blocks and grooves, so that it can be subtracted from the uncalibrated arrival time to define travel time through the shearing gouge layer. Section 2.4 outlines each step of this method.

2.4 Calibration Method for Travel Times and Absolute Velocities

We developed a method to empirically determine the arrival time of ultrasonic signals through the grooved forcing blocks. This travel time, which we term TT_0 , varies as a function of shear strain and is different for each gouge composition due to the evolution of material trapped within the grooves. We create a calibration curve to define the zero travel times (TT_0) as a function of shear strain for each gouge material. This calibration curve allows us to determine travel time through the actively shearing gouge layer from the total (directly measured) travel times, in order to calculate absolute velocities at any given strain. To generate the calibration curve, we conducted shearing experiments on gouge layers of varying thicknesses for each material. Generally, we ran two duplicate experiments for each layer thickness (Table 2-1). The initial layer thickness is controlled by using a carefully measured mass of material and constructing layers using a leveling jig and steel blocks. For some mixtures we report more or fewer experiments, depending on data quality and material availability (Table 2-1).

2.4.1 Travel Time Corrections

After picking the raw arrival times and checking against our cross-correlation method, we define a best-fit line to travel time and gouge thickness, for a series of individual shear strains ($\gamma = 0-20$; increments of ~ 1) (Figure 2-4). The intercept of each linear fit defines the TT_0 , representing the travel time through the blocks and grooves. The slopes of these lines define the slowness of the gouge (s/mm), and provides a secondary set of checks on the absolute velocities derived from our calibration. As noted above, TT_0 varies as functions of both the material and accumulated shear strain. For most fault gouges, the material lodged within the grooves reaches a

steady state by a shear strain of ~ 4 , and as a result the zero times converge at that point. We apply the method separately for P- and S-waves for all materials (Figure 2-5).

We use about 20 individual determinations of zero travel time for each material to construct a calibration curve that defines zero time continuously as a function of shear strain (Figure 2-4B). Note that we carefully track changes in layer thickness for each experiment (e.g., Figure 2-2) and thus calibration curves contain information from experiments that start with different layer thicknesses and also from a given experiment as layers densify and evolve with strain (Figure 2-4A). Our data for travel time and layer thickness are reasonably well fit with rational or exponential functions (Figure 2-4). The root mean square error (RMSE) of this fit provides a measure of error in the zero times that we incorporate in defining formal errors on resulting velocity values (Figure 2-4B). We follow this process for the full range of gouge materials, and for both P- and S-waves (Figure 2-5). Many TT_0 calibration curves have similar characteristics, and start with large arrival times that quickly decrease to nominally constant values by a shear strain of ~ 3 - indicating that the gouge within the grooves has largely stopped evolving or is evolving more slowly. The main deviation from this trend is the P-wave fit for the 49% smectite + illite Sumatra sample, which exhibits an increasing TT_0 with shear strain. We also note that for several of the curves, the value of TT_0 prior to shearing is smaller (i.e. wavespeed is faster) than that immediately after shearing begins. This may be due to a small amount of time-dependent healing that occurs during the initial compaction of the samples, and which allows enhanced grain contacts that are subsequently disrupted by initial shearing. Somewhat unexpectedly, the calibration curves are not systematic with clay percentage, further indicating that a distinct calibration is required for each material.

Using the calibration curves developed in step 2, we then subtract TT_0 from the raw travel times, TT , which are obtained using the same cross correlation method described in section

2.2, to define a corrected travel time, TT_c , which represents the travel time through the two gouge layers only (Figures 2-6 and 2-7):

$$TT_c = TT - TT_0$$

2.4.2 Velocities and Errors

To define absolute velocities, we use a time-of-flight technique with the corrected arrival times (TT_c) and the directly measured gouge layer thickness of the two layers (h):

$$V = \frac{h}{TT_c}$$

The layer thickness is monitored continuously via the horizontal DCDT, and changes throughout shear (Figure 2-2B). We use the RMS error from the calibration curve fits (Figure 2-4), to estimate uncertainty in TT_c , which then defines the uncertainty in velocity. We focus on the RMS error from the calibration curves because other sources of potential error (uncertainty in layer thickness, raw arrival picks, cross correlation picks) are non-systematic and also negligible relative to the RMS error. For the example of 50% smectite shown in Figure 2-8, the uncertainty in velocity ranges from ~ 200 m/s to ~ 400 m/s, corresponding to an error of ~ 8 – 12 %. This is typical for our experiments; error in both V_p and V_s is generally $< \sim 15$ %. The calibration allows us to use absolute values of velocities to make inferences about micromechanical processes within the gouge, and, in tandem with careful monitoring of layer porosity and density, to quantify elastic moduli. For example, we hypothesize that the temporary decrease exhibited in V_p in figure 2-8 is caused by the formation of shear fabrics

which reduce the layer stiffness and mechanical strength. These trends and the interpretation of variations with shearing are discussed in detail in Kenigsberg et al. [2019].

The resulting P- and S- wave velocities for each gouge are shown in Figure 2-9, and exhibit systematic variations as functions of both composition and shear strain. In general, gouges with low percentages of smectite ($\geq 50\%$) exhibit higher V_p and V_s , and velocities increase progressively with shear strain as porosity is further decreased (Kenigsberg et al. [2019]). Gouge samples with higher abundances of smectite ($\leq 70\%$ smectite) exhibit lower V_p and V_s , and velocities decrease with shear strain – which we attribute to the formation of fabrics defined by aligned clay particles and localized shear surfaces that decrease layer stiffness in the direction of wave propagation (normal to shear). These two groups cluster together and the Sumatra samples (containing 8% and 19% smectite) behave similarly to the smectite-poor synthetic gouges.

2.5 Discussion and Conclusions

The calibration method we describe provides a robust way to obtain absolute wave speeds for any material, and can be used in a range of deformation configurations, and is particularly useful for cases where travel time through the apparatus assembly varies as deformation progresses (for example, in the case of large changes in stress, the compression of porous frits used to distribute fluids, etc.). In our case, grooves in the forcing blocks are vital as they force shear to occur within the gouge layer instead of between the gouge layer and the steel blocks; however, they also trap gouge material that then becomes a part of the forcing block assembly for the purpose of calibration. As the gouge within the grooves evolves with shear strain due to comminution and enhanced packing, the arrival time through the forcing block assembly also evolves. Our method

accounts for this and provides a continuous suite of zero travel times (times required for elastic waves to pass through the forcing block assembly).

In a recent study using this method (Kenigsberg et al. [2019]), we not only determined accurate absolute velocities, but also were able to define bulk and shear moduli throughout shearing. We were then able to infer that shear fabrics act in concert with compaction to drive changes in elastic moduli and wavespeeds in the experimental fault zones. In certain phases of shearing, these processes are in competition, wherein progressive compaction drives increasing stiffness, but this is outpaced by reduction in layer-normal stiffness at strains where shear fabrics are actively forming. Taken together with measurements of friction and layer thickness, accurate measurements of wavespeed allow us to tease apart these two key processes. The insights gained into causes of variations in seismic velocity (and impedance) carry important implications for the interpretation of seismic data, as well as for understanding fault stiffness evolution during shearing.

The ability to apply this method to a large range of materials allows us to investigate important micromechanical processes for a large range of geological systems and settings. Velocities paired with friction data gives insight into factors that control elastic and mechanical processes within fault zones. In addition, if experiments allow for porosity calculations, this method also provides a means to define shear and bulk moduli, which provide further insight into material rigidity and stiffness, as well as micromechanical processes, and ultimately feed into interpretation of fault slip mode (e.g., Leeman et al, 2016) and fault physical properties as sensed by active and passive source experiments (Mooney and Ginzburg, 1986; Li et al., 1998, 2004, 2015; Li and Vidale, 2001; Unsworth and Bedrosian, 2004; Audet et al., 2009; Bangs et al., 2009; Tudge and Tobin, 2013).

Acknowledgements: We thank S. Swavely for technical help in the laboratory and Parisa Shokouhi and Charles Ammon for key discussions. We gratefully acknowledge support from the NSF U.S. Science Support Program (Post expedition award), GDL Foundation, DOE geothermal program (DOE EERE DE-EE0006762) and the NSF Geophysics program (NSF-EAR award 1215856 to D.S. and C.M EAR-1520760 and EAR-1547286/1547441). Data available from authors.

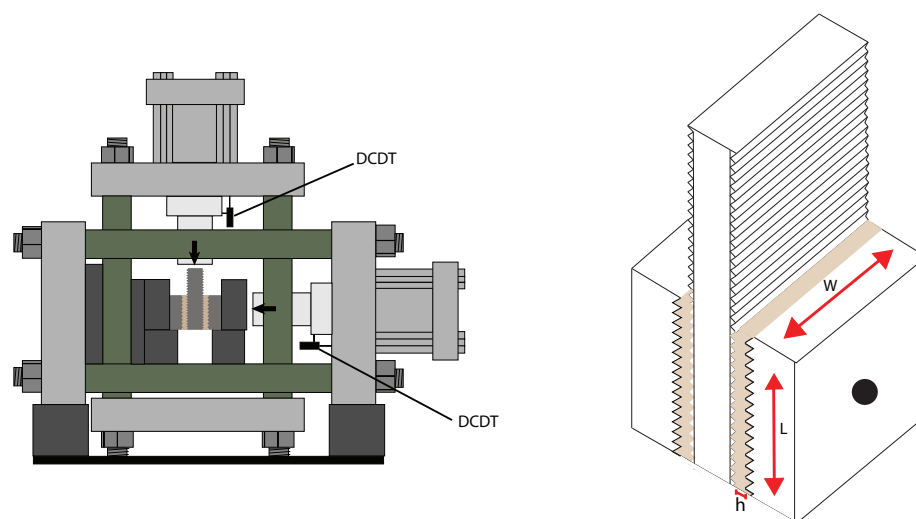


Figure 2-1: Left: Schematic of biaxial stress apparatus and double direct shear (DDS) sample. Right: Schematic of steel blocks and gouge samples with piezoelectric transducers (PZTs) in black.

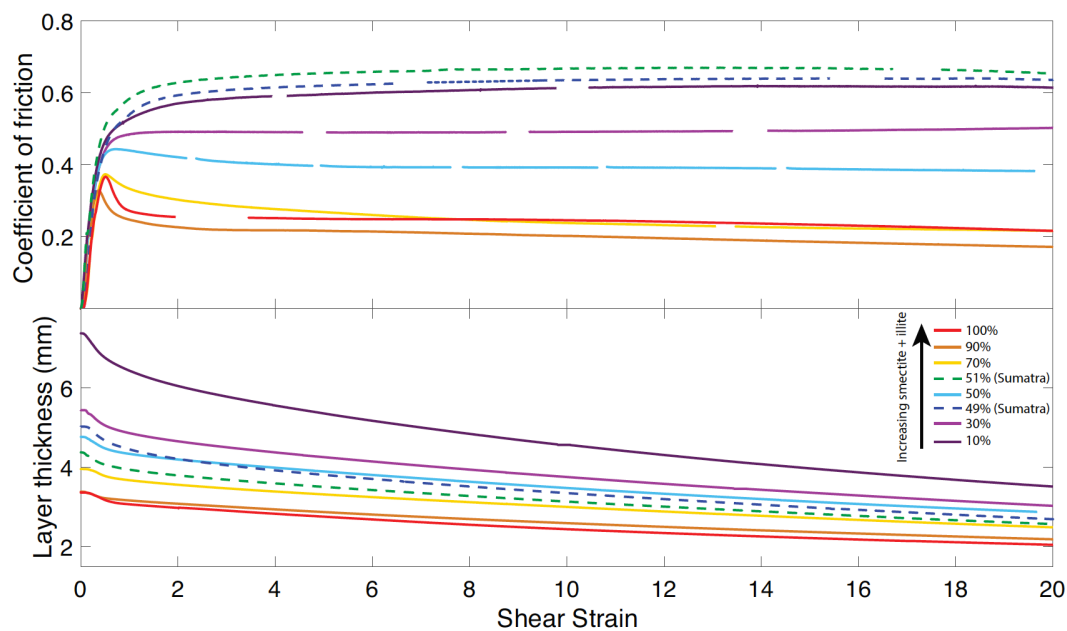


Figure 2-2: Coefficient of friction and layer thickness changes with shear strain. Layer thickness changes are accounted for when calculating velocities and calibrations.

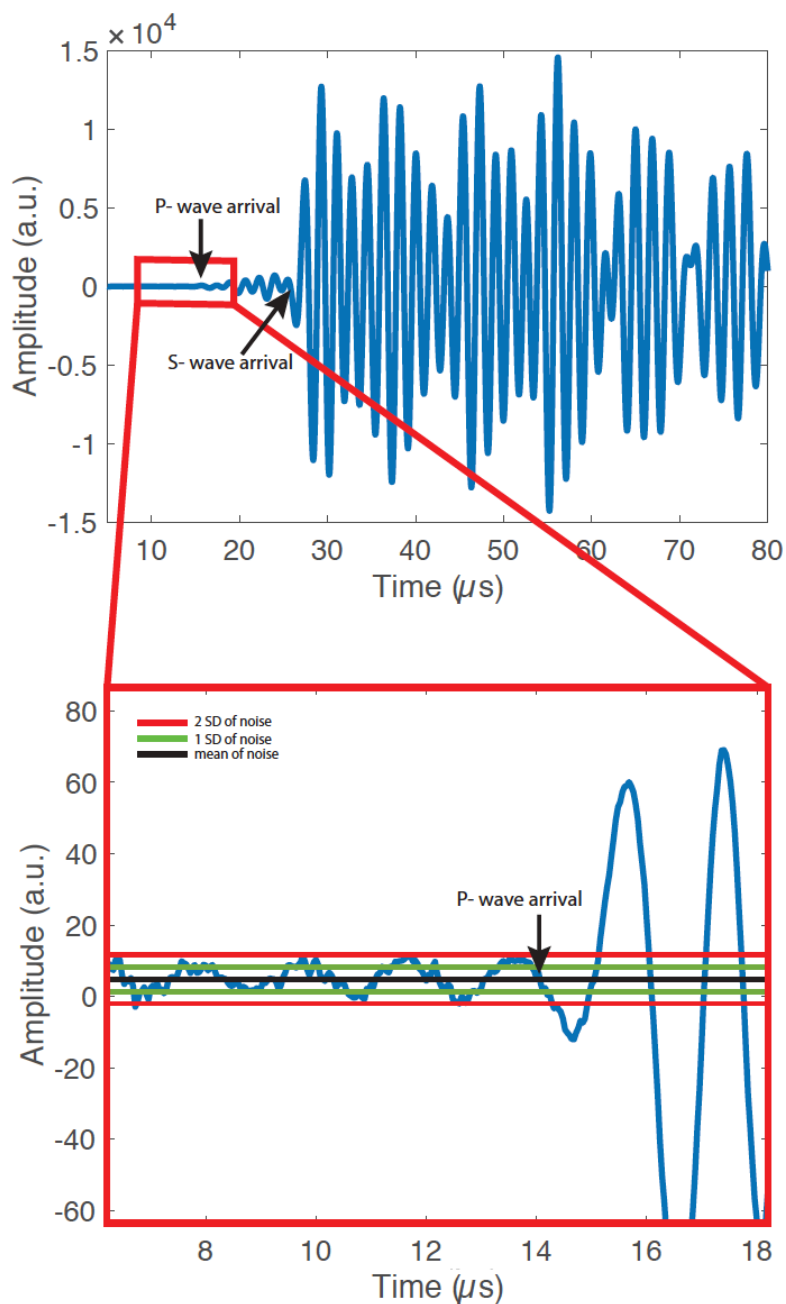


Figure 2-3: Example waveform in a.u., arbitrary units, from p4912 (50% smectite / 50% granular quartz). Mean (black line), ± 1 standard deviation (green line), and ± 2 standard deviation (red line) are calculated based on a portion of the waveform right before the P-wave arrival and then again right before the S-wave arrival. When the waveform crosses the 2 standard deviation red line, the arrival time is picked at the zero crossing of the mean line (black) before the signal crossed the red line.

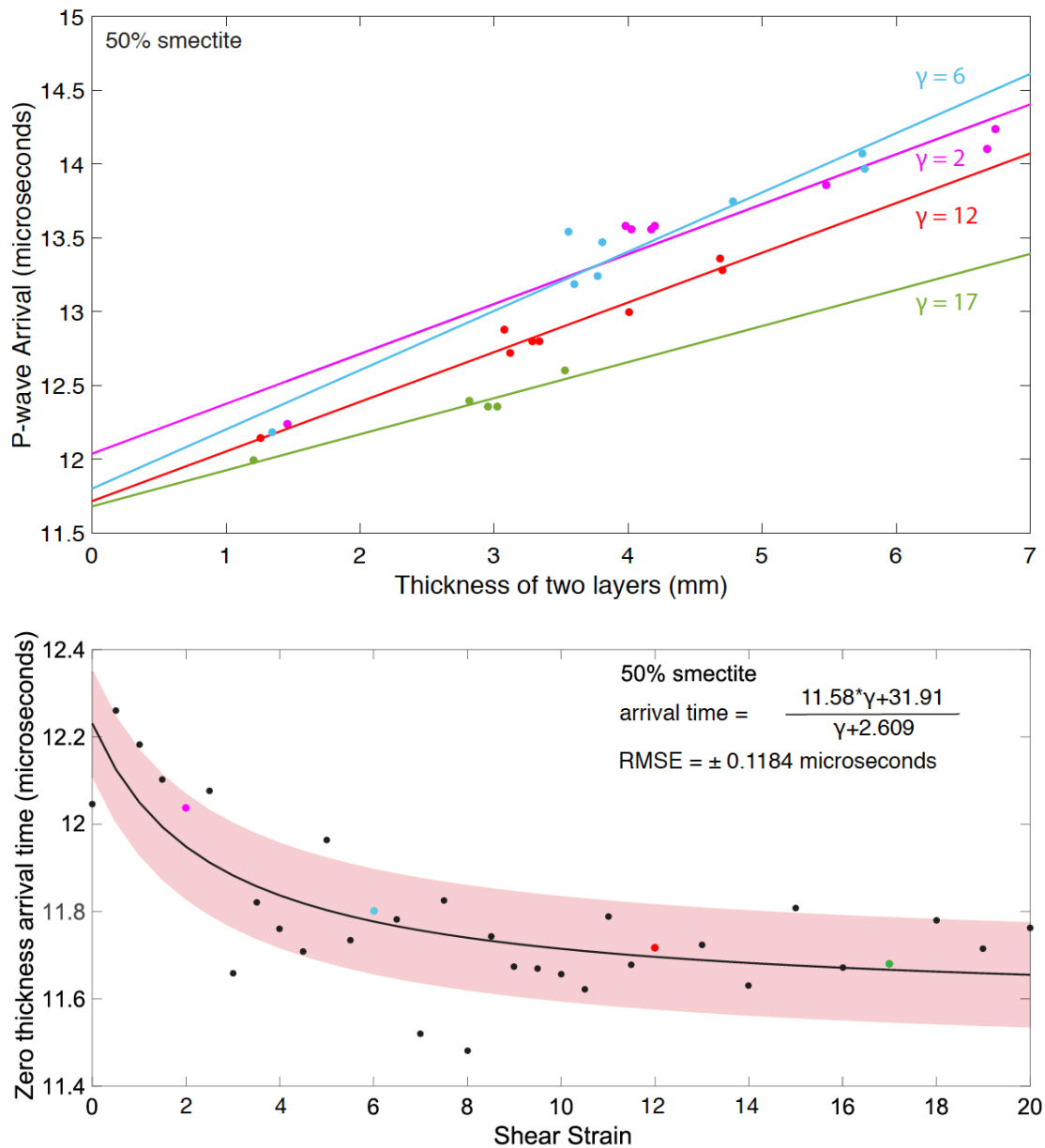


Figure 2-4: Example P-wave arrival times vs layer thickness of two layers for shear strains of 2, 6, 12, and 17. At a shear strain of 2, the arrival time is much slower. However, the lines converge at higher shear strains and all have similar P-wave arrival times. Bottom: 50% smectite 50% quartz example of a calibration curve. The red envelope is \pm RMSE. The pink, blue, red, and green points correspond to the lines in the top portion of this figure for shear strains of 2, 6, 12, and 17.

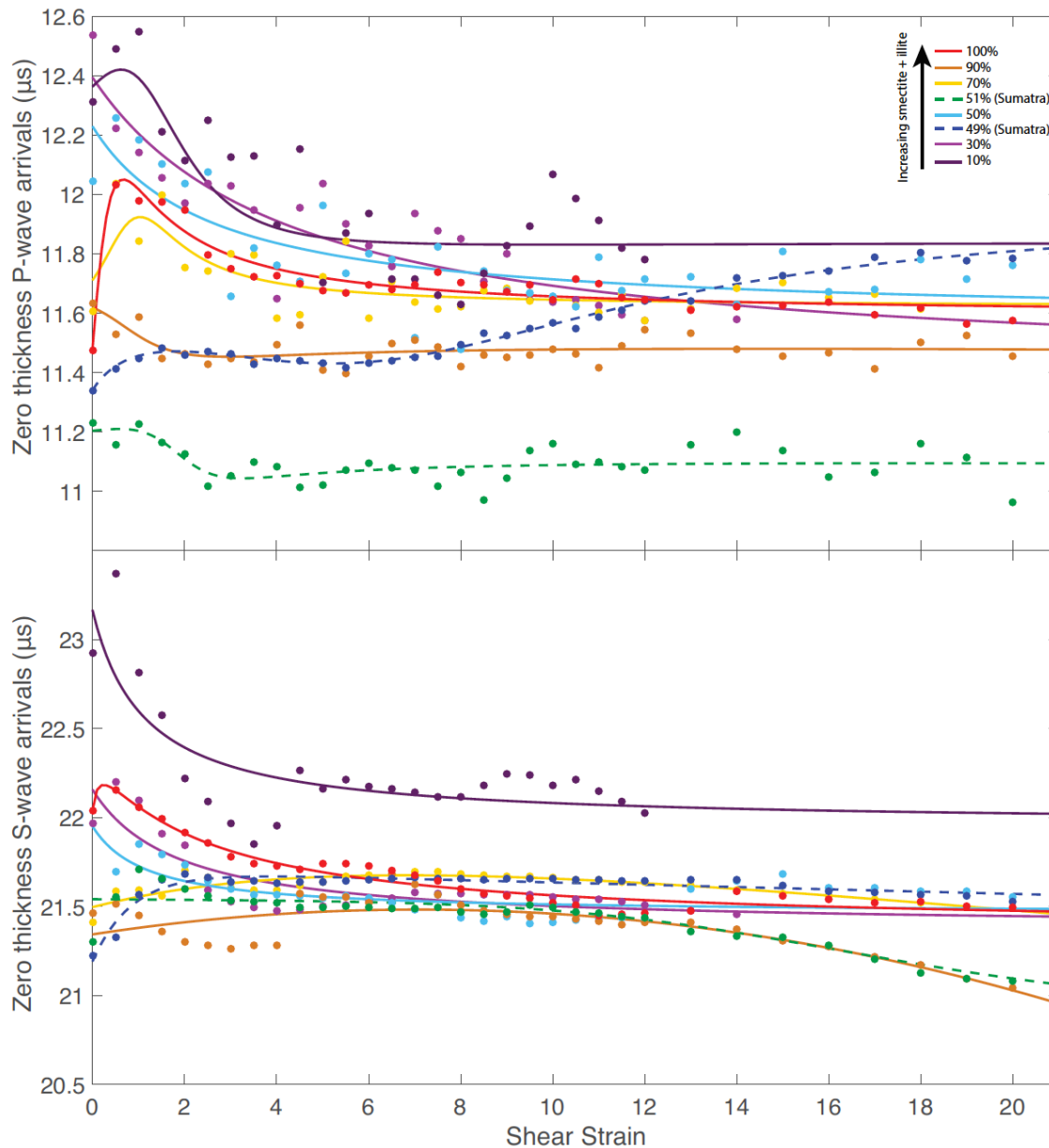


Figure 2-5: P-wave and S-wave calibration curves for 10%, 30%, 50%, 70%, 90%, and 100% smectite synthetic mixtures as well as two natural, Sumatra samples (dotted lines). For the most part, by a shear strain of ~ 4 , the calibration curves reach a steady state. The dots on each line represent zero thickness arrival time at the given shear strain as shown in the top portion of figure 2-4.

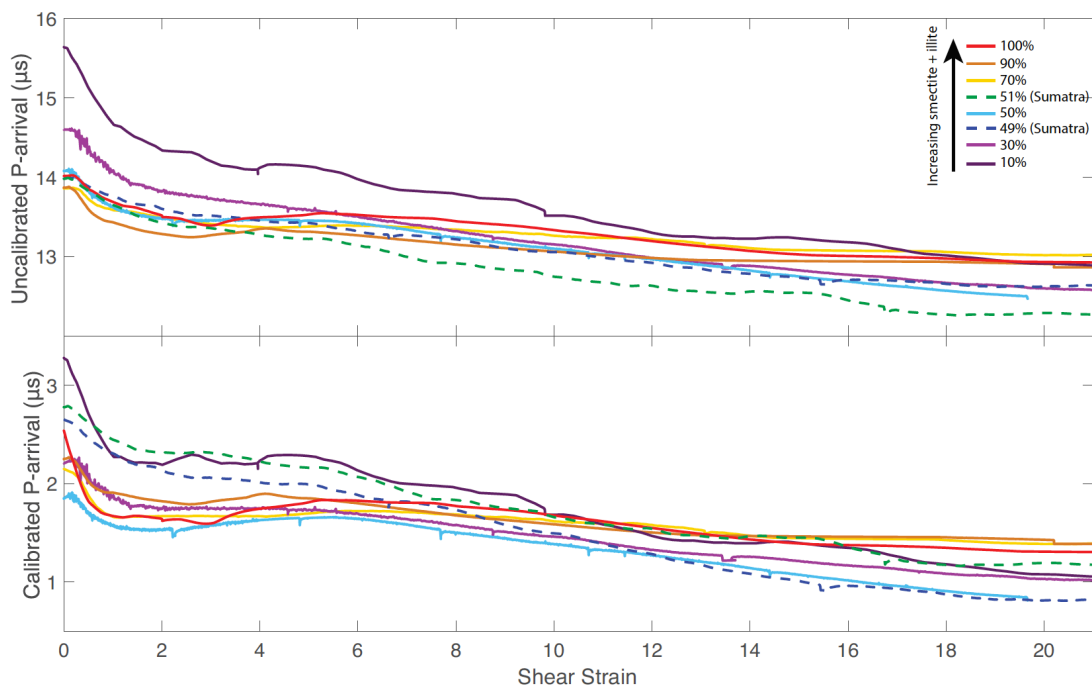


Figure 2-6: Uncalibrated and calibrated P-wave arrival times. The calibrated times are calculated by subtracting the "zero gouge thickness" value obtained from the calibration curve from the uncalibrated arrival time.

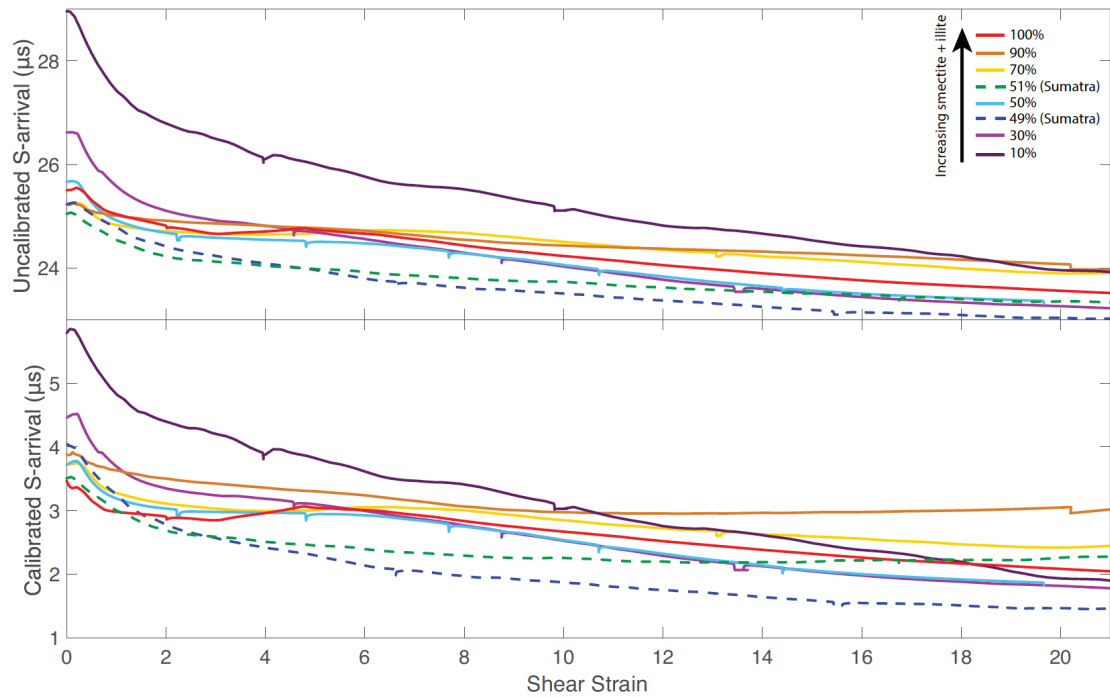


Figure 2-7: Uncalibrated and calibrated S-wave arrival times. The calibrated times are calculated by subtracting the "zero gouge thickness" value obtained from the calibration curve from the uncalibrated arrival time.

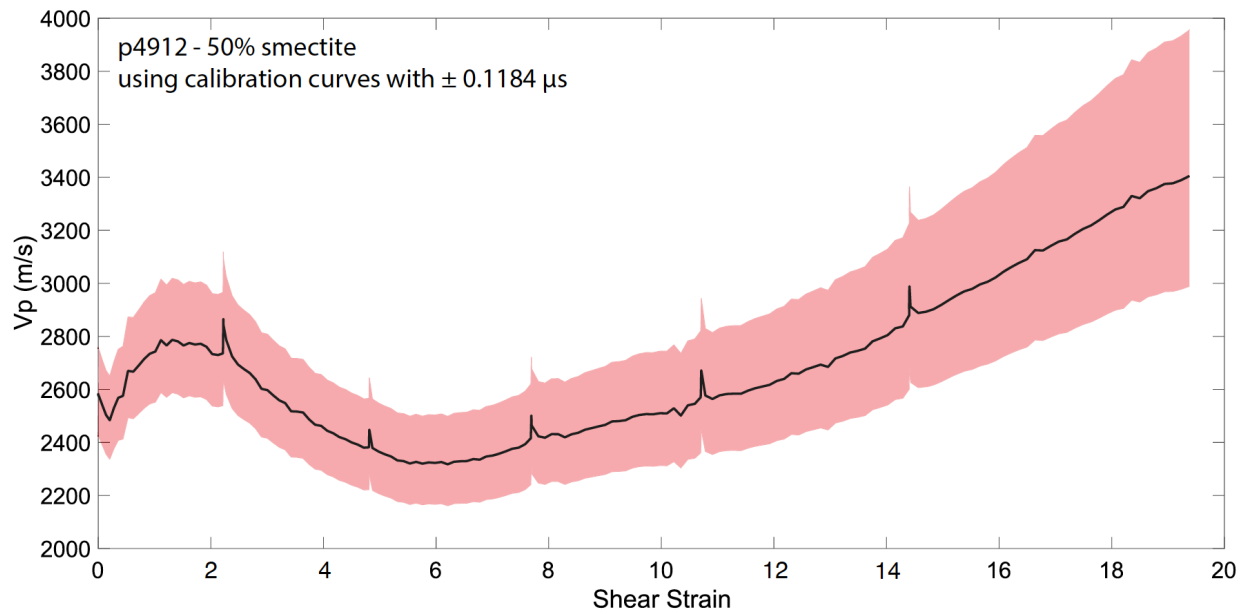


Figure 2-8: Absolute velocity achieved through the calibration process for p4912, 50% smectite. The red envelope represents the error imposed by the RMSE from figure 2-4.

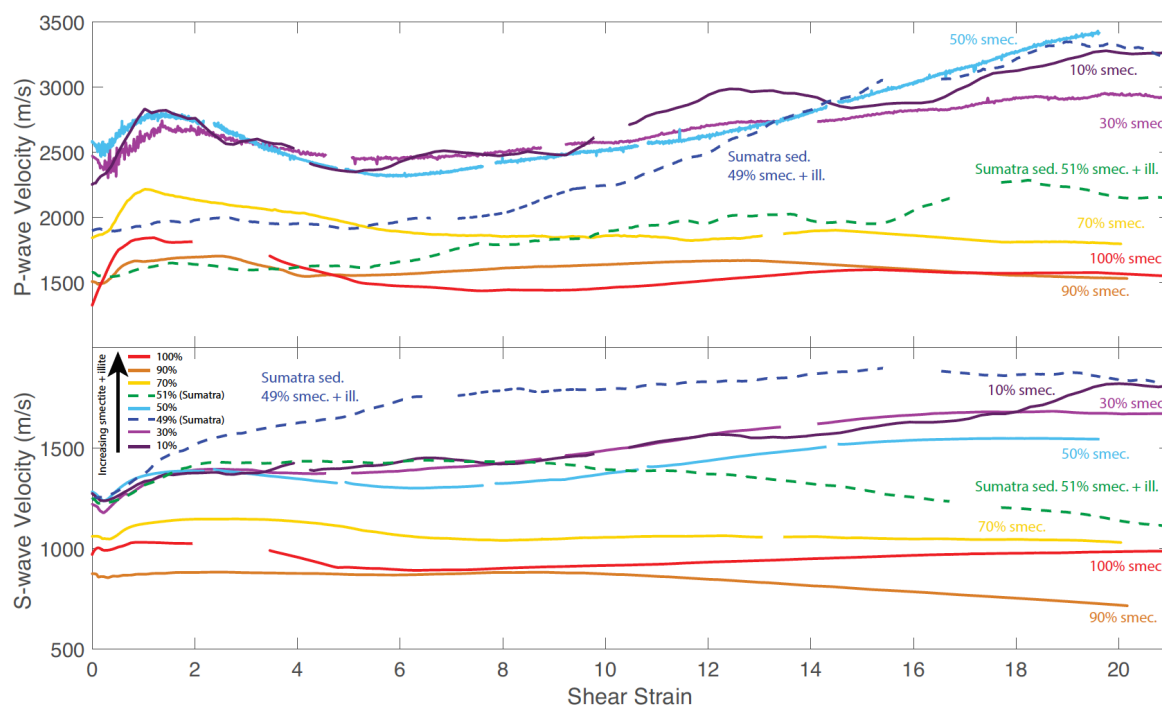


Figure 2-9: P- and S- wave absolute velocities for all synthetic smectite gouge mixtures as well as the Sumatra samples.

Table 2-1: List of Experiments

Experiment #	Composition	Single layer thickness before compaction (mm)
p5212	100% smectite	8 mm
p5213	100% smectite	8 mm
p5214	100% smectite	3 mm
p5215	100% smectite	3 mm
p5216	100% smectite	5 mm
p5217	100% smectite	5 mm
p5145	90% smectite/ 10% quartz	3 mm
p5148	90% smectite/ 10% quartz	8 mm
p5149	90% smectite/ 10% quartz	5 mm
p5150	90% smectite/ 10% quartz	8 mm
p5154	90% smectite/ 10% quartz	3 mm
p5157	90% smectite/ 10% quartz	5 mm
p5039	70% smectite/ 30% quartz	3 mm
p5040	70% smectite/ 30% quartz	3 mm
p5043	70% smectite/ 30% quartz	8 mm
p5052	70% smectite/ 30% quartz	5 mm
p5128	70% smectite/ 30% quartz	8 mm
p5136	70% smectite/ 30% quartz	5 mm
p4808	50% smectite/ 50% quartz	5 mm
p4830	50% smectite/ 50% quartz	5 mm
p4853	50% smectite/ 50% quartz	23 mm

p4867	50% smectite/ 50% quartz	3 mm
p4912	50% smectite/ 50% quartz	5 mm
p4913	50% smectite/ 50% quartz	5 mm
p4947	50% smectite/ 50% quartz	8 mm
p4962	50% smectite/ 50% quartz	8 mm
p4977	50% smectite/ 50% quartz	7 mm
p5129	30% smectite/ 70% quartz	8 mm
p5137	30% smectite/ 70% quartz	5 mm
p5141	30% smectite/ 70% quartz	8 mm
p5142	30% smectite/ 70% quartz	3 mm
p5143	30% smectite/ 70% quartz	3 mm
p5144	30% smectite/ 70% quartz	5 mm
p5167	10% smectite/ 90% quartz	8 mm
p5176	10% smectite/ 90% quartz	5 mm
p5178	10% smectite/ 90% quartz	5 mm
p5184	10% smectite/ 90% quartz	8 mm
p5185	10% smectite/ 90% quartz	3 mm
p5189	10% smectite/ 90% quartz	3 mm
p5218	U1480F-74X-2, 79-93cm	5 mm
p5219	U1480F-74X-2, 79-93cm	3 mm
p5223	U1480F-74X-2, 79-93cm	8 mm
p5224	U1480F-74X-2, 79-93cm	3 mm
p5225	U1480F-74X-2, 79-93cm	5 mm
p5226	U1480F-74X-2, 79-93cm	8 mm

p5196	U1480E-9H-1, 130-150cm	5 mm
p5197	U1480E-9H-1, 130-150cm	3 mm
p5199	U1480E-9H-1, 130-150cm	8 mm
p5203	U1480E-9H-1, 130-150cm	3 mm
p5204	U1480E-9H-1, 130-150cm	5 mm

Chapter 3

The Effects of Shear Strain, Fabric, and Porosity Evolution on Elastic and Mechanical Properties of Clay-Rich Fault Gouge

Abby R. Kenigsberg¹, Jacques Rivière², Chris Marone¹, Demian M. Saffer¹

¹Department of Geosciences and Center for Geomechanics, Geofluids, & Geohazards, The Pennsylvania State University, University Park, Pennsylvania 16802, USA

²Department of Engineering Science and Mechanics, The Pennsylvania State University, University Park, Pennsylvania 16802, USA

3.1 Abstract

The elastic and mechanical properties of fault gouge are key controls on fault zone stiffness, strength, damage, healing, and sliding stability. Clay minerals are prevalent in fault zones and have significant effects on friction, porosity, elastic properties, and shear fabric development. Though clay-rich gouges are well studied, the roles of porosity evolution and fabric formation in modulating elastic and mechanical properties are unclear. For example, in this study, we have found that with progressive shear, the role of strain localization and fabric development may compete with densification to control the evolution of friction and elastic moduli. We report on a suite of double-direct shear experiments on synthetic gouge composed of 50% Ca-montmorillonite and 50% granular quartz at a normal stress of 25 MPa. We measure the coefficient of friction, porosity, P- and S- wave speeds, and bulk and shear moduli, and their evolution with shearing, to shear strains up to ~ 25 . We find that the evolution of V_p , V_s , and elastic moduli are controlled by the interplay of porosity loss, shear fabric development, and particle contact stiffness. In general, V_p , V_s , and elastic moduli increase with shear strain and are

accompanied by gradual densification and porosity loss. However, at intermediate shear strains (~2-8) a decrease in V_p , V_s , and elastic moduli is superimposed on this overall trend. Based on previous studies, we hypothesize that shear bands develop parallel to shear direction (perpendicular to wave propagation) over this range of strains, suggesting that fabric development leads to reduced fault stiffness and competes with porosity loss as the dominant control of elastic properties.

3.2 Introduction

Clay minerals are common in shallow tectonic fault zones, and play a key role in governing their frictional strength and sliding behavior (Wu et al., 1975; Wu, 1978; Wang et al., 1980; Morrow et al., 1984, 2017; Vrolijk and van der Pluijm, 1999; Kopf and Brown, 2003; Moore and Lockner, 2004; Ikari et al., 2007, 2009; Niemeijer et al., 2010; Tembe et al., 2010; Carpenter et al., 2011, 2012; Behnsen and Faulkner, 2013). The effects of clays, and smectite family minerals in particular, on frictional behavior have been linked directly to the abundance of these weaker phases in fault rock (Logan and Rauenzahn, 1987; Kopf and Brown, 2003; Saffer and Marone, 2003). Experimental studies have shown that clay-bearing faults remain frictionally weak over a range of normal stresses (5 – 100 MPa), humidity and water content (dry to fully saturated), and clay types (smectite, illite, talc) (Wu et al., 1975; Wu, 1978; Saffer et al., 2001; Saffer and Marone, 2003; Niemeijer et al., 2010; Tembe et al., 2010; Carpenter et al., 2012).

Laboratory and field studies have also highlighted the roles of clay mineral alignment and shear plane development in controlling both fault strength and frictional properties (Schleicher et al., 2006; Collettini et al., 2009; Haines et al., 2009, 2013; Niemeijer et al., 2010). For example, previous work has shown that weakening occurs when clay minerals align along shear planes,

even if these fabric elements are interspersed with or anastomose around other compositional elements in fault gouge (Logan et al., 1979; Logan and Rauenzahn, 1987; Collettini et al., 2009; Niemeijer et al., 2010; Tembe et al., 2010; Haines et al., 2013; Wojatschke et al., 2016). Clay-rich gouges often exhibit a peak and subsequent decay of frictional strength with increasing shear strain, interpreted to reflect the development of shear fabric (Logan and Rauenzahn, 1987; Saffer and Marone, 2003; Ikari et al., 2009; Knuth et al., 2013; Haines et al., 2013). Several studies have also investigated the role of clay abundance in controlling the velocity dependence of friction (Kopf and Brown, 2003; Saffer and Marone, 2003; Collettini et al., 2009; Haines et al., 2009; Niemeijer et al., 2010; Ikari et al., 2011; Carpenter et al., 2012; den Hartog et al., 2012; Morrow et al., 2017; Scuderi et al., 2017), and have shown that gouges with high abundances of clay minerals generally do not exhibit the velocity weakening behavior that is necessary to initiate unstable sliding. However, under certain conditions, phyllosilicate rich gouge may exhibit both an increase in frictional strength and increasing tendency toward unstable slip, as a function of increased cementation, consolidation, or shear localization and fabric development (Moore et al., 1989; Moore and Saffer, 2001; Saffer and Marone, 2003; Ikari et al., 2011).

Although less studied, fabric formation also affects the elastic properties of fault zone rocks and gouges. Changes in elastic properties can be used as a tool to probe fault processes and characteristics that are otherwise difficult to observe, including changes in elastic moduli during stick-slip or seismic cycles (Brennguier et al., 2008; Scuderi et al., 2017), the evolution of fabrics and porosity loss with shear and as a function of fault architecture (Gettemy et al., 2004; Knuth et al., 2013; Carpenter et al., 2014), and monitoring of fault stiffness that plays a role in controlling sliding stability (Scholz, 2002; Leeman et al., 2016). These processes range from fault healing and crack opening and sealing to basic characteristics of fault material such as grain coordination and grain stiffness as well as changes in porosity (Hadley, 1976; Digby, 1981; Schubnel et al., 2003; Fortin et al., 2005, 2007; Mavko et al., 2009; Faulkner et al., 2010; Khidas

and Jia, 2012; Knuth et al., 2013; Kaproth and Marone, 2014). While a few studies have explored the evolution of wavespeed and elastic properties during shearing, a gap remains in connecting elastic properties to many important frictional properties such as compaction and shear fabric (Hadley, 1976; Nur et al., 1998; Popp and Kern, 1998; Jia et al., 1999; Schubnel et al., 2003; Fortin et al., 2005, 2007; Khidas and Jia, 2012; Knuth et al., 2013; Kaproth and Marone, 2014). For example, low velocity zones (LVFs) within fault zones are thought to be due factors such as low stress, fault zone damage, or porosity (Mooney and Ginzburg, 1986; Li et al., 1998, 2004, 2015; Li and Vidale, 2001; Unsworth and Bedrosian, 2004; Audet et al., 2009; Bangs et al., 2009; Tudge and Tobin, 2013), however, if recent studies hypothesizing that fabric may decrease velocities are correct (Knuth et al., 2013; Haines et al., 2013; Kaproth and Marone, 2014), then fabrics should also be considered a possible cause of LVFs.

Here, we investigate the co-evolution of mechanical and elastic properties of clay-rich gouge with shear strain, focusing on the effects of fabric development and porosity loss. We report on carefully controlled laboratory friction experiments using synthetic gouge composed of 50% Ca-montmorillonite smectite and 50% granular quartz. Specifically, we: 1) relate the evolution of frictional strength and shear strain to the development and nature of fabric and localization; 2) develop links between elastic properties of gouge (V_p , V_s , elastic moduli) and shear strain; and 3) discuss the co-evolution of friction and elastic properties during compaction (porosity loss) and shear (fabric formation) to develop insights into the micromechanics that control friction and elastic properties.

3.3 Materials and Methods

3.3.1 Experimental Configuration for Shearing and Friction Measurements

We conducted shearing experiments on synthetic clay-rich fault gouge in a servo-controlled, biaxial deformation apparatus using a double-direct shear (DDS) configuration (Figure 3-1)(Anthony & Marone, 2005; Knuth & Marone, 2007). We sheared gouge layers of 50 wt% Ca-montmorillonite and 50 wt% granular quartz under conditions of constant normal stress and controlled shear velocity to shear strains of ~ 25 . Knuth et al. 2013 conducted grain size analyses and determined 95% of the granular quartz is between 53 – 212 μm and the mean grain size is 127 μm . The Ca-montmorillonite is polydisperse and individual grains form clumps from 10 – 200 μm and peaks at ~ 75 μm (Knuth et al., 2013). Experiments were conducted under room humidity conditions (~ 26 – 86% RH) (Table 3-1). The DDS configuration involves two fault zones that are sheared simultaneously under identical stress conditions, between three forcing blocks with grooves oriented perpendicular to the slip direction to ensure that shear occurs within the fault zone (Figure 3-1) (Mair and Marone, 1999). We constructed layers to a thickness of 5 mm using a leveling jig and affixed guide plates to constrain the layer at the front and back (Figure 3-1). The center block is longer than the side forcing blocks, such that the nominal frictional contact area (10 cm X 10 cm) remains constant during shear.

We conducted all of our experiments at a normal stress of 25 MPa and controlled shear velocities of 21.5 $\mu\text{m/s}$, which are similar conditions to previous studies and within the range of shallow fault conditions. We measured shear and normal stresses throughout each experiment using load cells with a resolution of ± 0.1 kPa (Kaproth and Marone, 2014), and monitored sliding velocity and layer thickness continuously via direct current displacement transducers (DCDT) with an accuracy of ± 0.1 μm . We plot the ratio of shear stress divided by normal stress

and refer to it as the coefficient of friction (μ), under the assumption that cohesion in the granular layer is negligible (Figure 3-4, Table 3-1). Experiments began by applying normal stress and waiting until the layers compacted to a steady state thickness, typically after ~60 minutes. The initial layer thicknesses under load were 2-2.5 mm (Table 3-1).

3.3.2 Computation of mass loss and porosity

One key objective in our experiments was to carefully monitor gouge porosity and density and their variation during shear. In the DDS geometry, layers thin as a function of shear strain, due to the combined effects of gouge extrusion and densification due to compaction (Scott et al., 1994). The former process is referred to as geometric thinning because in the simple case where shear strain is constant across the layer, the layer thins as a function of shear by a factor $dx/2dh$ as gouge is transported out of the actively shearing volume with the leading edge of the center block, where x is shear offset at the layer boundary and h is layer thickness (Scott et al., 1994; Ikari et al., 2011; Kaproth and Marone, 2014). We measure changes in layer thickness throughout our experiments directly, but in order to determine gouge porosity (and density) throughout shear, the mass loss due to extrusion must be taken into account (Kaproth and Marone, 2014).

We estimate this loss assuming extrusion of a rectangular plug from the bottom of the layer during shearing, following Kaproth and Marone (2014). Using initial values of layer mass (known from sample construction) and thickness (measured under load with a digital caliper to an accuracy of $\pm 50 \mu\text{m}$), we obtain a continuous record of density and porosity during shear on the basis of conservation of mass. Initial porosity and bulk density are given by:

$$\rho_i = \frac{M_i}{(2hA) + V_T}$$

and

$$\phi_i = \left(1 - \frac{\rho_i}{\rho_s}\right) \times 100$$

where ρ_i is the initial layer bulk density, M_i is the initial mass, h is single layer thickness, A is the nominal frictional contact area, V_T is the total volume of the grooves in the forcing blocks, ϕ_i is the initial porosity (in percent), ρ_i is the initial layer bulk density, and ρ_s is the average solid grain density of the two-phase mixture (assumed to be 2.65 g/cm³).

During shear, the mass in the layer is given by:

$$M_{(n+1)} = M - M_L$$

or

$$M_{(n+1)} = (\rho_n V_n) - (\rho_n V_L)$$

where M is the initial mass, M_L is mass lost by extrusion, V_L is volume lost throughout shear, and V is the gouge volume that remains in the DDS configuration; V_L and V are in turn given by:

$$V_L = (2hWdy) + (2gv_T dy)$$

and

$$V = (2hA) + V_T$$

where W is the width of the blocks, dy is the distance sheared, g is the number of grooves/cm, and v_T is the volume of a single tooth in the center block. Density and porosity at any given shear displacement are then defined from the volume and mass remaining in the layer:

$$\rho = \frac{M}{(2hA) + V_T}$$

$$\phi = \left(1 - \frac{\rho}{\rho_s}\right) \times 100$$

We conducted an extensive set of tests and calibrations to verify the assumption of rectangular extrusion. A key part of these tests involved manually collecting the mass extruded from each layer at regular intervals during shear for comparison with predicted layer mass and mass loss. We conducted four calibration runs and measured mass loss 6-7 times in each run (Table 3-1) and for this suite of tests the maximum difference between the measured mass loss and that predicted by Equation (4) was 4g, or ~3.5 - 4% of the total layer mass.

3.3.3 Ultrasonic velocity measurements

We measured elastic wave speed throughout shear using shear wave piezoelectric (PZT) transducers embedded in the side blocks of the DDS assembly (Figure 3-2). The PZT ceramics are 1.27 cm in diameter and have a center frequency of 500 kHz. The PZTs are bonded in a blind hole 7 mm behind the grooved face of the DDS forcing blocks (Figure 3-1). One PZT acts as a transmitter and one as a receiver (Figure 3-1). P-waves are generated in this configuration via mode conversion. We use a 15-bit data acquisition system, which sends a short pulse (one cycle at 0.5 MHz) every 10 milliseconds throughout the experiment. We recorded individual waveforms, and stacked these in groups of 50 during processing to increase signal-to-noise ratio.

We calculate wave speeds using a time of flight technique from first arrivals and measured layer thickness, incorporating an extensive set of calibrations to define wave travel time through the forcing block assembly (see Chapter 2). We use waveform cross correlation to monitor the evolution of P- and S-wave arrival times. For each waveform, the cross correlation provides a time shift relative to a master waveform, which we choose early in an experiment (prior to shear). We pick the first arrival time for the master waveform using a threshold based on signal noise (Figure 3-2) and then add the time shifts to the rest of the waveforms to determine the absolute arrival times throughout the experiment.

After arrival times are determined, we determine shear and compressional wave velocities of the gouge layers. Calculating absolute velocities for the gouge layers in the double direct shear apparatus presents a unique challenge. We could simply calibrate the system by conducting an experiment without any gouge layers (i.e., by placing the three steel blocks in direct contact) to estimate the time of flight within the steel blocks. However, we cannot press the steel blocks against each other without damaging the grooves. To address this issue, we conducted an extensive set of calibrations to measure the travel time through the steel blocks and the gouge material within the grooves in each DDS forcing block (Figure 3-3). The resulting calibration yields travel times within the forcing block assembly and grooves as a function of shear strain for both P- and S- waves (TT_P and TT_S), which must be subtracted from the total travel time to define the travel time for the gouge layer itself (TT_g). This calibration is described in detail in chapter 2.

Velocities are then calculated by:

$$V = \frac{2h}{TT_g}$$

where V is velocity and h is the measured thickness of a single gouge layer. The primary source of error for our velocity calculations is from manual P- and S-wave arrival picks that are used in the calibration of the blocks. Propagating this error into our velocity measurements gives us a maximum error of $\pm 15\%$ in our V_p calculations (Chapter 2). We compute bulk (K) and shear (G) moduli from the P- and S- wave velocities and layer bulk density (Digby, 1981; Mavko et al., 2009):

$$K = \rho V_p^2 - \frac{4}{3}G$$

$$G = \rho V_s^2$$

3.3.4 SEM Imaging and High-Resolution X-ray CT Scans

SEM images were taken using a FEI Nova NanoSEM 630 FESEM at 10 kV. All samples were gold coated using a Leica EM ACE600 high vacuum sputter coater. We built new layers in experiments p4915 and p4913, and collected the resulting sheared gouge wafers after shear. We then allowed the wafer to break within the middle of the sample so that we could image the wafer while avoiding edge effects. We did not cut the wafer with a razor blade as it would have smeared the smectite. Though we attempted several methods to epoxy the wafers, the smectite was too impermeable and, therefore, we imaged rough surfaces perpendicular to the direction of shear. Though imaging rough surfaces is not ideal, we were able to obtain evidence for Riedel shears and Y-shears. We also compared our SEM images to Haines et al., 2013 to provide further evidence for our hypotheses.

CT scans were done at the University of Texas High-Resolution X-ray CT Facility using a Fein Focus High Power source at 160 kV, 0.105 mA, and an aluminum foil filter.

3.4 Results

3.4.1 Evolution of friction, porosity, and layer thickness

We calculated friction and porosity, and measured layer thickness throughout our experiments. We observe that shear stress and friction evolve systematically as a function of shear strain, up to the maximum strains of ~ 25 attained in our experiments (Figure 3-4). Shear stress increases rapidly with initial loading along an elastic loading curve, followed by the onset of inelastic strain and bulk frictional shear prior to reaching a peak strength with a friction coefficient of $\sim 0.43 - 0.47$ at a shear strain of ~ 0.5 (Figure 3-4). Following peak stress, friction decreases to a residual steady state value of $\mu = \sim 0.4$, with some variation between experiments ($0.43 - 0.49$), similar to the behavior reported in previous work on clay-rich gouges (Logan and Rauenzahn, 1987; Saffer and Marone, 2003; Ikari et al., 2009; Knuth et al., 2013; Haines et al., 2013). Layer thickness and porosity decrease rapidly before peak friction is reached, after which both porosity and layer thickness decrease more slowly, and the layer thickness approaches the linear reduction expected due to geometric thinning. During initial compaction at zero shear strain, each layer thins from 5 mm to ~ 2.4 mm; with shear they thin to < 1.5 mm (Figure 3-4). Initial porosity values after compaction from normal stress application range from 28-33% and decrease to 21-25% by shear strains of 20-25. As the coefficient of friction evolves most rapidly leading up to steady state friction (shear strains from 0 to ~ 2), porosity and layer thickness also

decrease most rapidly, before reaching a more linear decay (Figure 3-4). The initiation of this latter phase corresponds to the onset of steady state friction.

3.4.2 Ultrasonic velocities

In general, V_p , V_s , and V_p/V_s all increase as a function of shear strain (Figure 3-5). At intermediate shear strains ($\sim 2-8$) a decrease in velocities causes a deviation from this overall trend. We identify four main stages of behavior based on the combined frictional and ultrasonic behavior (Figure 3-5). Stage 1 (Figure 3-5, red portion of stress-strain curve) encompasses the initial load up (beginning at $V_p \sim 2350 - 2580$ m/s) and ends as the peak coefficient of friction is reached ($V_p \sim 2690$ m/s). Stage 2 (Figure 3-5, black) starts at peak friction and continues until V_p reaches a peak at a shear strains of 1.4-2.3, depending on the individual experiment ($V_p \sim 2800 - 3240$ m/s). Stage 3 (Figure 3-5, green) is characterized by a reduction in V_p from its peak value to a minimum at shear strains ranging from 6.1 – 8.5 ($V_p \sim 2310 - 2720$ m/s); this is the only portion of the experiments in which wavespeed decreases (Figure 3-5). Stage 4 (Figure 3-5, gray) continues until the end of each experiment, to shear strains of 19.6 – 23.1 ($V_p \sim 3420 - 4545$ m/s). During Stage 4, friction is relatively constant and P-wave velocity increases.

At the start of shear (early in Stage 1) we observe initial decreases in V_p , V_s , and V_p/V_s ratio. This is likely due to a disruption of grain contacts that formed prior to shearing, as the layer compacted. Following this very short-lived decrease, V_p , V_s , and V_p/V_s all increase as peak frictional strength is reached (to the end of stage 1, $V_p \sim 2600$ m/s, $V_s \sim 1210 - 1328$ m/s, $V_p/V_s \sim 2.02 - 2.22$), and velocities and V_p/V_s continue to increase as friction decreases past the peak strength (through stage 2) up to values of $V_p \sim 2800 - 3240$ m/s, $V_s \sim 1320 - 1390$ m/s, and $V_p/V_s \sim 2.02 - 2.34$ (Figure 3-5). V_p , V_s , and V_p/V_s then decrease to $\sim 2312 - 2720$ m/s, $\sim 1240 - 1340$ m/s, and 1.78 – 2.03 respectively, as residual friction is approached at shear strains

of ~6.1-8.5 (stage 3). At higher strains, V_p , V_s , and V_p/V_s all increase progressively with further shear, to maximum shear strains of ~19-23 (stage 4).

Ultrasonic velocities (V_p , V_s , and V_p/V_s ratio) all exhibit trends with shear strain that reflect the same trends observed in the evolution of friction. The ratio of V_p/V_s varies slightly among our experiments during Stages 1 and 2. Experiments p4912 and p4830 exhibit an increase in V_p/V_s during Stage 1, similar to V_p and V_s , while p4913 shows a slight decrease. During Stage 2, V_p/V_s in experiments p4912 and p4913 stabilizes while in experiment p4830 it increases. However, the trends observed for V_p/V_s in stages 3 and 4 are similar to the trends in V_p and V_s .

3.4.3 SEM and CT scan shear fabric observations

To investigate the development of fabric that accompanies evolving mechanical and elastic properties, imaged wafers from two experiments: p4915 which is sheared until right after peak friction and at the onset of stage 2 (shear strain ~0.5) and p4913 which is sheared until steady state friction is achieved during stage 4 (shear strain ~21) (figure 3-6). We also obtained High-Resolution X-ray CT Scans of these two wafers to monitor grain scale evolution.

In p4915, immediately after peak friction, as well as in the SEM image shown in figure 3-6 from Haines et al., 2013, we first see evidence for possible initial development of Riedel shears, similar to observations in previous studies (figure 3-6) (Logan and Rauenzahn, 1987; Logan et al., 1992; Haines et al., 2013). The CT images for p4915 reveal large aggregates of smectite relative to the individual quartz grains. In p4913, after the layer has been sheared to a shear strain of ~21, our SEM images show evidence for much more pervasive Riedel shears as well as some possible Y- and boundary shears. This is, however, a fairly loose interpretation as we were not able to polish the samples. However, the corresponding image from Haines et al., 2013 shows a

similar evolution to much more pervasive Riedel shears and some possible, throughgoing Y-shears. In addition, in p4913, we see a dramatic evolution of the grain size deformation as the clay aggregates become smeared out, which is likely a result of clays lining pervasive shear fabrics.

3.5 Discussion

Our experiments suggest a progression of dominant micromechanical processes with shearing, which can be linked to the evolution of porosity, friction, wavespeeds, and elastic moduli. Though porosity decreases continuously with shear, both the coefficient of friction and elastic properties exhibit a peak and subsequent decay. Scanning electron microscope (SEM) images from previous studies (Haines et al., 2013; Wojatschke et al., 2016) also indicate an evolution of shear planes within the gouge throughout shear. Specifically, Haines et al., 2013 observed fabric formation beginning with boundary shears and Riedel shears first forming at the peak coefficient of friction, and then continuously becoming more throughgoing and rotating to lower angles (figure 3-6). We observe similar trends in our SEM images and CT scans (figure 3-6). Haines et al., 2013 hypothesized that this evolution in fabric greatly affected the coefficient of friction, causing an initial peak and then decay as fabrics became more pervasive, and may have affected the progression of ultrasonic velocities. Here, we have further investigated the trends that Haines et al., hypothesized by using their observed fabrics in addition to our own SEM images and CT scans, to analyze our ultrasonic data in concert with porosity data and elastic moduli calculations. We made multiple attempts to collect SEM images of our sheared wafers but we were unable to fully impregnate the samples with epoxy and, therefore, rely on a combination of our images as well as past works from Haines et al., 2013 and Saffer et al., 2001 to form our hypotheses. Ultimately, we hypothesize that decreasing porosity (and associated strengthening of

grain contacts) competes with the development of shear fabrics as the dominant factors controlling the coefficient of friction and elastic properties of the gouge.

3.5.1 Evolution of friction and wavespeeds

The trends we observe in the coefficient of friction during shear are similar to those reported in previous studies, and have been attributed to the evolution of fabric (Logan et al., 1979; Wang et al., 1980; Logan and Rauenzahn, 1987; Saffer and Marone, 2003; Collettini et al., 2009; Haines et al., 2009, 2013; Ikari et al., 2009, 2011; Niemeijer et al., 2010; Tembe et al., 2010; Carpenter et al., 2011; Wojatschke et al., 2016). We interpret the increase in the coefficient of friction during initial shear loading as a response to grain reorganization and compaction (Figure 3-5), as evidenced by a rapid decrease in both porosity and layer thickness (Figure 3-4). As the peak in friction is approached, the development of and increasing localization of slip along shear planes coincides with the peak and a gradual reduction of friction to a steady state during our Stages 2 and 3 (Wu et al., 1975; Wu, 1978; Wang et al., 1980; Saffer and Marone, 2003; Collettini et al., 2009; Haines et al., 2009; Niemeijer et al., 2010; Tembe et al., 2010; Carpenter et al., 2011; Ikari et al., 2011; Wojatschke et al., 2016). Our Stage 4 represents the emergence of steady state (residual) friction values as shear strain reaches values of ~20-25. Based on previous studies that observed fabric formation and evolution, such as Haines et al., 2013, and our own SEM images and CT scans, we suggest that the pervasive shear planes (including R-, P-, and Y-shears) formed during stage 4 serve as planes of weakness that control the gouge layer friction (figure 3-6).

3.5.2 Elastic moduli and fabric development

The variations in P- and S-wave velocity we observe during shear reflect the evolving layer density, porosity, and possible grain size reduction, in tandem with the formation of shear bands and possible force chains that act in concert to control the bulk elastic moduli (Hadley, 1976; Nur et al., 1998; Popp and Kern, 1998; Jia et al., 1999; Schubnel et al., 2003; Fortin et al., 2005, 2007; Knuth and Marone, 2007; Khidas and Jia, 2012; Knuth et al., 2013; Kaproth and Marone, 2014). Porosity loss and compaction are most often cited as the dominant factors controlling changes in ultrasonic and mechanical properties, both during consolidation alone (e.g., Gettemy et al., 2004), and during shearing (Hadley, 1976; Popp and Kern, 1998; Jia et al., 1999; Schubnel et al., 2003; Fortin et al., 2005, 2007; Khidas and Jia, 2012; Knuth et al., 2013; Kaproth and Marone, 2014). However, the peak and decay to residual coefficient of friction values during stages 2 and 3 in our experiments is accompanied by continued compaction, but also by clear decreases in wavespeed and elastic moduli, indicating that porosity loss is not an exclusive control on these properties (Figure 3-5).

We interpret the evolution of elastic properties and wavespeeds - as well as friction - during shear to reflect the combined effects of compaction and development of fabric in the gouge layer. The evolution of elastic properties with porosity reduction provides insight into the competing roles of compaction as a mechanism to increase grain contact quality and quantity, and departures from a compaction trend that reflect enhanced grain contacts, increased or decreased contact area, force chain development, and the formation of shear planes that decrease the quality of wave propagation across the layer. Previous studies have found evidence in agreement with this hypothesis. For example, Khidas and Jia, 2012 and Knuth et al., 2013 found evidence in V_p and V_s data that decreased grain contact quality, or, decreased coordination number (the mean number of contacts per grain), led to a decrease in ultrasonic velocities,

whereas an increase in grain contact quality would result in increases in V_p and V_s . Knuth et al., 2013 also discussed that the destruction of longer force chains that support a large load could lead to shorter force chains with more complex geometries, causing a decrease in V_p and V_s similar to the decrease we observe in stage 3. Both Jia et al., 1999 and Khidas and Jia, 2012 agree that force chain evolution can have significant effects on elastic properties. In addition, Haines et al., 2013 hypothesized that force chains in their clay-rich gouges caused decreases in velocities and Tembe et al., 2010 also hypothesized that force chains in clay-rich gouges could still support some load in the gouge.

In our stage 1, porosity appears to control the elastic moduli (and hence the evolution of V_p and V_s) as suggested by the rapid decrease in porosity paired with an increase in V_p , V_s , K , and G (Figures 3-7 and 3-8). During this initial shear loading, grain rearrangement and possible grain size reduction leads to increased contact quality and quantity, and drives increasing layer stiffness. During stage 2, we interpret a continued increase in wavespeeds and elastic moduli coupled with a rapid decrease in porosity to indicate that porosity remains the primary control on elastic properties. This is also consistent with the reduction in strength from peak friction toward a residual value over this range of shear strain, which has been interpreted in previous studies to reflect alignment of grains and initial fabric formation that may lead to stronger grain contacts (Figure 3-7 and 3-5). As mentioned above from Knuth et al., 2013 with similar experimental conditions and parameters, the formation of long force chains may also play a role in stiffening during Stage 2 (Jia et al., 1999; Khidas and Jia, 2012; Knuth et al., 2013; Kaproth and Marone, 2014). Long, load supporting force chains have been observed and/or hypothesized in a range of materials, apparatus, and load, including in experiments with smectite-rich gouges (Jia et al., 1999; Tembe et al., 2010; Khidas and Jia, 2012; Knuth et al., 2013; Haines et al., 2013).

The onset of our Stage 3 marks a departure from this trend, with V_p , V_s , and elastic moduli all decreasing even as the gouge continues to densify and porosity continues to decrease

(Figures 3-5 and 3-8). The coefficient of friction also continues to decrease and approaches a residual value during this stage. The decreasing coefficient of friction, paired with decreasing elastic moduli, suggests that the formation of throughgoing shear planes (as observed in Haines et al., 2013) become an important control on the gouge elastic and mechanical properties (Fortin et al., 2007; Khidas and Jia, 2012; Knuth et al., 2013; Haines et al., 2013; Kaproth and Marone, 2014). Based on the decrease in elastic moduli, we infer that as pervasive fabrics are forming, the layer becomes less stiff in the direction of wave propagation (normal to shear, and normal to most fabric elements). We attribute this to throughgoing shear planes that simultaneously weaken the gouge in shear and, similar to the effect of cracks embedded in an elastic medium, decrease the efficiency of acoustic energy propagation normal to the dominant shear plane orientation (Eshelby, 1957, 1961, 1963; Budiansky and O'Connell, 1976). The fabrics formed perpendicular to the direction of wave propagation should also cause the ultrasonic wave to attenuate more and have a higher reflection coefficient, and, therefore, lead to decreased amplitudes. The effect of shear plane formation in reduction of layer stiffness may also be enhanced by the breakdown of force chains that developed during Stage 2 and the development of smaller, more complex force chains, as discussed above and in Knuth et al., 2013. We note that porosity continues to decrease during Stage 3, albeit more slowly than in Stages 1 and 2 (Figures 3-4 and 3-7). The simultaneous porosity decrease and decrease in elastic moduli indicate that porosity loss and compaction are not the primary controls on elastic properties during Stage 3.

By stage 4, the gouge layer has reached steady state residual friction. During these later stages of shearing, V_p , V_s , and elastic moduli all increase, indicating a significant stiffening of the layer (Figure 3-8). The increase in elastic moduli is paired with rapid porosity reduction, suggesting that porosity loss and compaction again become the dominant controls on elastic and mechanical properties. As the layer thickness and porosity continue to decrease, contact stiffness,

quality, and quantity have likely greatly increased, particularly in the platy, aligned clay particles (Khidas and Jia, 2012; Knuth et al., 2013).

3.5.3 Implications for Shear Fabrics and Micromechanical Processes

Modeled after Haines et al., 2013 and Logan and Rauenzahn, 1987, in figure 3-9 we present our interpretation of micromechanical processes controlling the elastic and mechanical responses of clay-rich gouge to shear. Based on our observations and SEM images from Haines et al., 2013, we hypothesize that during Stage 1, few fabrics and shear planes have formed which is consistent with increasing wavespeed, elastic moduli, and decreasing layer porosity, all suggestive of grain reorganization and possible force chain development that enhances grain contacts and stiffens and strengthens the gouge. During this stage, porosity loss controls the mechanical and elastic responses of the gouge. Stage 2 likely exhibits the first formation of shear fabrics, including P- and Riedel shears, coincident with the decrease in coefficient of friction from peak values (figure 3-6) (Logan et al., 1979; Logan and Rauenzahn, 1987; Haines et al., 2013). As noted above, we suggest that these shear planes are sufficiently developed to begin controlling the frictional response, but not yet pervasive or mature enough to control wave propagation or the elastic response (e.g., V_p still increases at the onset of Stage 2; Figures 3-5 and 3-9). This is also supported by our CT scans of p4915 at the onset of stage 2 paired with our SEM images (figure 3-6) in which though we can see some possible Riedel shears (SEM images), clay particles are still forming in aggregates and, therefore, Riedels are likely not throughgoing as they would be lined with clay particles. Although clay fabrics on rough surfaces are difficult to image, focused ion beam slicing paired with scanning electron microscope imaging demonstrates that at very small scales (20 μm) shear surfaces in smectite-rich gouges contain aligned clay fabrics, and this has been interpreted a mechanism for frictional weakening (Wojatschke et al., 2016). In

addition to the platy nature and alignment of clays, Haines et al., 2013 also finds that the ability of fine-grained, smectite-rich gouges to form narrow Riedel shears also facilitates significant weakening of clay-rich gouges (Haines et al., 2013 and figure 3-6). If this is the case for our gouge layers, it may provide an explanation for the onset of frictional weakening that accompanies shear fabric development during Stage 2.

Based on our frictional data, ultrasonic velocities, and SEM images from Haines et al., 2013, we infer that in Stage 3, Y-shears appear and boundary shears become more throughgoing, in addition to pervasive P- and Riedel shears. The onset of Stage 3 marks a continued decrease in the coefficient of friction, as V_p begins to decrease from a peak value. The correlation of Y-shears - which are oriented parallel to the slip direction - with decreasing wavespeeds and elastic moduli during Stage 3 supports the idea that these shear planes are a primary control on wave propagation normal to the layer. As noted above, the fact that V_p , V_s , G , and K all decrease in this stage, yet the layer continues to compact with progressive shear, is a departure from expected evolution of elastic properties with porosity loss (Mavko and Nur, 1979; Nur et al., 1998; Dvorkin et al., 1999; Bachrach et al., 2000; Mavko et al., 2009; Knuth et al., 2013; Kaproth and Marone, 2014) and provides clear evidence that at this stage of our experiments, shear fabrics become a dominant control on wavespeeds and moduli. In contrast, during stage 4 (Figures 3-9 and 3-6), we hypothesize that fabrics and shear planes become increasingly pervasive and the layer thins dramatically as the layer reaches a steady state residual friction, and wavespeeds and elastic moduli increase. We see evidence for this in our SEM images, SEM images from Haines et al., 2013, and our CT scans as the SEM images show many, low angle Riedel shears and Y-shears and the CT scans show that the clay has become much more smeared throughout the sample, likely because it is lining shear surfaces. Although fabrics and shear planes are likely abundant at this stage (Riedel shears, P-shears, Y-shears), it appears that porosity loss and compaction control both the elastic and mechanical properties at these higher shear strains.

3.6 Conclusions

We conducted shearing experiments with gouge composed of 50% smectite and 50% granular quartz to investigate the role of progressive shearing and fabric development in controlling the evolution of friction, porosity, V_p , V_s , and bulk and shear moduli. Though porosity loss is often cited as a primary control on elastic properties (Mavko and Nur, 1979; Nur et al., 1998; Dvorkin et al., 1999; Bachrach et al., 2000; Mavko et al., 2009; Knuth et al., 2013; Kaproth and Marone, 2014), we show that at different stages of shearing, fabric formation and other micromechanical processes are also important factors. As fabrics and shear planes form in the gouge layers, they compete with compaction as the dominant control on elastic and frictional properties. After the coefficient of friction reaches peak values, we infer that the formation of fabrics begins to weaken the gouge layer. However, it is not until fabrics and shear planes are further developed and become perpendicular to the direction of wave propagation that they become a dominant control on wavespeed and elastic properties. Finally, once the coefficient of friction reaches steady state (controlled primarily by the strength of shear planes and fabrics), porosity once again becomes the dominant control on further changes in V_p , V_s , amplitude, and V_p/V_s , all of which continue to increase with progressive shearing.

Our results highlight the importance of micromechanical processes in governing the evolution of elastic properties in fault zones, in addition to their well-studied effects on frictional behavior (Logan et al., 1979; Logan and Rauenzahn, 1987; Collettini et al., 2009; Niemeijer et al., 2010; Tembe et al., 2010; Knuth et al., 2013; Haines et al., 2013; Kaproth and Marone, 2014; Wojatschke et al., 2016). Because the development of pervasive fabrics is a key factor in defining fault elastic properties, we expect that variations in fabric and fault structure with progressive slip, or during the seismic cycle, will act as an important control on sliding stability through their effect on fault stiffness (Scholz, 2002; Leeman et al., 2015, 2018; Scuderi et al., 2017), in

addition to the effects of fabrics directly on frictional properties. In addition to fault sliding stability and stiffness, fabric driven changes in velocity also need to be considered when interpreting fault zone seismic properties such as reflectivity and velocity. Though low velocity zones within fault zones are most often interpreted to be the result of low stress, fault zone damage, or preserved porosity (Mooney and Ginzburg, 1986; Li et al., 1998, 2004, 2015; Li and Vidale, 2001; Unsworth and Bedrosian, 2004; Audet et al., 2009; Bangs et al., 2009; Tudge and Tobin, 2013), fabric formation may also contribute to decreases in velocity.

Acknowledgements: We thank S. Swavely for technical help in the laboratory and David C. Bolton, Srisharan Shreedharan, Parisa Shokouhi, and Charles Ammon for key discussions. We gratefully acknowledge support from the GDL Foundation, DOE geothermal program (DOE EERE DE-EE0006762) and the NSF Geophysics program (NSF-EAR award 1215856 to D.S. and C.M EAR-1520760 and EAR-1547286/1547441). Data available from authors.

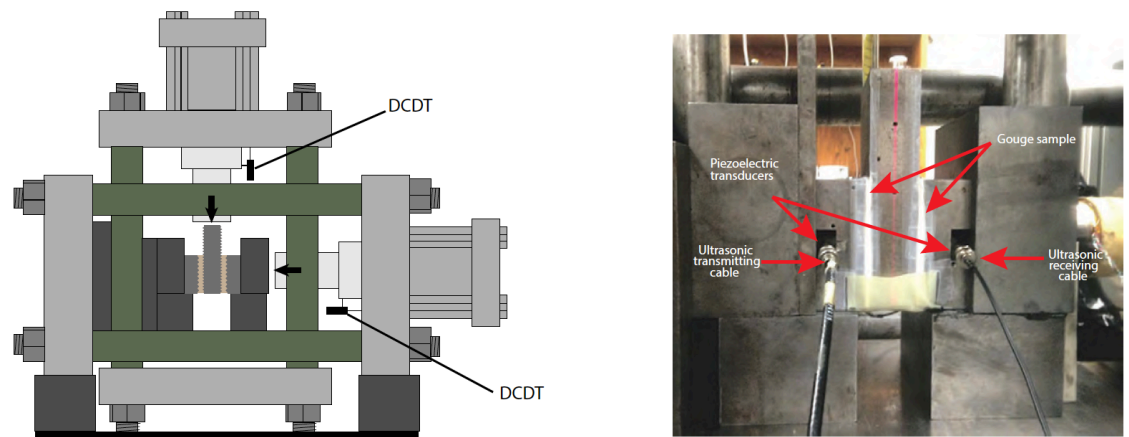


Figure 3-1: Left: Schematic of biaxial deformation apparatus with double direct shear sample. Right: Double direct shear sample with ultrasonic cables connected to piezoelectric transducers.

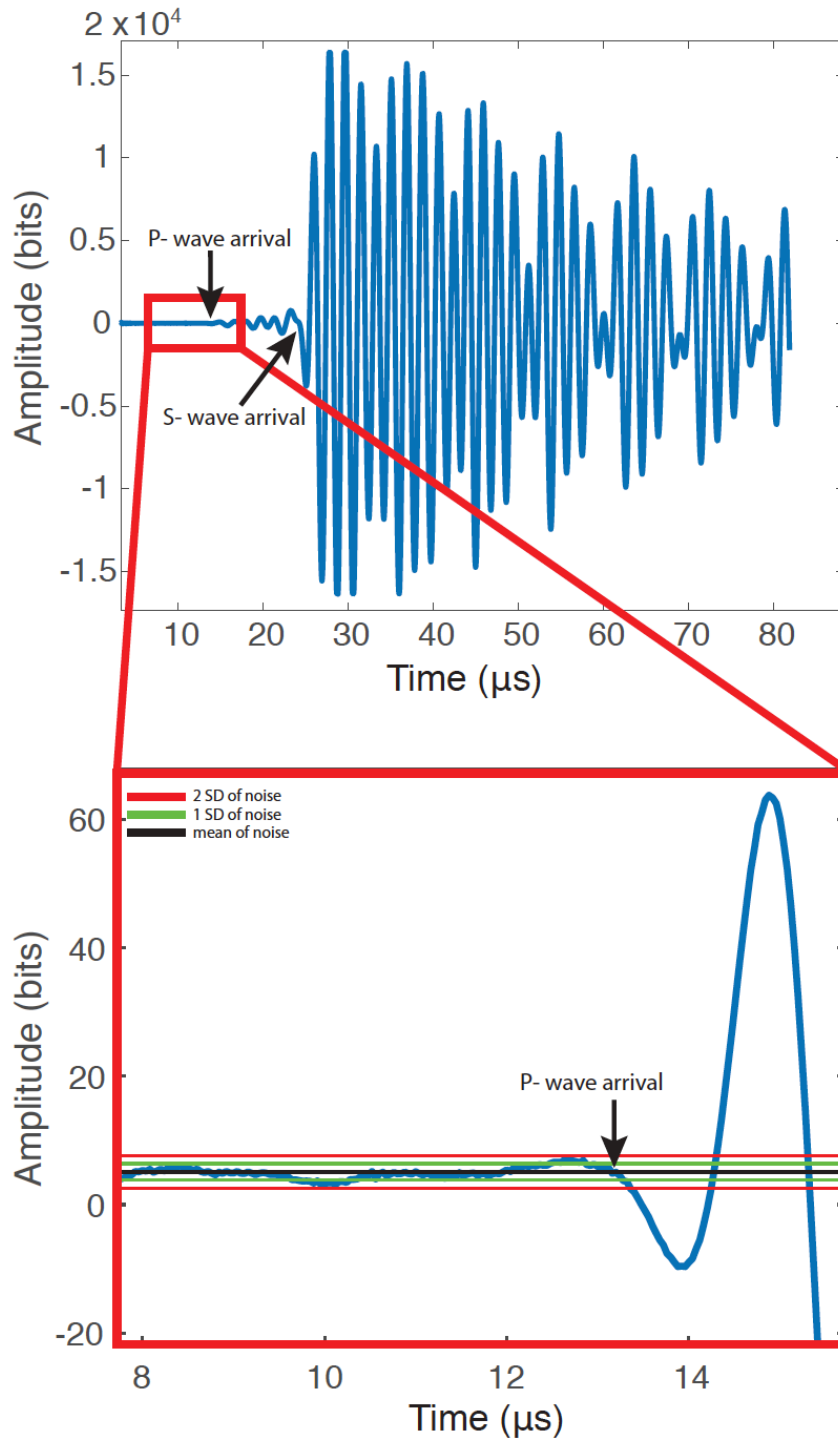


Figure 3-2: Example waveform from experiment p4830. P and S wave arrivals times are picked at the zero-crossing (relative to the signal mean, black line). A master wave is picked for each experiment and the evolution of arrival times as a function of shear are determined via cross correlation.

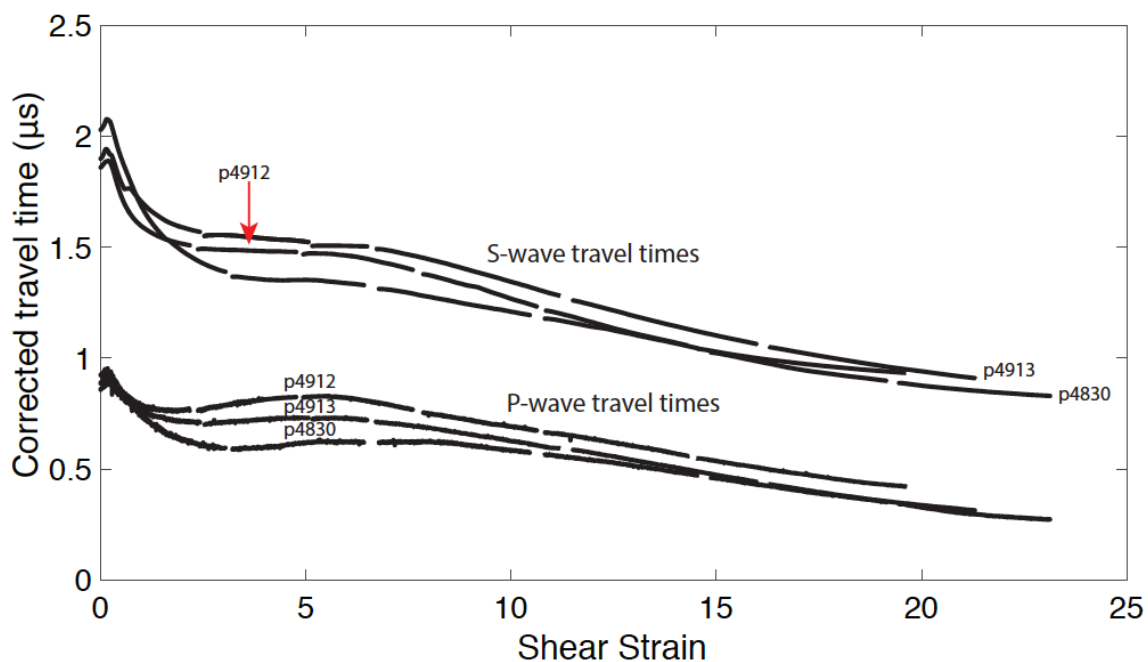


Figure 3-3: Travel times for P- and S-waves through two layers of fault gouge. These data are determined from waveforms (Figure 3-2) and calibrations to account for the travel time through the loading platens and sample assembly. Note that wave speed increases rapidly during initial shear, up to strain of ~ 3 , due to shear enhanced gouge compaction and then evolves more gradually with strain. Gaps in the data are associated with mechanical offsets of the experimental apparatus.

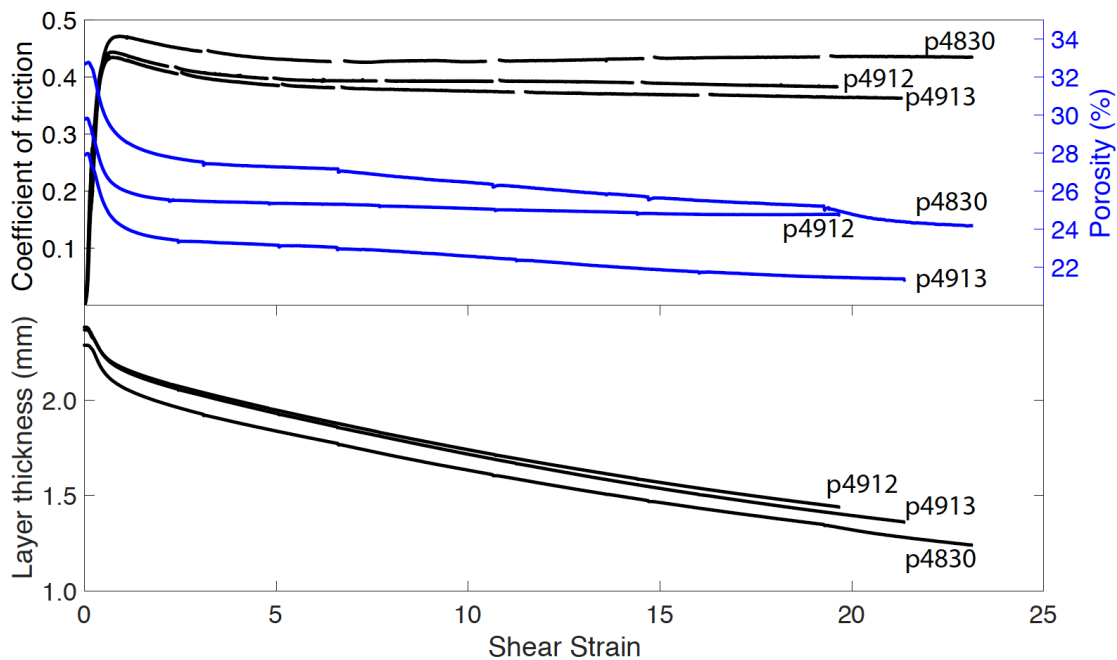


Figure 3-4: Coefficient of friction, porosity, and layer thickness as a function of shear strain for three complete experiments. Changes in porosity mirror changes in the coefficient of friction, showing rapid evolution followed by gradual changes. Gouge layers thin rapidly upon initial shear and then exhibit steady state thinning associated with geometric spreading.

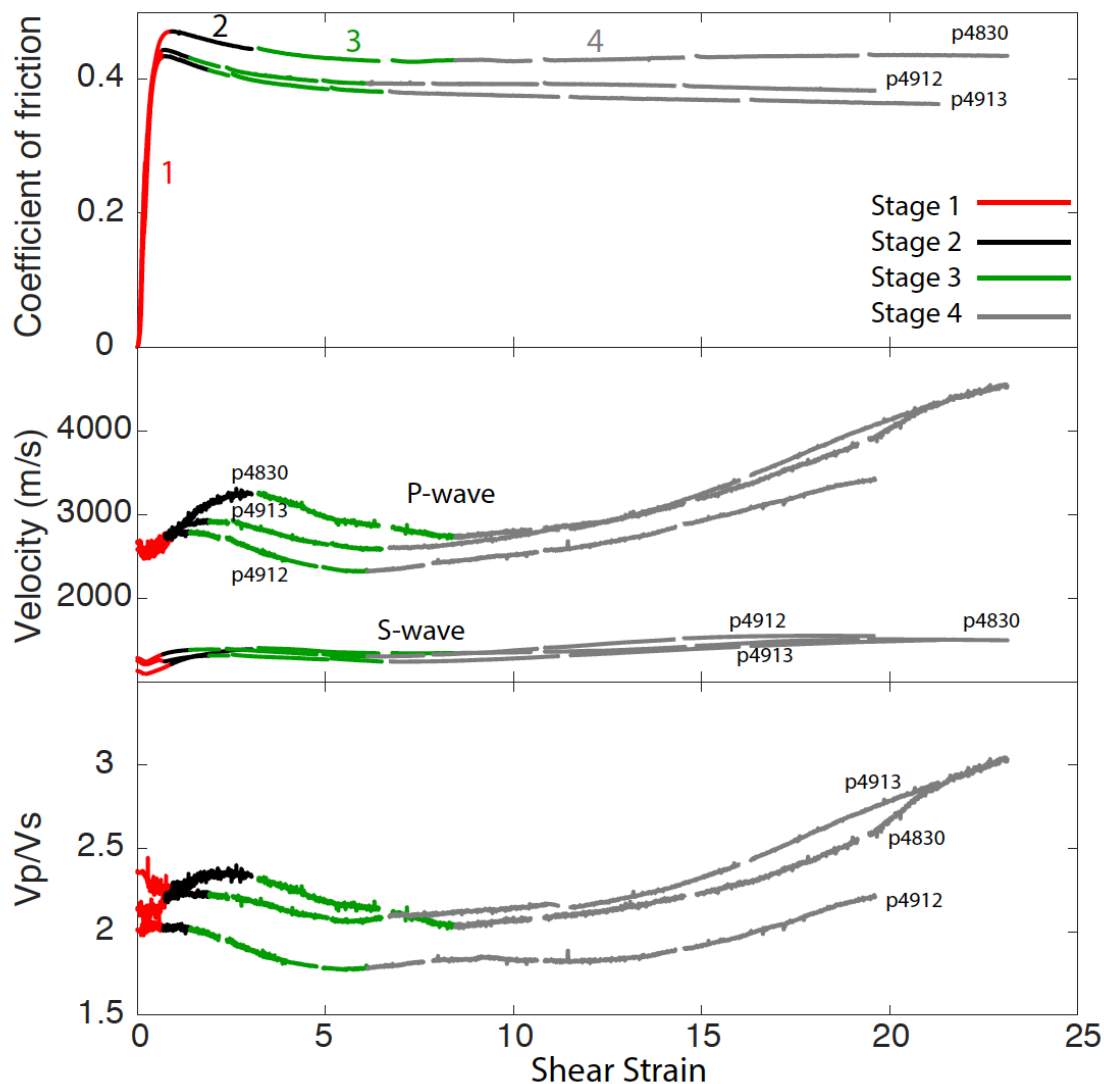
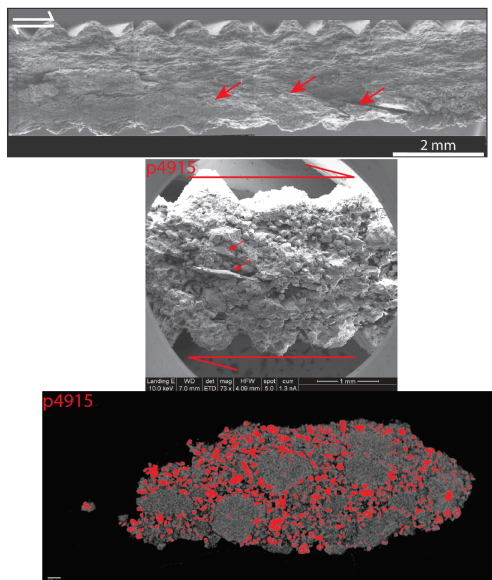


Figure 3-5: Data for three complete experiments showing four stages of evolution in friction and elastic wave speed. Stage 1 (red) shows an increase in all properties during shear loading. Stage 2 (black) begins when friction first decreases after the peak strength, which coincides with increases in V_p , V_s , and V_p/V_s that are interpreted to result from shear fabric formation. Stage 3 (green) begins at the peak value of V_p and occurs during frictional weakening which is interpreted to result from fabric intensification and alignment parallel to the shear direction. The beginning of Stage 4 (gray), is defined when V_p begins increasing again. In State 4, friction has reached a steady state value and wave speeds increase as the layer compacts and densifies.

At peak friction (onset of stage 2)
 Top: SEM image from Haines et al., 2013 - strain ~ 1.7
 Middle: SEM image - strain ~ 0.5
 Bottom: CT scan, quartz grains shown in red - strain ~ 0.5



At residual friction (stage 4)
 Top: SEM image from Haines et al., 2013 - strain ~ 19
 Middle: SEM image - strain ~ 21
 Bottom: CT scan, quartz grains shown in red - strain ~ 21

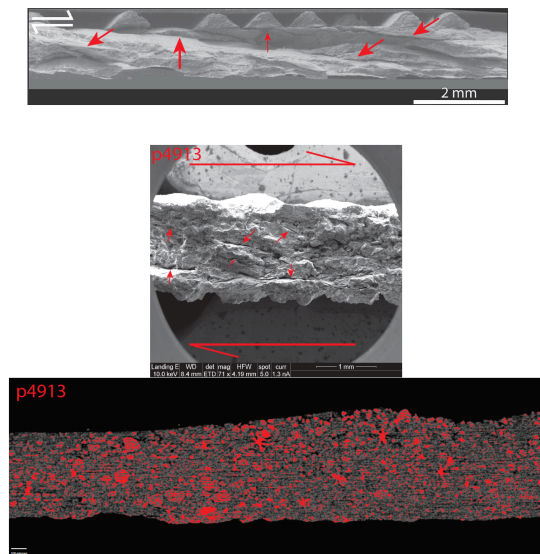


Figure 3-6: Left: Images of sheared wafers at peak friction (at the onset of stage 2). Right: Images of sheared wafers at residual friction. The top image on the left and right is modified from Haines et al., 2013 and is an image of sheared chlorite schist sheared at a normal stress of 20 MPa and shearing velocity of $\sim 11 \mu\text{m/s}$. The middle two images are SEM images of sheared wafers from experiments in this study (p4915 and p4913). The bottom images are also from p4915 and p4913 and are CT scans of the same face that is shown in the middle images. Quartz grains are highlighted in red. The top two images on the left and right show possible shear planes evolving with shear. The left images, before peak friction and at the onset of stage two show the formation of a few Riedel shears as shown by the red arrows. The CT scan shows large aggregates of smectite forming, indicating that while there are likely some fabrics, they are not throughgoing enough for all of the clay in the sample to line them. The right images, at residual friction, show many shear planes as shown by the red arrows. As these fabrics rotate more perpendicular to the direction of wave propagation and become more through-going, they cause a decrease in the ultrasonic velocities. The CT scan of p4913 shows that the clay has smeared throughout the sample and is likely lining throughgoing fabrics.

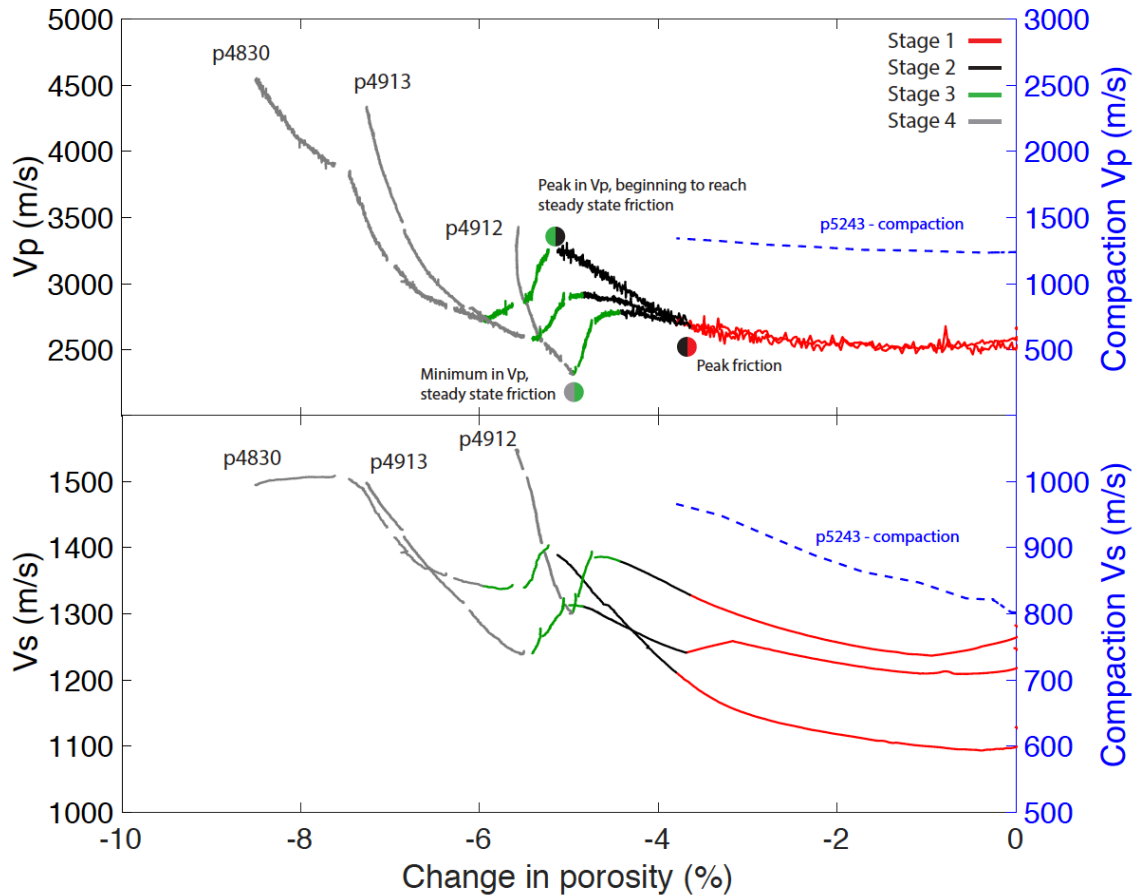


Figure 3-7: Evolution of elastic wave speeds with porosity for three complete experiments, showing the four stages defined in Figure 3-5. The dashed blue curves show V_p and V_s evolution as a function of change in porosity for an experiment (p5243) where only normal stress was increased (0 - ~65 MPa) and there was no shear. Therefore, the trend shown in the blue curves is the change in velocity due only to compaction. Any trend that deviates from p5243 indicates that processes other than compaction are occurring. Both V_p and V_s increase during porosity reduction except for Stage 3 (green). The reduction in V_p and V_s during bulk gouge densification (Stage 3) suggests that shear fabric formation can reduce elastic modulus or density locally within the shear bands.

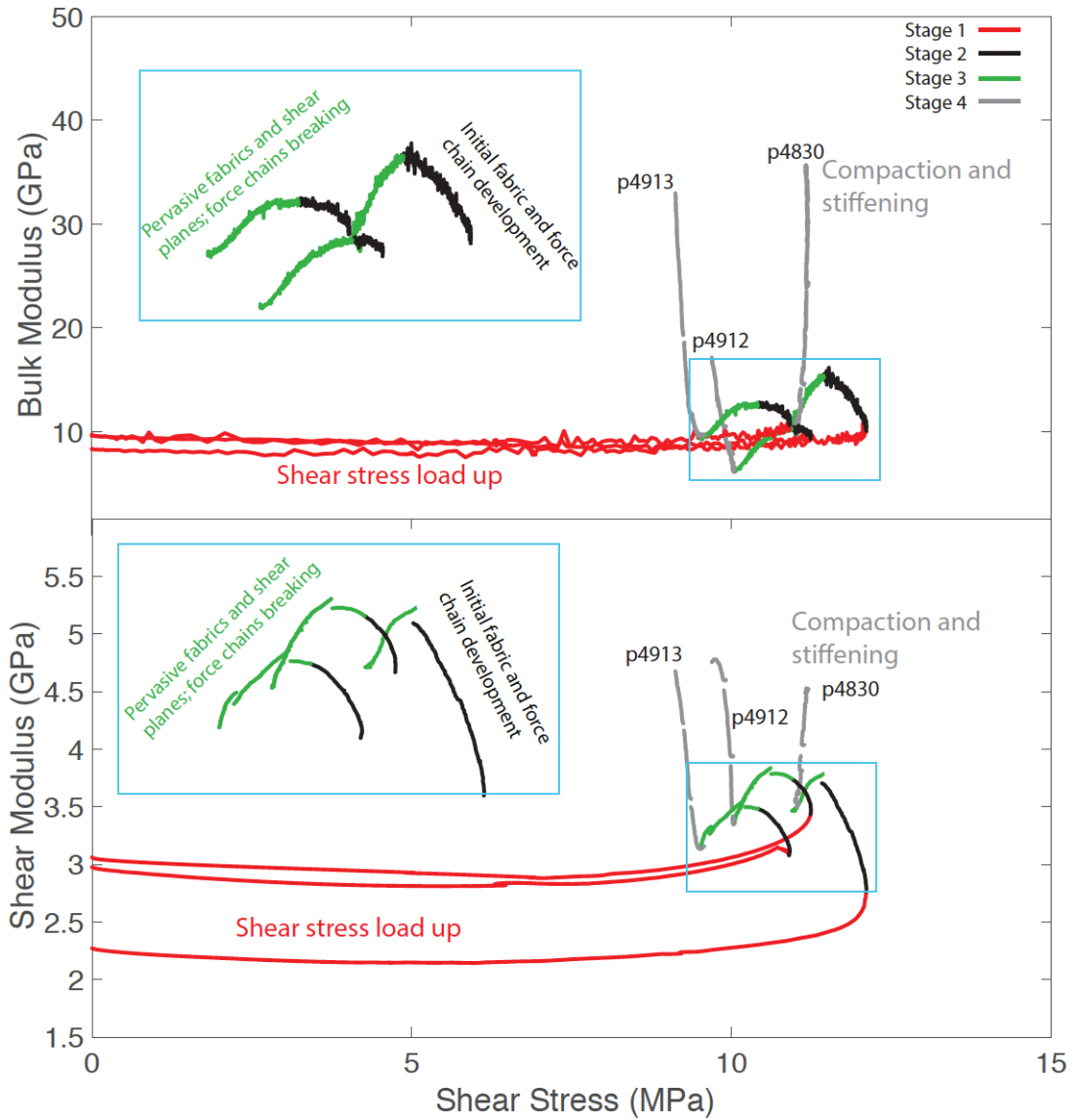


Figure 3-8: Shear and bulk modulus as a function of shear stress showing the four stages defined in Figure 3-5. Evolution of the moduli provide insight into micromechanical processes within the layer. Bulk and shear modulus are relatively constant during Stage 1 and then begin to increase as grains rearrange and contact quality and quantity increase. Stage 2 exhibits an increase in bulk and shear modulus as fabrics initially develop and force chains form. Increased fabric formation also may enhance grain contacts. Stage 3 displays the only decrease in shear and bulk modulus as fabrics become more pervasive and longer force chains formed in Stage 2 begin to break down, decreasing the stiffness and rigidity of the layer. Stage 4 exhibits a large increase in shear and bulk modulus as fabrics become more pervasive and the layer further compacts, creating an increase in grain contact quantity and quality.

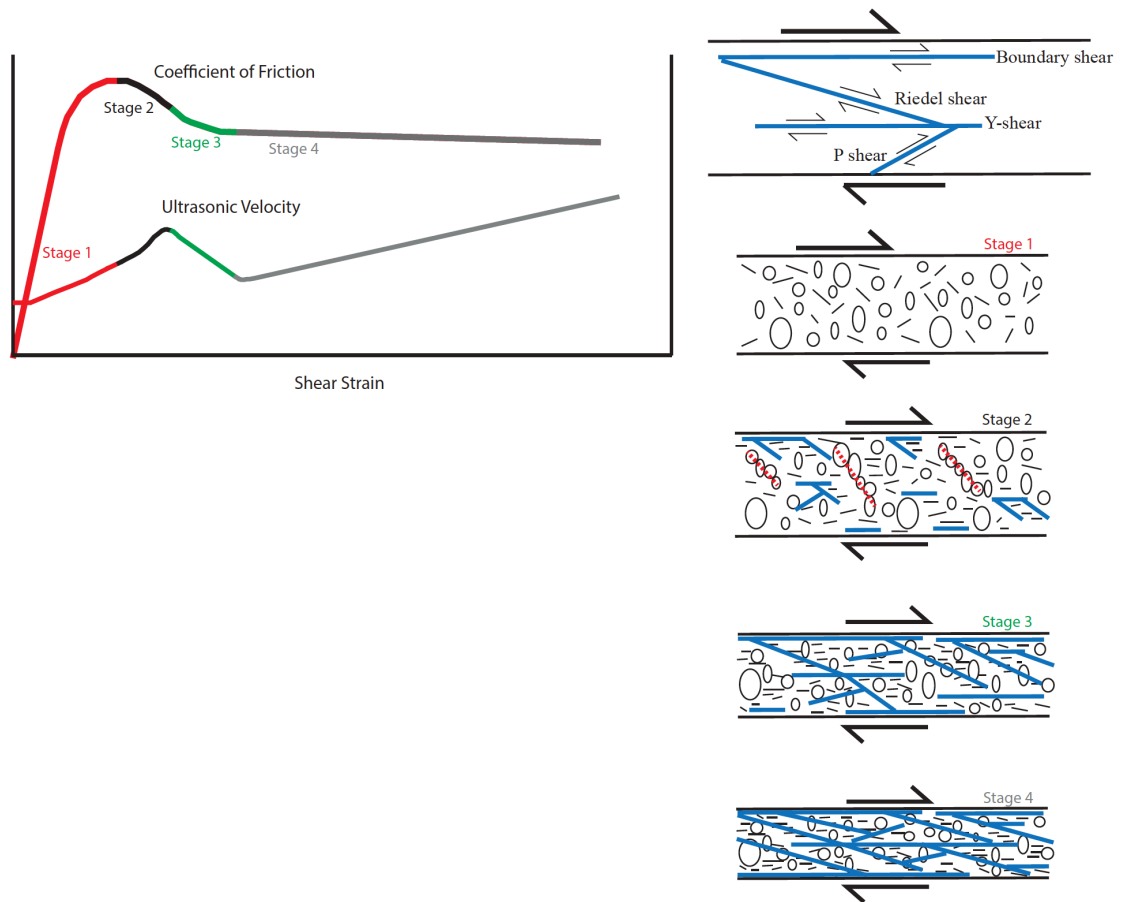


Figure 3-9: After Haines et al., 2013 and Logan and Rauenzahn, 1987. Hypothesized micromechanical processes occurring with the gouge layer during shear. During stage 1 (red) few fabrics have formed and grains are reorganizing during shear stress load up. Compaction controls the mechanical and elastic responses of stage 1. Stage 2 (black) begins at peak friction and marks the onset of Riedel shears, boundary shears, and Y-shears, causing a decrease in the coefficient of friction. It is possible that long, compliant force chains form during stage 2. While fabric formation weakens the coefficient of friction and controls mechanical properties, compaction still controls elastic properties. During stage 3 (green), we observe further weakening within the layer causing a decrease in V_p and V_s as Riedels, P-shears, boundary shears, and Y-shears grow throughout the layer rotate to become perpendicular to the direction of wave propagation. The evolution of fabrics controls both mechanical and elastic properties during stage 3. Stage 4 (gray) marks steady state friction and a continuous increase in V_p and V_s as Riedels, Y-shears, and boundary shears are throughgoing and well developed. Further compaction controls the mechanical and elastic properties of stage 4.

Table 3-1: List of experiments, including calibration experiments (bolded experiment numbers are shown in the figures)

Exp. #	Peak μ	Initial thickness /compacted thickness of single layer (mm)	Final shear strain	Initial mass (g)	Measured mass loss (g)	Predicted mass loss (g)	Threshold value for ultrasonic velocities (P-/S-wave)	Notes
p4808	0.49	5/2.35	11.8	118.28	33.41	32.92	N/A	Periodic mass loss measured
p4830	0.47	5/2.29	23.1	112.0	31.79	32.2	.81/.81	Periodic mass loss measured
p4853	N/A	23/12.125	0	N/A	N/A	N/A	N/A	No shear. Solely for calibration of acoustic side blocks.
p4867	0.47	3/0.835	63.2	N/A	N/A	N/A	N/A	Solely for calibration of acoustic side blocks.
p4912	0.44	5/2.385	19.7	116.51	30.05	29.34	.81/.75	Periodic mass loss measured
p4913	0.43	5/2.37	21.3	118.63	33.0	30.81	.88/.75	Periodic mass loss measured
p4914	0.43	5/2.33	1.2	N/A	N/A	N/A	N/A	Experiment stopped right after peak friction to capture fabrics
p4915	N/A	5/2.245	0.4	N/A	N/A	N/A	N/A	Experiment stopped before peak friction to capture fabrics (Fig. 3-6)

p4916	N/A	5/2.31	0.2	N/A	N/A	N/A	N/A	Experiment stopped before peak friction to capture fabrics
p4947	0.41	8/3.91	14.6	N/A	N/A	N/A	N/A	Solely for calibration of acoustic side blocks
p4962	0.41	8/3.87	14.8	N/A	N/A	N/A	N/A	Solely for calibration of acoustic side blocks
p4977	0.44	7/3.13	23.2	N/A	N/A	N/A	N/A	Solely for calibration of acoustic side blocks
p5243	N/A	5/3.015 (5 MPa)	N/A	N/A	N/A	N/A	.88/.88	Compaction test (Fig. 7)

Chapter 4

Evolution of Elastic and Mechanical Properties during Fault Shear: The Roles of Clay Content, Fabric Development, and Porosity

Abby R. Kenigsberg¹, Jacques Rivière², Chris Marone¹, Demian M. Saffer¹

¹Department of Geosciences and Center for Geomechanics, Geofluids, & Geohazards, The Pennsylvania State University, University Park, Pennsylvania 16802, USA

²Department of Engineering Science and Mechanics, The Pennsylvania State University, University Park, Pennsylvania 16802, USA

4.1 Abstract

Phyllosilicate minerals are known to weaken fault zones due to the formation of shear fabrics and clay alignment. Although the effects of clay abundance and shear fabrics on the coefficient of friction, sliding stability, and porosity evolution of faults are well-studied, their influence on ultrasonic velocities (V_p and V_s) and elastic moduli are less well known. V_p , V_s , and elastic moduli provide key insights to fault stiffness and seismic cycle properties and, therefore, any effect that fabrics have on these properties are vital to understand. Smectite content is the most important factor in determining whether fabric or porosity controls the elastic responses. To investigate the interplay between gouge composition, shear fabric, and porosity in governing fault zone elastic properties, we conducted a suite of direct shear experiments on synthetic smectite-quartz fault gouges with smectite contents ranging from 10-100 wt%. We also tested sediment incoming to the Sumatra subduction zone that represents the protolith for the plate boundary thrust (recovered on International Ocean Discovery Program Expedition 362). We sheared the gouges at a normal stress of 25 MPa, a velocity of ~ 20 $\mu\text{m/s}$, and to shear strains up to 30. We

monitored compressional and shear wave velocities (V_p , V_s) throughout shearing, while concurrently measuring the evolution of friction and porosity; from V_p , V_s , and density, we compute shear (G) and bulk (K) moduli. We find that mechanical and elastic properties for synthetic samples with abundant smectite (>70%) are almost entirely controlled by fabric formation, resulting in decreases in the coefficient of friction, V_p , V_s , K , and G with shear. Though fabrics control the elastic response of smectite-poor gouges (<50%) and cause a decrease in velocities and moduli over a narrow range of intermediate shear strains, porosity is the primary control throughout the majority of shearing, resulting in large increases in velocities and elastic moduli with shear. The Sumatra sediments have fairly low smectite content (8% and 19%) and behave similarly to the smectite-poor synthetic gouges. Elastic properties (V_p , V_s , K , G) vary systematically with smectite content with high smectite gouges having initial elastic property values of, $V_p \sim 1300\text{-}1800$ m/s, $V_s \sim 900\text{-}1100$ m/s, $K \sim 1\text{-}4$ GPa, and $G \sim 1\text{-}2$ GPa and low smectite gouges having initial elastic properties of $V_p \sim 2300\text{-}2500$ m/s, $V_s \sim 1200\text{-}1300$ m/s, $K \sim 5\text{-}8$ GPa, and $G \sim 2.5\text{ GPa} - 3$ GPa. Overall we find that, even in low smectite gouges, smectite and shear fabrics can affect the stiffness and elastic properties of fault gouges. Shear fabrics, which cause mechanical and frictional weakening, also cause destiffening in elastic moduli implying that abundant amounts of smectite within fault zones may lead to much weaker and more compliant faults relative to fault zones formed in stronger minerals.

4.2 Introduction

Shear fabrics and clay alignment in fault gouges have been connected to dramatic fault weakening (Sisbon, 1977; Logan and Rauenzahn, 1987; Faulkner et al., 2003; Wibberley and Shimamoto, 2003; Saffer and Marone, 2003; Jefferies et al., 2006; Ikari et al., 2009, 2015; Niemeijer et al., 2010; Carpenter et al., 2011; Knuth et al., 2013; Haines et al., 2013; Wojatschke

et al., 2016). These factors, and the presence of smectite clay in particular, have been linked to low friction on major faults, including the San Andreas fault zone (Collettini et al., 2009; Carpenter et al., 2011, 2012; Lockner et al., 2011) and shallow subduction plate boundaries (Wu et al., 1975; Deng and Underwood, 2001; Carpenter et al., 2011, 2012; Ikari et al., 2011; Ujiie et al., 2013; Wojatschke et al., 2016). Fabrics and nano-coatings formed during shear of clay-rich gouges have been identified as a mechanism to reduce fault strength and stability (Schleicher et al., 2006; Collettini et al., 2009; Haines et al., 2009, 2013; Niemeijer et al., 2010; Wojatschke et al., 2016). For example, with increasing clay abundance, synthetic and remolded gouges exhibit an increasingly large peak in friction upon initial shear, followed by a rapid decrease in frictional strength. This peak and subsequent decay is linked to the formation and evolution of shear planes and fabrics (Logan and Rauenzahn, 1987; Saffer and Marone, 2003; Ikari et al., 2009; Knuth et al., 2013; Haines et al., 2013).

While many of the mechanical effects of shear fabrics and clays, and smectite clay in particular, are well studied, there are relatively few studies of the effects of shear fabric and fault structure on the elastic properties of fault zones (Gettemy et al., 2004; Knuth et al., 2013; Carpenter et al., 2014). Elastic waves have been used extensively to monitor changes in elastic properties during seismic cycles both in nature and in laboratory settings (Brenquier et al., 2008; Scuderi et al., 2017), as well as to indirectly document changes in porosity, fault healing, crack sealing, and grain coordination during deformation in fault gouge and granular materials in general (Digby, 1981; Schubnel et al., 2003; Fortin et al., 2005; Mavko et al., 2009; Khidas and Jia, 2012; Knuth et al., 2013; Kaproth and Marone, 2014; Ryan et al., 2018; Shreedharan et al., 2019).

In general, porosity loss (i.e. compaction), stress changes, and fault damage are recognized as primary controls on velocity evolution during deformation and shearing (Hadley, 1976; Mavko and Nur, 1979; Li et al., 1998, 2004; Nur et al., 1998; Popp and Kern, 1998;

Dvorkin et al., 1999; Jia et al., 1999; Li and Vidale, 2001; Unsworth and Bedrosian, 2004; Fortin et al., 2005, 2007; Audet et al., 2009; Mavko et al., 2009; Khidas and Jia, 2012; Knuth et al., 2013; Kaproth and Marone, 2014). However, many recent works have observed more complex variations in elastic properties than a simple monotonic stiffening due to progressive compaction, leading to the hypothesis that shear fabrics play an important role in governing wavespeeds and elastic properties (Haines et al., 2013; Knuth et al., 2013). Nonetheless, the effects of shear fabrics on ultrasonic velocities and elastic moduli have generally not been investigated in detail. It is important to understand the links between fabrics and elastic properties to correctly interpret seismic data that provides key insight into fault stiffness and the seismic cycle.

In this study, we investigate the evolution of the mechanical and elastic properties of a range of synthetic smectite rich clay gouges as well as natural sediment from off the coast of Sumatra collected during International Ocean Discovery Program (IODP) Expedition 362. We conducted a series of direct shear experiments, and report on the evolution of porosity, coefficient of friction, ultrasonic velocities, and elastic moduli during progressive shearing. Focusing on the effects of gouge composition, we discuss: 1) the links between the evolution of coefficient of friction and ultrasonic velocities; 2) the role fabrics play in controlling mechanical and elastic properties; and 3) proposed micromechanical processes controlling the evolution of mechanical and elastic properties throughout shear for a range of clay-rich gouges.

4.3 Materials and Methods

4.3.1 Shearing Experiments

We conducted a suite of double direct shear (DDS) experiments on synthetic smectite-quartz fault gouges ranging in composition from 10 – 100 wt.% Ca-montmorillonite, as well as

experiments on clay-rich sediments from off the coast of Sumatra acquired during IODP Expedition 362. These natural samples sit atop the subducting Indian Plate and represent the “subduction input” materials in which the plate interface eventually forms. We tested two samples of the subduction input sediment containing ~ 20 wt% quartz, ~ 12-13 wt% plagioclase, ~2-3 wt% calcite, ~15 wt% kaolinite + chlorite, and ~50 wt% smectite + illite. One of the samples (362-U1480E-9H-1, 130-150 cm) contained a higher proportion of illite within the smectite-illite fraction (8 wt% smectite + 41 wt% illite), whereas the other (362-U1480F-74X-2, 79-93 cm) contained 19% smectite + 32% illite (Rosenberger et al., 2019). It is important to note that the Sumatra samples have a more complicated composition than our synthetic samples (Table 4-1), including the presence of plagioclase, and containing illite, chlorite, and kaolinite as part of the clay fraction.

In our DDS configuration, two gouge layers are sandwiched between three grooved steel forcing blocks (Figure 4-1). The grooves ensure that shear occurs within the gouge layers and not at the interface of the blocks and gouge layers (Saffer and Marone, 2003; Anthony and Marone, 2005; Knuth and Marone, 2007). The center forcing block is longer than the two side blocks; this allows the nominal surface area to remain constant throughout shear. In addition, steel guide plates are secured to the front and back of the sample to keep gouge from extruding. Using a leveling jig, each gouge layer was constructed to a 5 mm initial layer thickness, except for experiments used for calibrations which had initial thicknesses of 3, 5, 8, and 23 mm (Table 4-1; (Kenigsberg et al., 2019, submitted). Tests were conducted at room temperature and humidity (11.8% - 72.6% relative humidity).

At the start of each test, we applied a layer-normal stress of 25 MPa and allowed the gouge samples to compact until reaching equilibrium (defined on the basis of stabilization of layer thickness), then imposed shear by driving the center block downward at a velocity of 21.5 $\mu\text{m/s}$ to total displacements of ~ 40 – 60 mm. Using horizontal and vertical load cells with a

resolution of ± 0.1 kPa (Kaproth and Marone, 2014), we continuously measured shear and normal stress throughout shear. We determine coefficient of friction by dividing shear stress by normal stress, assuming zero cohesion (Figure 4-3). We also measured shear velocity and layer thickness with direct current displacement transducers (DCDTs) with a resolution of ± 0.1 μm .

Throughout experiments, we measured elastic wavespeed using piezoelectric lead-zirconate-titanate transducers (PZTs, 500 kHz center frequency, 1.27 cm diameter) which are embedded in the side forcing blocks (Figures 4-1 and 4-2). We use a 15-bit data acquisition system and transmit a negative half-sine wave pulse through the DDS configuration every 10 ms throughout the experiment. One shear wave PZT in a side block acts as an ultrasonic transmitter and a PZT in the other side block acts as the receiver; P-waves are generated via mode conversion. We record individual waveforms, but use stacked waveforms during processing to improve signal-to-noise ratio.

4.3.2 Mass Loss and Porosity Calculations

Porosity evolution provides insight into micromechanical processes within the gouge layers and to compute elastic moduli from wavespeeds; hence, continuous monitoring of porosity during shear is a key element of our study (Figure 4-3). In the double direct shear configuration, this is not trivial, because material is lost from the actively shearing region both by entrainment along the center block and by extrusion. We determine porosity using layer thickness measurements in tandem with a mass loss model. We briefly describe our approach to compute porosity as a function of shear strain here, and refer the reader to *Kaproth & Marone, 2014* and *Kenigsberg et al. [2019]* for additional details.

As the layers are sheared, they thin due to both loss of gouge mass from the active shear zone (due to transport with the center block as it moves downward, so called “geometric

thinning”), and densification as the layers compact (Scott et al., 1994). While we are able to continuously monitor layer thickness, we must account for the material lost due to the geometric effect to correctly calculate the evolving mass of the actively shearing gouge material (Kaproth and Marone, 2014). With knowledge of the initial layer mass (measured directly at the time the layers are constructed), we define the bulk density and porosity of the layer throughout shear on the basis of conservation of mass.

We model this mass loss as a rectangular plug of material transported downward and out of the active shear zone with the center block. We first calculate an initial porosity based on known initial layer thickness, volume of sample, and mass of sample before shearing:

$$\rho_i = \frac{M_i}{(2hA) + V_T}$$

and

$$\phi_i = \left(1 - \frac{\rho_i}{\rho_s}\right) \times 100$$

where ρ_i is the initial layer bulk density, M_i is the initial mass, A is the nominal frictional contact area, h is single layer thickness, V_T is the total volume of the grooves in the forcing blocks, ϕ_i is the initial porosity (in percent), and ρ_s is the average solid grain density of the two-phase (or multi-phase for Suamtra sediment) mixture (Table 4-1). For the case of a rectangular plug, the volume and mass lost through shear at any given time, n , are given by:

$$M_{(n)} = M_i - M_L$$

Or

$$M_{(n)} = (\rho_{n-1}V_{n-1}) - (\rho_{n-1}V_L)$$

M_L is mass lost throughout shear, ρ_n is the density of the sample based on mass and volume, and V_L is volume lost throughout shear, given by:

$$V_L = (2hWdy) + (2gv_Tdy)$$

and

$$V = (2hA) + V_T \quad .$$

V_L is volume lost throughout shear, V is the gouge volume that remains in the DDS configuration, dy is the distance sheared, g is the number of grooves/cm, W is the width of the blocks, v_T is the volume of a single tooth in the center block, and V_T is the volume of all of the grooves within the 10 cm X 10 cm shearing area.

Using the initial mass, density, and volume, we derive layer mass throughout shear from the known mass at a given time, M , and the calculated mass lost, M_L , due to sample extrusion. Bulk density and porosity are obtained from this mass, the measured volume of the layer (from layer thickness and known nominal contact area), and the average solid grain density (Kaproth and Marone, 2014; Kenigsberg et al., 2019, submitted). To verify the assumption of rectangular mass loss, we manually measured the material that was extruded with the center block at multiple points during shearing and compared this to our modeled mass loss. The largest discrepancy between the predicted mass loss and the manually measured mass loss was 4 g, or ~3.5 - 4% of the total layer mass.

4.3.3 Ultrasonic Velocities and Elastic Moduli

Using S-wave PZTs, we measured ultrasonic velocities by a time-of-flight technique, using first arrivals of P- and S-waves, layer thickness measurements, and an extensive set of empirical calibrations conducted to determine the wave travel time through the steel forcing block assembly (termed “zero time”, Kenigsberg et al. 2019). To determine arrival times, we conducted manual picks at shear strains from 0 – 20 (Figure 4-2) and compared these with arrival times based on cross-correlation against a master waveform picked at zero shear strain. The time shift between the master waveform and every other waveform throughout the experiment is recorded

and then added to our manually picked arrival time for the master waveform at zero shear strain. Based on our calibrations, we then subtract the zero time to obtain travel times of the P- and S-waves through the gouge layers themselves.

Using these velocities together with bulk densities defined by our mass loss model, we compute elastic moduli throughout shear (Digby, 1981; Kaproth & Marone, 2014; Knuth et al., 2013):

$$G = \rho V_s^2$$

$$K = \rho V_p^2 - \frac{4}{3}G$$

where K is bulk modulus and G is shear modulus.

4.4 Results

4.4.1 Coefficient of Friction

Friction decreases systematically with clay abundance. Peak friction values are $\mu = 0.57 - 0.63$ for 10% smectite and Sumatra samples, and decrease to $\mu = 0.33$ for 90-100% smectite samples (Fig. 4-3a); residual friction values decrease from $\mu=0.59$ for 10% smectite to 0.12 for 90-100% smectite gouge. This decrease is nonlinear – with high smectite gouges all exhibiting low residual friction ($\mu < 0.25$), and low smectite gouges all exhibiting high residual friction ($\mu > 0.5$); there is a rapid transition in friction between 30-70 wt% smectite. We note that the variations in friction are correlated with the abundance of smectite rather than total clay - as is evident from the behavior of the natural samples from Sumatra, which contain 8% and 19% smectite, but >50% clay, and exhibit friction similar to that for our synthetic mixtures with <30% smectite. We note minor exceptions to this trend wherein friction is slightly lower for our 90% smectite than our 100% smectite gouge, and we attribute this to the higher RH of the former experiment. Likewise, we note that for samples with lower smectite there is a similar minor

variation between some natural samples and the synthetics, which we attribute to the multi-modal composition of the natural sediments.

There is a similar difference in stress-strain evolution as a function of composition. Smectite-rich samples (≥ 50 wt%) exhibit a peak friction and subsequent decay at shear strains of $\sim 1-2$, whereas smectite-poor samples exhibit a roll over in friction after initial loading, and simply approach a steady state value (Figure 4-3A) (Logan and Rauenzahn, 1987; Saffer and Marone, 2003; Ikari et al., 2009; Knuth et al., 2013; Haines et al., 2013). The natural samples – with high clay contents ($\sim 50\%$ smectite + illite) – behave more similarly to the low clay synthetic gouges. This suggests that smectite may be the key factor in controlling frictional behavior, rather than total clay abundance.

4.4.2 Ultrasonic Velocities and Elastic Moduli

In general, the elastic responses of our samples fall into three main groups, which correspond to clay content: smectite-poor synthetic gouges (≤ 50 wt% smectite), smectite-rich synthetic gouges (> 70 wt% smectite), and the Sumatra samples (~ 50 wt% smectite + illite; with < 20 wt% smectite) (Figures 4-4, 4-5, and 4-6).

The smectite-poor synthetic gouge samples exhibit similar V_p , V_s , K , and G trends and values (figures 4-4, 4-5, and 4-6). These gouges are characterized by similar initial (pre-shear) values of V_p (~ 2300 – 2500 m/s), V_s ($V_s \sim 1200$ – 1300 m/s), K (~ 5 – 8 GPa), and G (~ 2.5 GPa – 3 GPa). Up to a shear strain of ~ 1.6 , all exhibit increasing velocity and elastic moduli. This increase is followed by a relatively rapid decrease in V_p and K , while V_s and G stabilize. The 50% smectite sample is an exception to this trend, and exhibits a decrease in V_s and G over these shear strains. Beyond shear strains of ~ 6 , V_p , V_s , G , and K all increase throughout the rest of the experiments (at a shear strain of 20, $V_p \sim 2900$ m/s – 3400 m/s, $V_s \sim 1500$ m/s – 1800 m/s, $K \sim$

10 GPa – 17 GPa, and $G \sim 5 \text{ GPa} - 6 \text{ GPa}$) with the 50% smectite gouge having the largest values of V_p and K , and 10% smectite having the largest values of V_s and G .

The smectite-rich synthetic gouges also all exhibit similar trends in elastic moduli and velocities, but span a larger range of values than the smectite-poor gouges (Figures 4-4 and 4-5). The 70% smectite sample exhibits higher velocities and larger elastic moduli than the 90% and 100% smectite gouges; however, in general, the smectite-rich samples (70 – 100 wt%) have much lower initial values of V_p (1300-1800 m/s, V_s (900-1100 m/s), K (1-4 GPa), and G (1-2 GPa) than the quartz-rich (smectite-poor) gouges. The smectite-poor synthetic gouges, like their smectite-rich counterparts, exhibit an initial increase in V_p , V_s , K , and G and peak at a shear strain of ~ 1.6 (Figures 4-4 and 4-5). Unlike the smectite-poor samples, which exhibit increasing velocities and moduli beyond shear strains of ~ 6 , the smectite-rich gouges exhibit decreasing velocities and moduli with continued shear (Figures 4-4 and 4-5). However, the 90% sample only displays an increase and peak in V_p and K while V_s and G remain stable ($V_p \sim 1700 \text{ m/s} - 2200 \text{ m/s}$, $V_s \sim 1000 \text{ m/s} - 1100 \text{ m/s}$, $K \sim 4 \text{ GPa} - 6 \text{ GPa}$, $G \sim 2 \text{ GPa} - 3 \text{ GPa}$). The 90% smectite sample – as is the case for frictional behavior – represents a minor exception to this overall trend primarily for V_s and G , as it exhibits values that are lower than the 100% smectite case. Again, this is consistent with the higher relative humidity for the 90% smectite experiment as increased water content decreases the frictional strength of smectite (Ikari et al., 2007).

The natural sediment samples from Sumatra exhibit intermediate properties, and more complex stress-strain behavior than the synthetic gouges. The two Sumatra samples exhibit initial values of V_p (~ 1600 - 1900 m/s) and K (~ 1 - 2 GPa) similar to the smectite-rich synthetic gouges (Figures 4-4 and 4-5); however, the pre-shear values of V_s ($\sim 1200 \text{ m/s}$) and G (~ 2 - 3 GPa) are more similar to those of the smectite-poor synthetic gouges (Figures 4-4 and 4-5). The behavior of the Sumatra samples at higher shear strains is slightly more complex. As shear progresses, V_p and K for both Sumatra samples increase and follow the same general trend as our smectite-poor

synthetic gouges, reaching maxima of $V_p \approx 2200\text{-}3300$ m/s and $K \approx 6\text{-}12$ GPa at a shear strain of 20. The two Sumatra samples have differing trends for V_s and G . The Sumatra sample with 8% smectite exhibits similar values and trends of V_s and G to the 10% smectite gouge ($V_s \approx 1800$ m/s and $G \approx 6$ GPa at shear strain of 20). However, the Sumatra sample with 19% smectite exhibits similar V_s and G to the 10% smectite sample until a shear strain of ~ 8 , after which it decreases to V_s and G values similar to the smectite-rich synthetic gouges ($V_s \approx 1100$ m/s and $G \approx 2$ GPa at a shear strain of 20). Overall, the natural sample with 19 wt% smectite (51% smectite + illite) exhibits lower V_p , V_s , K , and G , than the sample with 8 wt% (49% smectite + illite).

4.5 Discussion

Our experiments indicate that composition, shear fabric development, and porosity loss act in concert to control the mechanical and elastic properties of fault gouge. Importantly, we find that smectite content is the main factor in determining whether shear fabric or compaction plays the dominant role in controlling the evolution of friction and elastic properties with shear. Shear fabrics reduce the coefficient of friction in smectite-rich synthetic gouges, resulting in a decay from peak friction and overall low residual friction (Schleicher et al., 2006; Colletini et al., 2009; Haines et al., 2009, 2013; Niemeijer et al., 2010; Wojatschke et al., 2016). As described in the following, we suggest that shear fabrics also provide an explanation for the evolution of elastic moduli and wavespeeds, through a competition with porosity reduction.

4.5.1 Friction Strength and Stress-strain Behavior

In agreement with previous studies, we observe a peak and subsequent decay of the coefficient of friction in synthetic gouge samples with ≥ 50 wt% smectite (Figure 4-3) (Logan et

al., 1979; Saffer and Marone, 2003; Haines et al., 2009, 2013; Ikari et al., 2009, 2011; Niemeijer et al., 2010; Carpenter et al., 2011; Wojatschke et al., 2016). With decreased smectite and increased quartz content, this peak diminishes and is eventually absent in synthetic gouge samples that have < 50 wt% smectite. The characteristic peak and decay in the coefficient of friction of smectite-rich gouges has been linked to shear fabric formation, particularly the transition to throughgoing Y-shears with aligned clay minerals that weaken the layer (Wu et al., 1975; Haines et al., 2009; Niemeijer et al., 2010; Tembe et al., 2010; Carpenter et al., 2011; Ikari et al., 2011; Wojatschke et al., 2016).

The Sumatra samples have a more complicated composition and, therefore, a more complicated explanation for their frictional and stress-strain behavior. Though these samples both contain ~50 wt % smectite+illite (SI), these two samples are frictionally stronger than our 50% smectite synthetic gouge. The Sumatra samples contain a relatively small proportion of smectite (8 and 19 wt%; with the remaining SI composed of illite). This indicates that smectite, rather than total clay content, is probably the main control on strength and coefficient of friction. Though illite is a platy clay like smectite, due to the presence of poorly hydrated potassium ions in the interlayer of the illite structure, it is non-swelling and, therefore, experiences less weakening due to water. The Ca-montmorillonite smectite, on the other hand, is a swelling clay. The Ca ions in the interlayer of the smectite structure are highly hydrated and, therefore, more attracted to other particles and weaker due to the presence of water. If these samples had more smectite instead of illite, it is likely that they would behave as the other high smectite samples. However, we do see a decrease in the coefficient of friction at high shear strains indicating that, with enough shear, it may be possible for fabrics to form that affect the strength, and possibly the elastic response, of these materials.

4.5.2 Porosity Reduction, Fabric Evolution, and Elastic Properties

Compaction (porosity loss) is commonly cited as the primary control on velocity changes during deformation of granular materials (e.g., Gettemy et al., 2004), and shear (Hadley, 1976; Popp and Kern, 1998; Jia et al., 1999; Schubnel et al., 2003; Fortin et al., 2005, 2007; Khidas and Jia, 2012; Knuth et al., 2013; Kaproth and Marone, 2014). As porosity decreases, velocity is expected to increase as pore space is lost and grain contact quality increases. However, in our experiments, there are many instances where V_p decreases even as porosity decreases (Figures 4-7 and 4-8). This implies that processes other than porosity reduction play a role in controlling wave speed and its evolution with shear.

In general, we observe that both velocity and elastic moduli vary with gouge composition and shear strain. At a given shear strain, increased smectite content leads to a reduction in V_p , V_s , K , and G (Figure 4-6). The roles of smectite content and shearing become more evident at higher shear strains, as V_p , V_s , G , and K all increase with strain in clay-poor gouges, and decrease or remain steady in clay-rich gouges.

Figure 4-7 presents a compaction trend curve from an experiment (p5243) on 50% smectite 50% granular quartz synthetic gouge that was simply compacted to ~60 MPa (with no shear). V_p should follow a similar trend in our experiments if porosity reduction were the sole mechanism operating in the gouge. We hypothesize that the significant departures from this compaction trend in our experiments, including changes opposite in sign to the trend, reflect fabric development, dominantly in the clay-rich gouges. In particular, the observations of decreasing V_p even as compaction occurs (Figure 4-7), as well as the decrease (or steady values) of V_s , K , and G with shearing, are all consistent with a model in which shear planes parallel to the layer develop and mature. These features would disrupt and slow wave propagation normal to the layers, as is expected in anisotropic media and in the case of thin high aspect ratio cracks

(Eshelby, 1957, 1961, 1963; Budiansky and O'Connell, 1976; Hudson, 1986; Mavko et al., 2009).

The correlation of the peak in ultrasonic velocities and elastic moduli to the peak in friction further supports the idea that throughgoing fabrics are a likely underlying mechanism. In addition to the decrease in V_p with decreasing porosity, there are also stages of rapid velocity increase with shear, exceeding the rate of velocity we see in the simple example of pure compaction (no shear). Rapid V_p increases occur at high shear strains in the smectite-rich synthetic gouges as well as the Sumatra samples, and we interpret this to reflect a component of shear enhanced compaction (Zhu et al., 1997; Fortin et al., 2005; Fortin et al., 2007; Khidas & Jia, 2012).

On the basis of our data, we suggest that fabric development affects the elastic properties and frictional evolution of the gouges differently, depending on the smectite content (Figure 4-8). For smectite-rich gouges, the development of shear planes and alignment of clay minerals leads to: (1) the peak and subsequent decay in friction, as has been documented by detailed studies of microstructure and friction (e.g., Haines et al, 2009, 2013); (2) overall low frictional strength as pervasive Y-shears are established; and (3) disruption and slowing of wavespeeds across the layer, and concomitant decreased elastic moduli with shearing.

In smectite-poor gouges, we suggest that wavespeed and elastic moduli are controlled by a competition between fabric development and compaction. For gouges with <50 wt% smectite, and including the Sumatra samples, we do not observe a peak and decay in friction with strain (Figure 4-3), indicating that if shear fabrics or localized shear planes are developed, they do not exert significant control on the evolution of shear strength. However, the evolution of V_p , V_s , and elastic moduli is more complicated (Figures 4-4 and 4-5). Like the smectite-rich gouges, these materials exhibit a peak in wavespeeds at shear strains of ~ 2 followed by a reduction in these quantities up to a shear strain of ~ 6 , beyond which V_p , V_s , and elastic moduli all increase. As shear initiates, Riedel and P-shears form first and are not pervasive enough nor are they oriented in a way that they would interfere with wave propagation (Fortin et al., 2007; Khidas and Jia,

2012; Knuth et al., 2013; Haines et al., 2013; Kaproth and Marone, 2014). As shear progresses, Y-shears form and Riedel shears begin to rotate sub-parallel to the direction of shear and perpendicular to the direction of wave propagation (Logan and Rauenzahn, 1987; Logan et al., 1992; Haines et al., 2013). We posit that: (1) the initial increase and peak in velocities and elastic moduli is related to increasing load and grain re-organization that leads to enhanced grain contacts; and (2) the intermediate decrease in V_p , V_s , G , and K results from the formation of (perhaps poorly developed) Y-shears parallel to the direction of shear and perpendicular to the direction of wave propagation (Logan and Rauenzahn, 1987; Logan et al., 1992; Haines et al., 2013; Kenigsberg et al., 2019, submitted). At higher shear strains, we suggest that shear enhanced compaction dominates, and causes large increases in velocities and moduli.

The behavior of the Sumatra samples differs slightly from that of the smectite-poor synthetic gouges. These sediments are close to the threshold of ~50 wt% smectite that separates frictional and wavespeed evolution with strain for our synthetic samples, but as noted above, contain <20 wt% smectite. Therefore, it is not surprising that the two Sumatra samples exhibit similar stress strain behavior to our 10 wt% smectite gouge, without a peak and decay in friction (c.f. Figure 4-3). At high shear strains (~20 – 30) the coefficient of friction appears to decrease slightly. As these samples do contain ~50 wt% clays, this modest late stage weakening could be due to fabric formation associated with the complex mineralogy of the material, intragranular cracking, or destruction of long force chains. Overall, the velocities and elastic moduli for both Sumatra samples, like those for smectite-poor synthetic gouges, appear to be controlled by porosity loss, as V_p and K increase at all shear strains. However, for the Sumatra sample with 51% SI (19% smectite), V_s and G decrease at high shear strains (~10 – 30), again perhaps indicating that fabrics may be forming in this sample at high strains - and that V_s and G are more sensitive to fabric formation than V_p and K .

4.5.3 Shear Planes and Clays in Natural Fault Gouges

Although our natural fault gouges have much more complex compositions than two-component, synthetic clay-rich gouges, our data suggest that the coefficient of friction, elastic moduli, and wavespeeds for these materials are all highly consistent with data for synthetic gouges with comparable smectite content. With some variations and complexities as is expected with natural samples with a large range of minerals, the properties of our Sumatra samples lie within the range observed for the synthetic smectite-poor gouges. The importance of smectite, rather than total clay abundance, is consistent with previous studies that have investigated the role of dehydration and clay transformation in the onset of mechanical changes on major faults (Lauer et al., 2017; Hüpers et al., 2017) and the role of smectite and associated fabrics in leading to fault weakening (Ikari et al., 2009, 2015; Carpenter et al., 2011; Haines et al., 2013).

4.6 Conclusions

We performed direct shearing experiments on a range of smectite-quartz synthetic gouges and natural sediments that form protolith for the Sumatra subduction thrust, in order to gain insight into the roles of composition, porosity, and fabric evolution in controlling fault physical properties. Although porosity reduction is commonly recognized as a dominant control on the elastic properties of sediments and other granular materials (e.g., Bachrach et al., 2000; Dvorkin et al., 1999; Kaproth & Marone, 2014; Knuth et al., 2013; Mavko et al., 2009; Mavko & Nur, 1979; Nur et al., 1998), we found that, depending on smectite content, fabric and shear plane development also play a key role in the evolution of these properties with shearing. The frictional and elastic behavior of smectite-rich synthetic gouges is dominantly controlled by fabric development, particularly at high strains, whereas these properties in smectite-poor gouges evolve

in response to the competing effects of fabric development and porosity loss, including shear-enhanced compaction. Natural samples from Sumatra are controlled by similar micromechanical processes; in these materials, the low abundance of smectite and higher amounts of illite clays lead to behavior that mimics that of low-smectite synthetic gouges, but with possible indications that shear fabrics become increasingly important at high strains.

The interplay between gouge composition, fabric, and shear enhanced compaction elucidate the importance of these factors in governing the elastic and mechanical properties of faults. While the effects of clays and shear fabrics within fault zones on frictional properties have been thoroughly studied (Collettini et al., 2009; Haines et al., 2013; Kaproth & Marone, 2014; Knuth et al., 2013; Logan et al., 1979; Logan & Rauenzahn, 1987; Niemeijer et al., 2010; Tembe et al., 2010; Wojatschke et al., 2016), the effects of shear fabrics and clay composition on elastic properties have been less studied (e.g., Fortin et al., 2005; Fortin et al., 2007; Hadley, 1976; Jia et al., 1999; Kaproth & Marone, 2014; Khidas & Jia, 2012; Knuth et al., 2013; Nur et al., 1998; Popp & Kern, 1998; Schubnel et al., 2003).

In summary, we find that with increased smectite content within fault gouge, shear fabric formation controls elastic and mechanical properties causing the layer to destiffen, overpowering the effects of increased shear and decreased porosity. In contrast, low smectite content fault gouges are largely controlled by compaction, though these gouges are still affected by inferred fabric development. This hypothesized fabric formation which causes mechanical and frictional weakening also causes reduced elastic moduli indicating that smectite rich fault zones may be expected to be both frictionally weak and compliant relative to fault zones formed in stronger minerals.

Acknowledgements: We thank S. Swavely for technical help in the laboratory and Parisa Shokouhi and Charles Ammon for key discussions. We gratefully acknowledge support

from the NSF U.S. Science Support Program (Post expedition award), GDL Foundation, DOE geothermal program (DOE EERE DE-EE0006762) and the NSF Geophysics program (NSF awards EAR-1215856, EAR-1520760, and EAR-1547286/1547441. All data available from authors upon request.

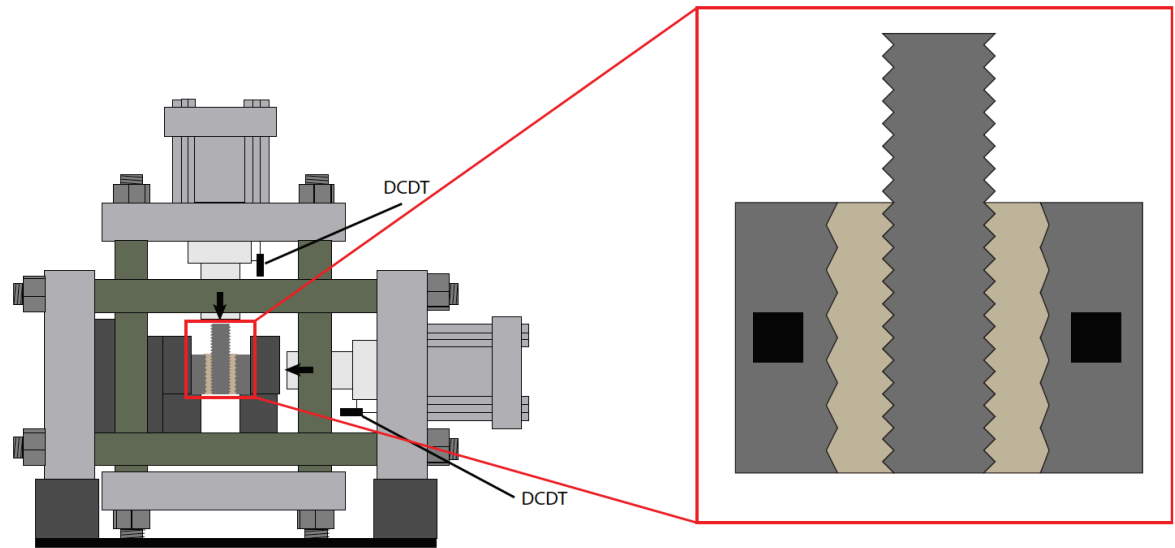


Figure 4-1: Left: Schematic of the biaxial shear apparatus and double direct shear sample. Right: Schematic of the double direct shear configuration with piezoelectric transducers within the side blocks (black rectangles).

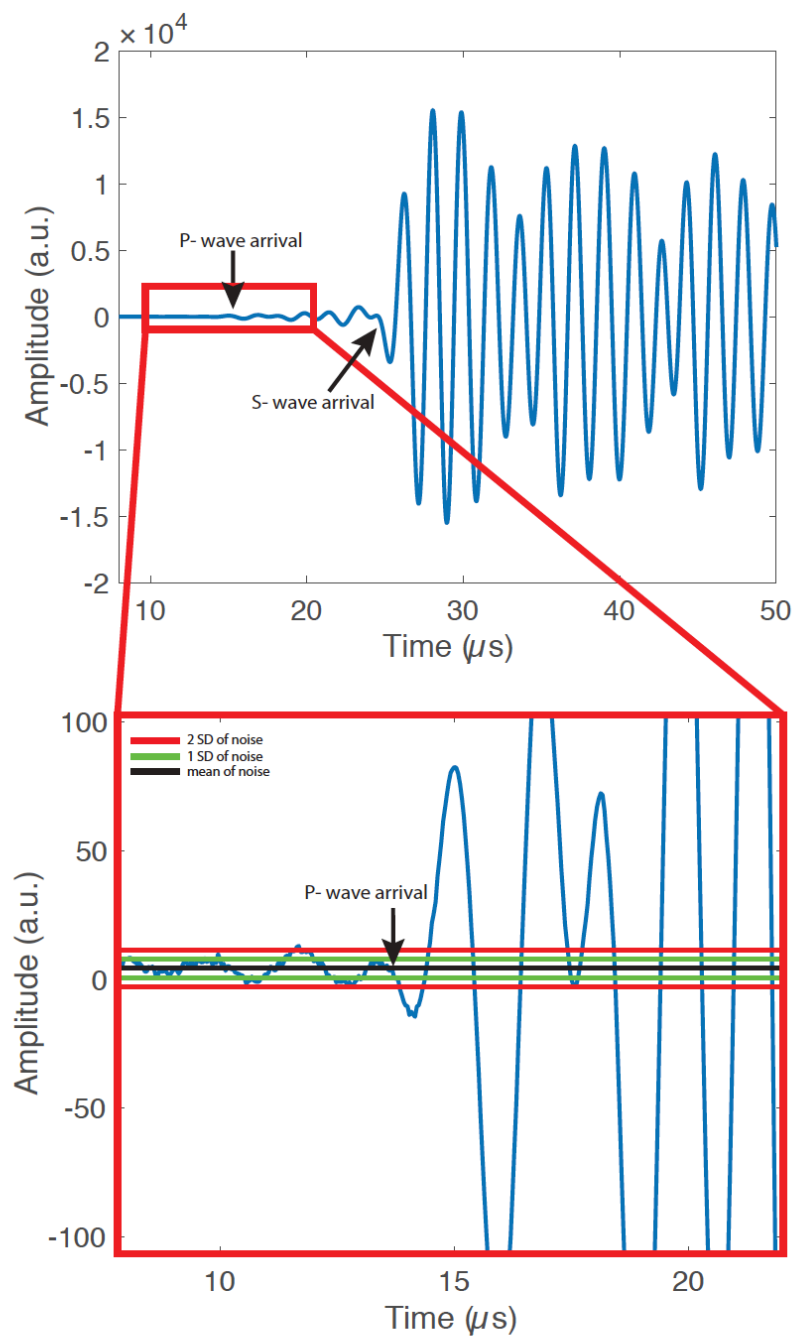


Figure 4-2: Example waveform in a.u., arbitrary units (p4830 - 50% smectite/50% quartz). P- and S-wave arrivals are picked at the zero crossing (black line) right before the signal has exceeded 2 standard deviation of the noise (red line).

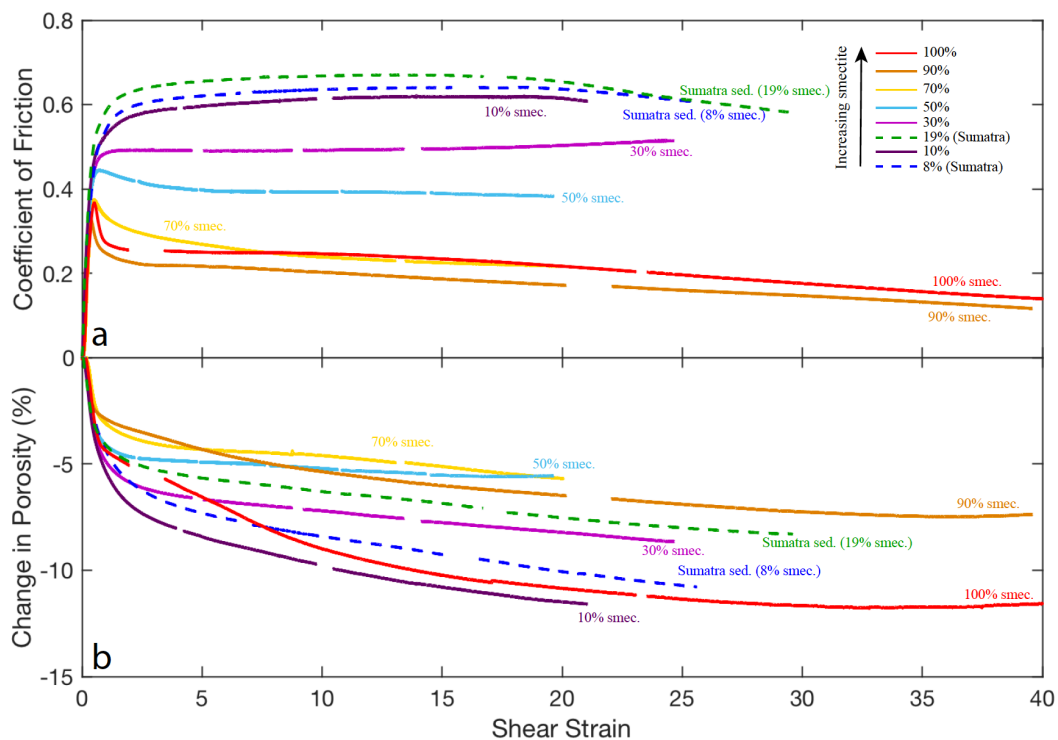


Figure 4-3: The coefficient of friction and change in porosity as a function of shear strain. The coefficient of friction decreases with increasing clay content in synthetic gouge mixtures. High smectite mixtures (50% and greater) exhibit a distinctive peak and subsequent decay due to fabric formation. Porosity decreases throughout the entire experiment for all mixtures. Porosity decreases most rapidly before peak friction and fabric formation and then reaches as steady state decrease as fabrics are formed. 100% and 90% smectite exhibit a more rapid decrease in porosity than other mixtures at intermediate shear strains (~0-8).

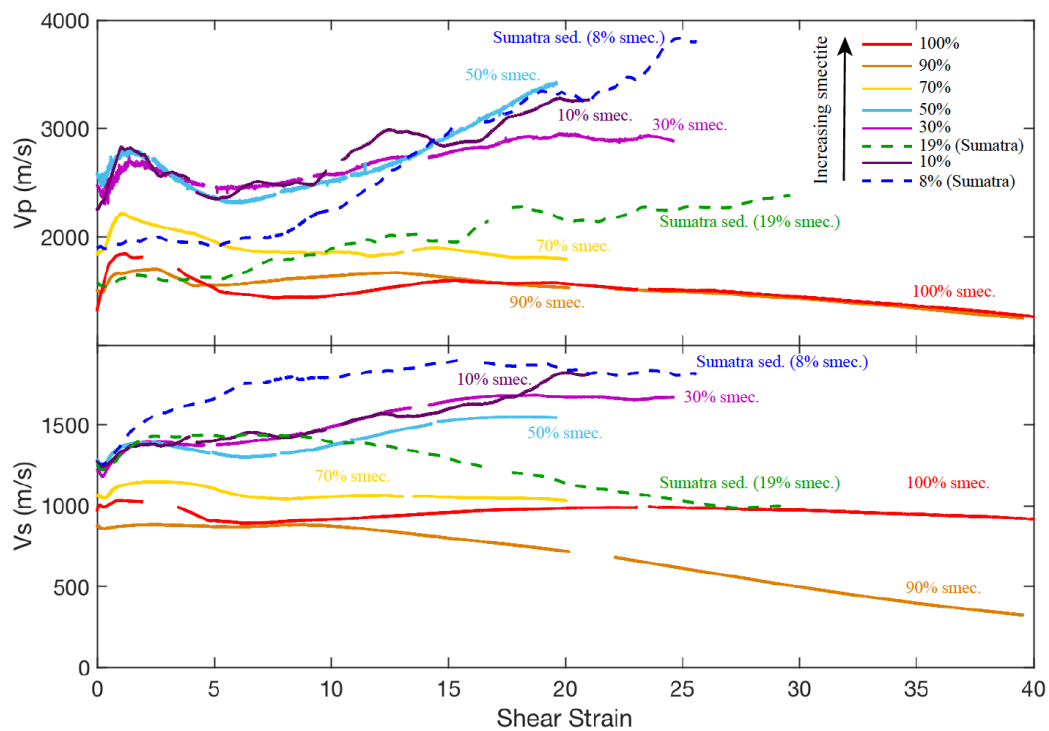


Figure 4-4: Absolute P- and S-wave velocities as a function of shear strain. In general, velocities decrease with increasing clay content. Decreases in velocities with increasing shear strain indicate that fabrics are controlling velocities as opposed to porosity loss. Due to the high portion of illite, the Sumatra sediments behave differently than the synthetic gouge mixtures.

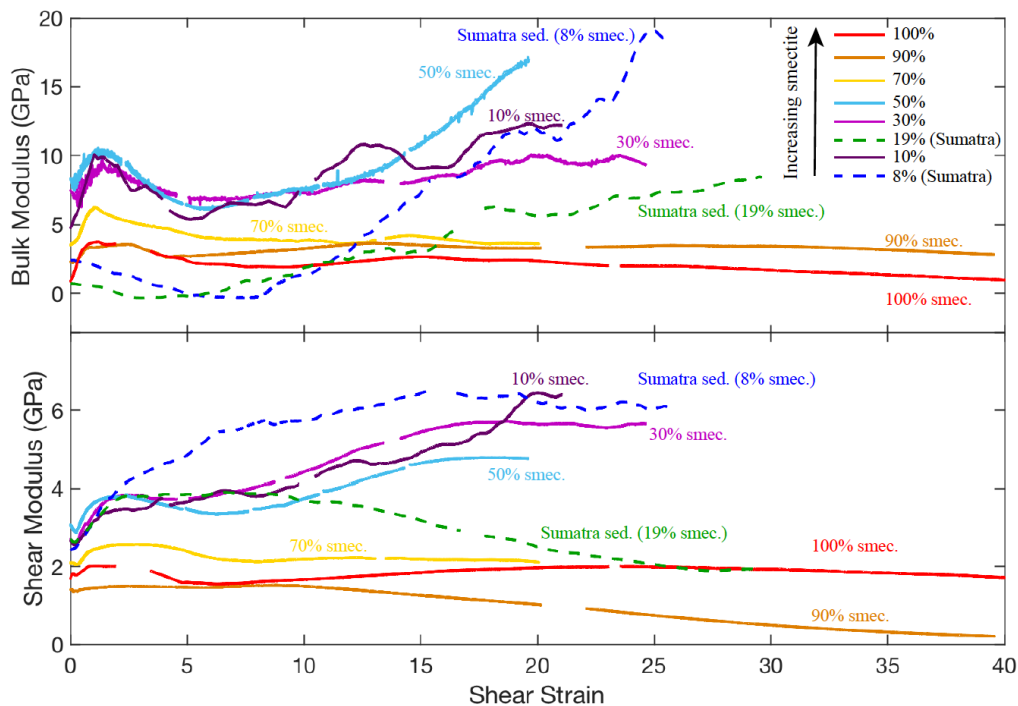


Figure 4-5: Shear and bulk moduli as a function of shear strain. High smectite synthetic gouge mixtures primarily exhibit decreasing elastic moduli as fabrics are weakening the gouges. Low smectite synthetic gouges have short periods of decrease due to optimally oriented fabrics, but are primarily controlled by porosity loss and shear enhanced compaction as is shown by the increasing elastic moduli. The Sumatra sediments exhibit increases in elastic moduli except for the shear modulus of one of the samples indicating that fabrics may be pervasive as high shear strains for this sample.

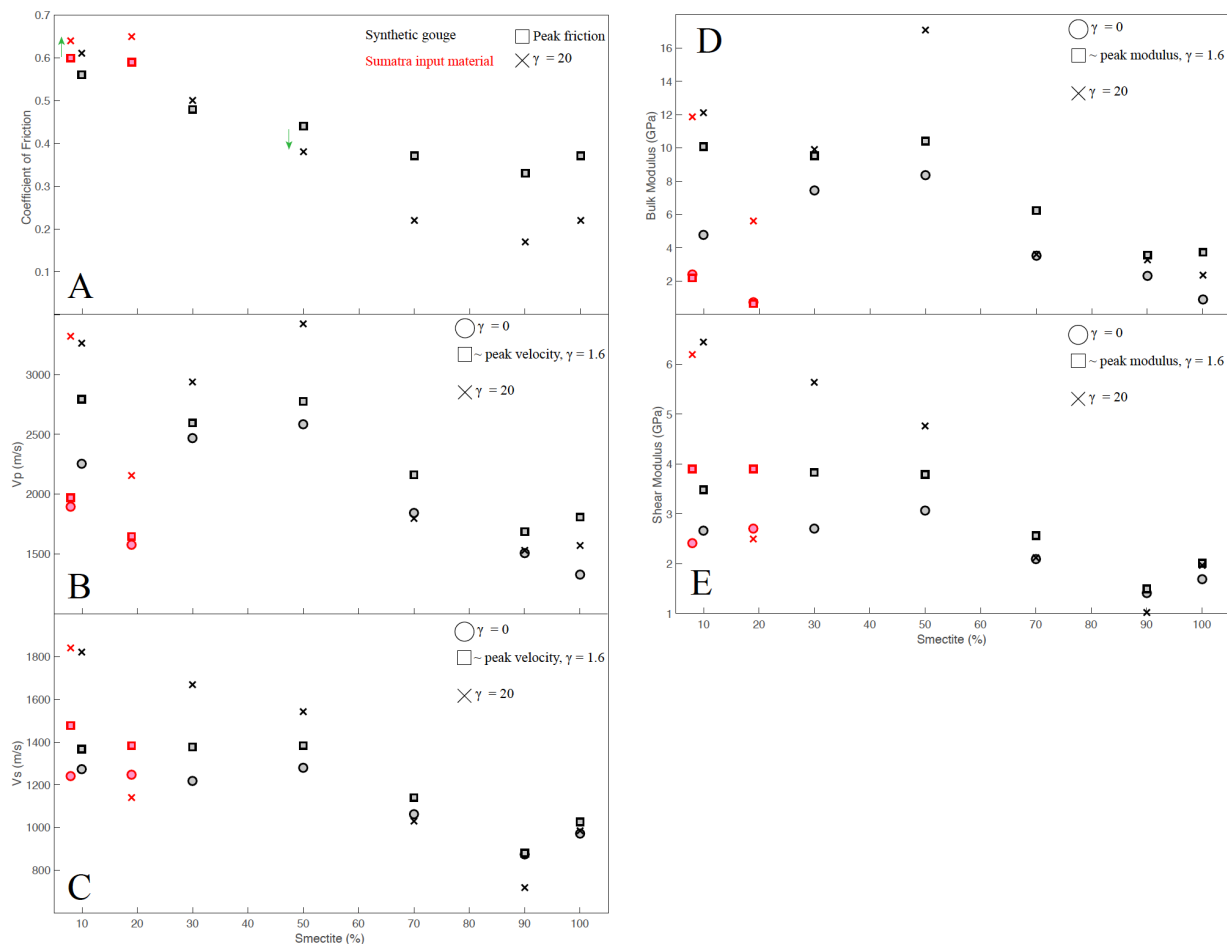


Figure 4-6: The coefficient of friction, V_p , V_s , and bulk (K) and shear (G) modulus as a function of smectite percentages at a shear strain of 0, local peak coefficient of friction (immediately after shear stress load up) and velocity/modulus, and at a shear strain of 20. Low smectite gouge mixtures exhibit an increase in the coefficient of friction (green arrow indicates increasing shear strain), V_p , V_s , K and G as a function of shear strain whereas high smectite synthetic gouge mixtures exhibit a decrease in V_p , V_s , and the coefficient of friction (green arrow indicates increasing shear strain) as a function of shear strain due to fabrics weakening the gouge. K and G reach a peak and then decrease by a shear strain of 20. The Sumatra samples largely behave similarly to the low smectite synthetic gouge samples with the exception of V_s and G of the Sumatra sample with 19% smectite.

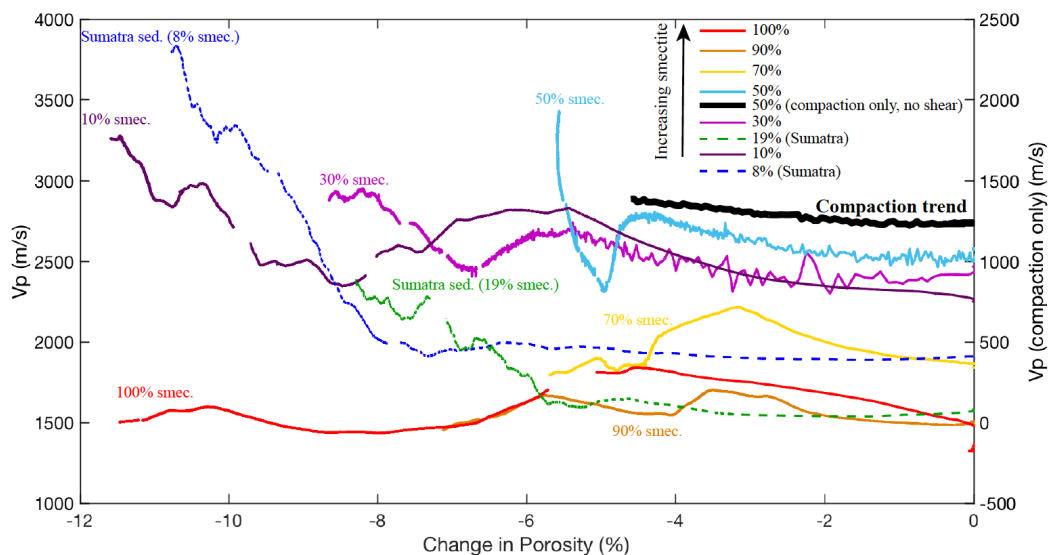


Figure 4-7: P-wave velocity as a function of change in porosity. Shear strain is increasing as porosity is reducing. Changes in ultrasonic velocity throughout shear are generally attributed to porosity loss and compaction. The thick black line shows the compaction trend for an experiment (p5243) that was only compacted and was not sheared. However, we observe a deviation from this trend for our sheared experiments with decreases in velocity even as porosity decreases indicating that another processes in controlling velocity. We interpret decreases in velocity as porosity decreases as periods in which fabrics are controlling the velocity. High smectite synthetic gouges largely exhibit decreasing velocities as porosity decreases, indicating that fabrics are controlling these gouges for the majority of shear. Low smectite synthetic gouges exhibit short term decreases in velocity. We attribute these decreases to periods in which fabrics are preferentially oriented perpendicular to the direction of wave propagation and, therefore, behave as barriers to the ultrasonic waves. The Sumatra sediments increase throughout shear indicating that they are largely controlled by porosity loss.

Table 4-1: List of Experiments

Exp. #	Composition	Peak coefficient of friction	Initial thickness of single layer (mm)	Calculated grain density of multi-phase mixture (g/cm ³)	Notes
p5212	100% smectite	0.42	8	2.1	Calibration of acoustic side blocks
p5213	100% smectite	0.33	8	2.1	Calibration of acoustic side blocks
p5214	100% smectite	0.35	3	2.1	Calibration of acoustic side blocks
p5215	100% smectite	0.38	3	2.1	Calibration of acoustic side blocks
p5216	100% smectite	0.37	5	2.1	Periodic mass loss measured
p5217	100% smectite	0.37	5	2.1	Periodic mass loss measured
p5145	90% smectite/ 10% quartz	0.37	3	2.155	Calibration of acoustic side blocks
p5148	90% smectite/ 10% quartz	0.33	8	2.155	Calibration of acoustic side blocks
p5149	90% smectite/ 10% quartz	0.33	5	2.155	Periodic mass loss measured
p5150	90% smectite/ 10% quartz	0.34	8	2.155	Calibration of acoustic side blocks
p5154	90% smectite/ 10% quartz	0.36	3	2.155	Calibration of acoustic side blocks
p5157	90% smectite/ 10% quartz	0.34	5	2.155	Periodic mass loss measured

p5039	70% smectite/ 30% quartz	0.43	3	2.265	Calibration of acoustic side blocks
p5040	70% smectite/ 30% quartz	0.41	3	2.265	Calibration of acoustic side blocks
p5043	70% smectite/ 30% quartz	0.37	8	2.265	Calibration of acoustic side blocks
p5052	70% smectite/ 30% quartz	0.41	5	2.265	Periodic mass loss measured
p5128	70% smectite/ 30% quartz	0.36	8	2.265	Calibration of acoustic side blocks
p5136	70% smectite/ 30% quartz	0.37	5	2.265	Periodic mass loss measured
p4808	50% smectite/ 50% quartz	0.49	5	2.375	Periodic mass loss measured
p4830	50% smectite/ 50% quartz	0.47	5	2.375	Periodic mass loss measured
p4853	50% smectite/ 50% quartz	N/A	23	2.375	No shear. Calibration of acoustic side blocks.
p4867	50% smectite/ 50% quartz	0.47	3	2.375	Calibration of acoustic side blocks.
p4912	50% smectite/ 50% quartz	0.44	5	2.375	Periodic mass loss measured
p4913	50% smectite/ 50% quartz	0.43	5	2.375	Periodic mass loss measured
p4947	50% smectite/ 50% quartz	0.41	8	2.375	Calibration of acoustic side blocks
p4962	50% smectite/ 50% quartz	0.41	8	2.375	Calibration of acoustic side blocks
p4977	50% smectite/ 50% quartz	0.44	7	2.375	Calibration of acoustic side blocks

p5129	30% smectite/ 70% quartz	0.46 (before rollover)	8	2.485	Calibration of acoustic side blocks
p5137	30% smectite/ 70% quartz	0.5 (before rollover)	5	2.485	Periodic mass loss measured
p5141	30% smectite/ 70% quartz	0.46 (before rollover)	8	2.485	Calibration of acoustic side blocks
p5142	30% smectite/ 70% quartz	0.5 (before rollover)	3	2.485	Calibration of acoustic side blocks
p5143	30% smectite/ 70% quartz	0.51 (before rollover)	3	2.485	Calibration of acoustic side blocks
p5144	30% smectite/ 70% quartz	0.48 (before rollover)	5	2.485	Periodic mass loss measured
p5167	10% smectite/ 90% quartz	0.54 (before rollover)	8	2.595	Calibration of acoustic side blocks
p5176	10% smectite/ 90% quartz	0.56 (before rollover)	5	2.595	Periodic mass loss measured
p5178	10% smectite/ 90% quartz	0.57 (before rollover)	5	2.595	Periodic mass loss measured
p5184	10% smectite/ 90% quartz	.054 (before rollover)	8	2.595	Calibration of acoustic side blocks
p5185	10% smectite/ 90% quartz	0.57 (before rollover)	3	2.595	Calibration of acoustic side blocks
p5189	10% smectite/ 90% quartz	0.55 (before rollover)	3	2.595	Calibration of acoustic side blocks
p5218	Sumatra input material (51% smectite + illite)	0.6 (before rollover)	5	2.586	Periodic mass loss measured
p5219	Sumatra input material (51% smectite + illite)	0.63 (before rollover)	3	2.586	Calibration of acoustic side blocks
p5223	Sumatra input material (51% smectite + illite)	0.57 (before rollover)	8	2.586	Calibration of acoustic side blocks

p5224	Sumatra input material (51% smectite + illite)	0.59 (before rollover)	3	2.586	Calibration of acoustic side blocks
p5225	Sumatra input material (51% smectite + illite)	0.64 (before rollover)	5	2.586	Periodic mass loss measured
p5226	Sumatra input material (51% smectite + illite)	0.58 (before rollover)	8	2.586	Calibration of acoustic side blocks
p5196	Sumatra input material (49% smectite + illite)	0.55 (before rollover)	5	2.652	Periodic mass loss measured
p5197	Sumatra input material (49% smectite + illite)	0.58 (before rollover)	3	2.652	Calibration of acoustic side blocks
p5199	Sumatra input material (49% smectite + illite)	0.57 (before rollover)	8	2.652	Calibration of acoustic side blocks
p5203	Sumatra input material (49% smectite + illite)	0.64 (before rollover)	3	2.652	Calibration of acoustic side blocks
p5204	Sumatra input material (49% smectite + illite)	0.6 (before rollover)	5	2.652	Periodic mass loss measured

Chapter 5

Evolution of Permeability During Shear of Fault Gouge: Effects of Composition and Fabric

Abby R. Kenigsberg¹, Clay E. Wood¹, Jacques Rivière², Chris Marone¹, Demian M. Saffer¹

¹Department of Geosciences and Center for Geomechanics, Geofluids, & Geohazards, The Pennsylvania State University, University Park, Pennsylvania 16802, USA

²Department of Engineering Science and Mechanics, The Pennsylvania State University, University Park, Pennsylvania 16802, USA

5.1 Abstract

Smectite clay has been shown to drastically reduce fault zone permeability which can have a variety of effects on a fault zone including causing increased pore pressures and allowing the fault zone to serve as a reservoir cap. Though past studies have reported decreased permeability when smectite gouge is sheared, few, if any, have attempted to directly correlate this decrease to shear fabrics. Furthermore, no previous studies have linked permeability reduction, shear fabrics, coefficient of friction, and elastic properties. In this study, we report on a suite of double direct shear experiments in a true triaxial pressure vessel. We studied a suite of synthetic gouges ranging from 10 - 90% Ca-montmorillonite smectite clay mixed with granular quartz. We also recorded ultrasonic waveform data throughout shear. We applied normal stresses, shear stress, and confining pressures during permeability tests where the pore pressure differential was 3 MPa. We measured and calculated permeability, coefficient of friction, and elastic properties.

We found that initial permeability values range from $3.9 * 10^{-20}$ to $8.5 * 10^{-17}$ and final permeability values at steady state friction range from $2.0 * 10^{-21}$ to $5.9 * 10^{-18}$. For all mixtures, permeability decreases significantly directly after a peak in the coefficient of friction indicating that shear fabrics are directly responsible for the decrease in permeability. The amplitude values track the coefficient of friction and show similar trends displaying that ultrasonic properties can be used as another proxy for fabric formation. This has important implications for faults in natural settings as we have determined that not only does the amount of smectite within the fault gouge control the permeability, but the maturity and development of the shear fabrics are also a very important characteristic to consider when evaluating fault zone permeability.

5.2 Introduction

Permeability in clay-rich fault zones, and permeability evolution with shearing and deformation, are key controls on important hydrologic and mechanical processes. These include regional flow and pressure compartmentalization associated with fault sealing, as well as promotion of elevated pore pressures that affect fault strength and sliding stability (Hubbert and Rubey, 1959; Knipe, 1992; Rice, 1992; Yielding et al., 1997; Faulkner and Rutter, 2001; Wibberley and Shimamoto, 2005; Segall and Rice, 2006; Vrolijk et al., 2016). Transient processes related to fault slip events like shear compaction and dilation also play important roles in earthquake nucleation and propagation (Sleep and Blanpied, 1992; Samuelson et al., 2009).

Clay minerals are one cause of low fault zone permeability in a range of different settings, including the San Andreas fault, the Japan Trench, the Nankai Trough, and the Carboneras fault (Wu et al., 1975; Faulkner and Rutter, 2001; Faulkner et al., 2003, 2010; Crawford et al., 2008; Ikari and Saffer, 2012; Ujiie et al., 2013). While many studies have shown that clay-rich fault gouge, and smectite clays in particular, exhibit low permeability ($10^{-18} - 10^{-21}$

m²), particularly when sheared, the evolution of permeability with shear, and the links between permeability, shear strain, composition, and other physical properties (friction, stiffness) is not well understood (Morrow et al., 1984, 2017; Faulkner and Rutter, 2003; Crawford et al., 2008; Ikari et al., 2009; Behnsen and Faulkner, 2013; Kaproth et al., 2016). In this study, we investigate the direct links between shear fabric formation, permeability, and ultrasonic elastic properties in synthetic smectite-rich gouge via a combined suite of measurements during shear, including the coefficient of friction, permeability, layer thickness changes, and ultrasonic amplitudes.

Many studies have shown that fabrics formed during shear in clay-rich gouges leads to frictional weakening from a peak to considerably lower residual values with progressive shearing (Sisbon, 1977; Logan and Rauenzahn, 1987; Faulkner et al., 2003; Wibberley and Shimamoto, 2003; Saffer and Marone, 2003; Jefferies et al., 2006; Ikari et al., 2009, 2015; Niemeijer et al., 2010; Carpenter et al., 2011; Knuth et al., 2013; Haines et al., 2013; Wojatschke et al., 2016). In fact, the combined effects of abundant smectite and well developed fabrics have been directly linked to low coefficient of friction ($\mu = 0.1 - 0.3$) of major fault zones in a range of tectonic settings (Wu et al., 1975; Deng and Underwood, 2001; Collettini et al., 2009; Carpenter et al., 2011, 2012; Lockner et al., 2011; Ikari et al., 2011; Ujiie et al., 2013; Wojatschke et al., 2016). Though it is known that smectite and shear fabrics reduce frictional strength, less is known about the links between gouge composition, fabric, and permeability. Some recent studies have reported that permeability in phyllosilicate-rich gouges reduces largely before a shear strain of 5 and then reaches an equilibrium (Crawford et al., 2008; Ikari et al., 2009; Kaproth et al., 2016), though they do not discuss in depth that a shear strain of 5 correlates to the peak and then decay in friction when fabrics are initially forming, which is possibly a more significant target than a given shear strain.

In this study, we investigate permeability evolution during shearing and its dependence on gouge composition. To accomplish this, we tested a range of smectite-rich gouge

samples composed of 10 - 90% smectite mixed with granular quartz, and conducted a suite of direct shear experiments with concurrent measurement of permeability and ultrasonic wave transmission across the gouge. We then link changes in permeability, the coefficient of friction, and ultrasonic amplitudes in the context of inferred fabric evolution.

5.3 Materials and Methods

5.3.1 Friction Measurements and Permeability Tests

We sheared synthetic clay-rich fault gouges (ranging from 10 – 90 wt% Ca-montmorillonite smectite clay mixed with granular quartz) in a double-direct shear (DDS) configuration inside of a pressure vessel (Anthony and Marone, 2005; Knuth and Marone, 2007; Samuelson et al., 2009) (Figure 5-1). Grain size analyses from Knuth et al. 2013 determined that the Ca-montmorillonite smectite clay is polydisperse with individual grains forming clumps from 10 – 200 μm and peaks at $\sim 75 \mu\text{m}$ (Knuth et al., 2013) whereas the granular quartz is has a median grain size of $\sim 10.5 \mu\text{m}$ (Ikari et al., 2009).

The double-direct shear (DDS) configuration consists of two $\sim 5 \text{ mm}$ layers of gouge sandwiched between two grooved side blocks and a center block (Figure 5-1). The side block dimensions are 5 x 5 cm; the sample contact area is $\sim 30.78 \text{ cm}^2$ throughout the experiment (Ikari et al., 2009). All of the forcing blocks are plumbed to allow fluid access, and include porous stainless steel frits that allow fluid to be evenly distributed to the layer faces (Samuelson et al., 2009; Ikari et al., 2009). A piece of filter paper is placed between the frits and the gouge layer to prevent the frits from becoming clogged with gouge. The entire sample assembly is then sealed in a rubber jacket.

Effective normal stress (σ_n') is applied to the sample via a combination of confining

pressure (P_c), and a horizontal piston (σ_n) (Figure 5-1). The confining fluid used in our experiments is a food-grade heat transfer oil (XCEL THERM 600, Radco Industries). Shear stress is applied via a vertical piston that enters through the top of the vessel. All stresses are independently servo-controlled. Pore fluid (deionized water) is applied by intensifiers plumbed to the forcing blocks. These include an “upstream” pore pressure (PPa) applied through the center block and a “downstream” pore pressure applied to the two side blocks (PPb) (Figure 5-1). The vertical and horizontal stresses are measured with load cells with a resolution of ± 0.1 kPa (Kaproth and Marone, 2014), and vertical and horizontal displacement are measured continuously via direct current displacement transducers (DCDT) with an accuracy of ± 0.1 μm . P_c , PPa , and PPb are controlled to ± 7 kPa (Ikari et al., 2009). We calculate the coefficient of friction (μ) using the ratio of shear stress divided by normal stress, assuming that cohesion in the granular gouge is negligible.

After loading the assembly into the vessel and prior to shearing, we loaded the sample to ~ 16 MPa effective normal stress ($\sigma_n = 4$ MPa; $P_c = 3$ MPa) and saturated the gouge by applying a vacuum at the downstream end, and an upstream pressure (PPa) of 1 MPa. We then sheared the gouge layers at a constant effective normal stress of ~ 32 MPa, constant displacement rates of ~ 21.5 $\mu\text{m/s}$, a P_c of 12 MPa, and pore pressure ($PPa = PPb$) of 1 MPa.

Throughout each experiment, we periodically stopped shear to conduct permeability tests using a steady state constant head technique, with PPa set to 4 MPa PPb at 1 MPa. Using Darcy’s law, we calculated permeability (m^2) as follows,

$$\text{permeability}, k = \frac{Q * h * \eta}{A * dPp}$$

where dPp is the pore pressure differential (Pa), Q is the volumetric flow rate (m^3/s), A is the cross sectional area of the sample (0.005 m^2), h is the layer thickness (m), and η is the

dynamic viscosity of water (Pa s). We only calculated permeability after equilibration, determined by comparison of Q_a (flow rate for Ppa) and Q_b (flow rate for Ppb).

5.3.2 Ultrasonic Measurements

We continuously measured and recorded ultrasonic wave propagation throughout shear using piezoelectric (PZT) transducers. The system sends a pulse every 10 milliseconds and during processing we stack 100 waveforms to improve signal to noise ratio. The PZTs are bonded to the side blocks via epoxy. We used 1.27 cm diameter, P-wave PZTs with a center frequency of 500 kHz. One PZT transmits a waveform while the other receives it across the sample. Here, we focus on amplitudes because they provide a highly sensitive measure of small changes in gouge layer properties and fabric development (Kilgore et al., 2017; Shreedharan et al., 2019). In order to assess variations in amplitude during shear, we report amplitudes as the maximum positive value of the P-wave first arrival, normalized to the amplitude at zero shear strain (Figure 5-1).

5.4 Results

5.4.1 Friction and Permeability Evolution as a Function of Clay Content and Shear Strain

Coefficient of friction and permeability both decrease systematically with increased clay content and with progressive shear (Figures 5-2, 5-3a, 5-3b). All mixtures exhibit a local peak in coefficient of friction at a shear strain of ~4-5, and then decay to residual friction values (Figure 5-2). The local peak coefficient of friction after initial shear stress load up (often referred to simply as the peak coefficient of friction) ranges from $\mu=0.16$ for 90% smectite to $\mu=0.66$ for 10% smectite; residual coefficient of friction ranges from $\mu=0.14$ for 90% smectite to $\mu=0.51$ for

10% smectite (Figures 5-2 and 5-3). Both the residual and peak friction coefficients vary approximately linearly with smectite abundance, and are consistent with previously reported friction values for clay-rich natural and synthetic gouges (Figure 5-3a) (Logan and Rauenzahn, 1987; Saffer and Marone, 2003; Ikari et al., 2009; Haines et al., 2013).

Initial (pre-shear) permeability values range from $3.9 \times 10^{-20} \text{ m}^2$ for our 70 wt% smectite gouge to $8.5 \times 10^{-17} \text{ m}^2$ for 10 wt% smectite. Final (at shear strains >10 ; see Figure 5-2) permeability values range from $2.0 \times 10^{-21} \text{ m}^2$ for 70% smectite to $5.9 \times 10^{-18} \text{ m}^2$ for 10% smectite. The permeability for 10% smectite and 70% smectite decrease by ~ 1 order of magnitude whereas the permeability for 30% smectite and 50% smectite decrease by ~ 2 orders of magnitude. We did not collect permeability data for 90% smectite because the equilibration time was too large. For all mixtures, permeability decreases dramatically immediately after peak friction, between shear strains of ~ 2.5 -5, beyond which it continues to decrease gradually with further shearing (Figures 5-2 and 5-4). This is consistent with previous work on kaolinite-quartz mixtures, montmorillonite-quartz mixtures, chlorite schist, illite shale, halite-illite-quartz mixtures, and halite-montmorillonite-quartz mixtures showing that permeability decreases most markedly by a shear strain of 5 (Crawford et al., 2008; Ikari et al., 2009; Kaproth et al., 2016). One key result of our work is that once the gouge begins failing in shear following initial load-up (i.e. at and following attainment of peak friction), the combined effects of gouge composition and shearing (associated with presumed fabric development) lead to a systematic correlation between friction

and permeability – both for a given gouge as shear progresses, and in comparing gouges of different composition (Figure 5-4).

5.4.2 Ultrasonic Amplitudes

In general, ultrasonic amplitudes decrease both with clay content and progressive shearing (Figures 5-3 and 5-6). The mixtures with 10 - 50% smectite all reach a peak amplitude (ranging from 1.3 – 1.7, respectively) that approximately maps to the peak coefficient of friction, before decreasing with further shear strain (Figures 5-5 and 5-6). The mixtures with higher smectite abundance (70 and 90 wt%), which exhibit less pronounced peak friction (c.f. Figure 5-1) don't exhibit a peak amplitude, but are characterized by a clear decrease in amplitude that coincides with the approach to residual friction.

5.5 Discussion

5.5.1 Coevolution of Permeability, Friction, and Amplitude

Figure 5-3 shows the clear relationship between clay content and coefficient of friction as well as permeability indicating that greater proportions of smectite cause gouge to be much weaker and also less permeable. In addition, figure 5-3 highlights the strong correlation between evolution of the coefficient of friction (μ), permeability (k), and amplitude (A) as function of strain as increased shear strain results in further decreases in the coefficient of friction, permeability, and amplitude. The strong coevolution of these properties with shear is consistent with the idea that fabric is controlling friction and permeability reduction (Crawford et al., 2008; Ikari et al., 2009; Haines et al., 2013; Kaproth et al., 2016). Therefore, we interpret this decrease

in μ , k , and A with increasing shear strain as an indicator of fabric formation both weakening the gouge layer and also causing a barrier to flow as the fabrics form perpendicular to the direction of water flow during permeability tests. Furthermore, we have observed (Figure 5-4) that during initial shear load up, there is very little permeability reduction. During this time, we hypothesize that grains are simply rearranging and rotating and are not yet aligned. However, immediately after peak friction, when fabrics are becoming substantially more pervasive (Haines et al., 2013), permeability drops significantly and then generally stabilizes or decreases to a lesser extent (Figures 5-2 and 5-4). This indicates that as Riedel shears are rotating and Y-shears are forming perpendicular to the direction of flow, they are acting as flow barriers and causing a dramatic decrease in permeability (Haines et al., 2013; Kenigsberg et al., 2019b (submitted), 2019a (submitted)). However, once fabrics are formed and only continue to evolve (Haines et al., 2013), permeability is less affected and changes less dramatically. As seen in figure 5-4, before peak friction, all mixtures show similar trends with fairly stable permeability values. However, after peak friction, the more smectite present in the mixture, the more pronounced the decrease in permeability is, as is seen by the increased steepness of the slope of permeability decrease in figure 5-4. Mixtures with 10% and 30% smectite reach a steady state permeability as show by the last 3 permeability measurements in figures 5-2 and 5-4. However, mixtures with 50% and 70% smectite seem to continue to decrease even at high shear strains, likely because fabrics are much more pervasive and continue to form in these mixtures relative to the 10% and 30% smectite samples. As stated above 10% smectite and 70% smectite decrease by ~ 1 order of magnitude whereas the permeability for 30% smectite and 50% smectite decrease by ~ 2 orders of magnitude. It is possible that 30% smectite and 50% smectite mixtures have the highest potential for permeability reduction via fabric evolution. The 10% smectite mixture is largely controlled by the quartz within the gouge, whereas the 70% mixture starts with extremely low permeability and does not have the same potential for permeability reduction as the 30% smectite and 50%

smectite do. This relationship between the coefficient of friction and permeability provides further evidence that fabrics directly control permeability and the degree of shear, or maturity of a fault, is an extremely important factor in determining the amount of permeability that is possible.

We have found that the amplitude mimics the response of the coefficient of friction to shear, making amplitude an additional indicator for shear fabric formation. We largely examine this relationship in figure 5-5 by focusing on experiment p5309 which is composed of 30% smectite.

As shown in figure 5-5 and figure 5-6, during shear stress load up, the coefficient of friction increases while the amplitude is relatively stable (figure 5-5). As stated above, this is likely because grains are simply rearranging and no fabrics have formed in the layer, however, the layer is compacting and becoming more stiff which causes in the increase in the coefficient of friction (Knuth et al., 2013; Haines et al., 2013; Kenigsberg et al., 2019b (submitted), 2019a (submitted)). As the layer approaches peak friction (figure 5-5), amplitude begins to increase for the first time as the layer continues to stiffen. At peak friction, the shear fabrics form planes of weakness and have become pervasive enough to begin to control the coefficient of friction, however, amplitude is still largely controlled by the compaction of the layer and, therefore, continues to increase (layer thickness shown in figure 5-7). As the coefficient of friction continues to decrease due to fabrics evolving and becoming more pervasive (Haines et al., 2013; Kenigsberg et al., 2019b (submitted), 2019a (submitted)), amplitude also reaches a peak and, soon after, as steady state friction is achieved, amplitude begins to decrease. This decrease is likely due to evolving and pervasive shear fabrics that create a more complex geometry that reduces the efficiency of ultrasonic energy transmission, causing a decrease in the ultrasonic amplitudes as the coefficient of friction reaches a steady state as shown in Haines et al., 2013, Knuth et al., 2013, and our previous studies. Based on ours and others past work, it is suspected that this is the time that throughgoing Y-shears and boundary shears form, acting as barriers to

ultrasonic energy transmission and greatly weakening the gouge. This close relationship between friction, amplitudes, and fabrics allows us to use ultrasonic properties as another proxy for fabric formation and, therefore, permeability decrease.

5.5.2 Implications for Fault Hydraulic and Mechanical Processes

The combined effects of increasing strain, fabric evolution, and gouge composition play important roles in controlling permeability and, ultimately, fault properties. As strain, fabric, and composition change and evolve together, we find that weaker gouges – both from clay abundance and shear fabrics – also have low permeability and transmission efficiency for acoustic energy (i.e. lower amplitudes). Therefore, weaker faults may be more sensitive to fault zone processes and properties affected by low fault zone permeability such as pore pressure generation and trapping, dynamic fault weakening, and dilation hardening (Hubbert and Rubey, 1959; Rice, 1992; Faulkner and Rutter, 2001; Wibberley and Shimamoto, 2005; Segall and Rice, 2006). Often, only shale bed thickness or amount of clay within a fault is considered in seal capacity models (Knipe, 1992; Yielding et al., 1997; Vrolijk et al., 2016). However, we show that for both seal capacity and fault stability, fault maturity is a vital characteristic to consider as well.

5.6 Conclusions

We conducted shear and permeability tests on a range of synthetic, smectite-rich gouge samples and continuously recorded ultrasonic amplitudes. We found a direct correlation between fabric formation and permeability reduction and determined that directly after the local peak coefficient of friction is achieved due to fabric formation, the largest decrease in permeability occurs. In addition, we determined that ultrasonic amplitudes can be used to track fabric evolution

and, therefore, permeability reduction. This study has broad impacts as we have found that the maturity of a fault zone is extremely important to understanding the amount of permeability reduction possible. In addition, we have found that amplitude can be used to track the evolution of fabrics and, therefore, permeability. This is vital to remember when assessing faults for their potential to cause increased pore pressure and lower effective normal stresses. This study also has industry applications as we have shown that fault maturity is also an important characteristic of seal capacity of reservoirs.

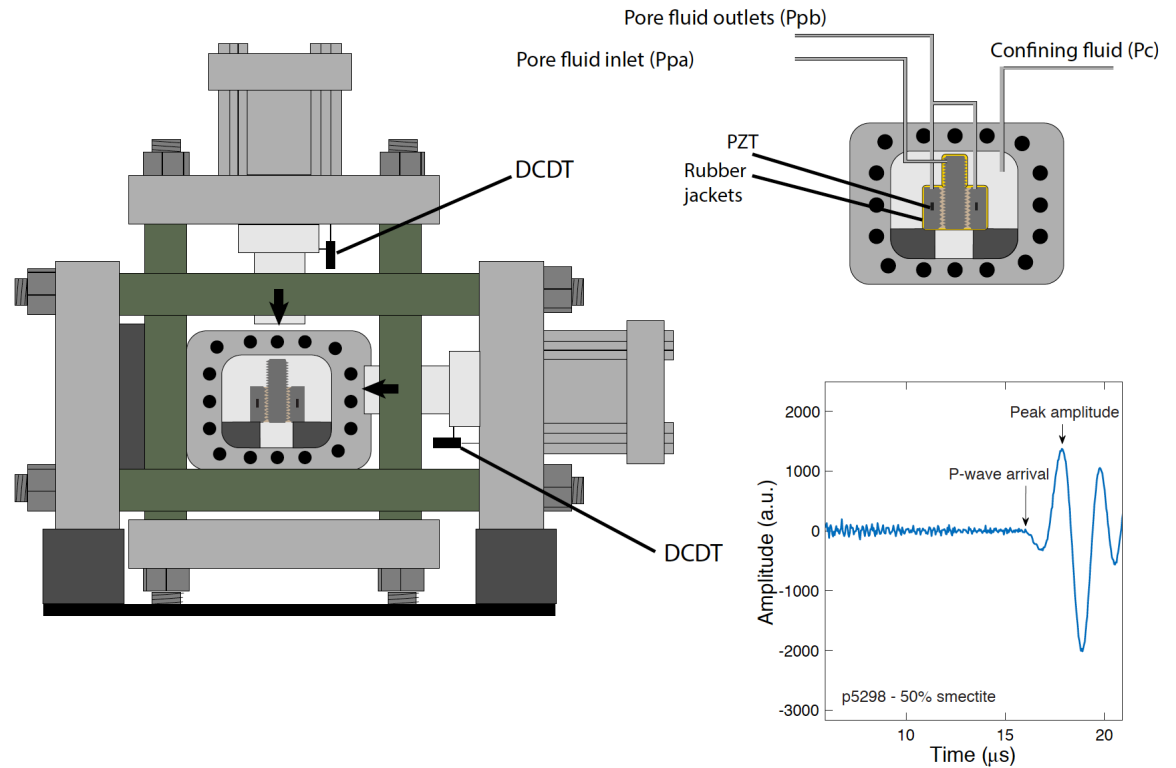


Figure 5-1: Left: Schematic of the biaxial shear apparatus and double direct shear sample inside of the true triaxial pressure vessel. Top Right: Schematic of the pressure vessel with pore fluid and confining pressure lines shown. Piezoelectric transducers are shown within the side blocks – black rectangles - and rubber jackets to seal the samples are shown around the sample in yellow. Bottom right: Example waveform in a.u., arbitrary units (p5298 - 50% smectite/50% quartz). The amplitude is picked as the first peak amplitude after the P-wave arrival.

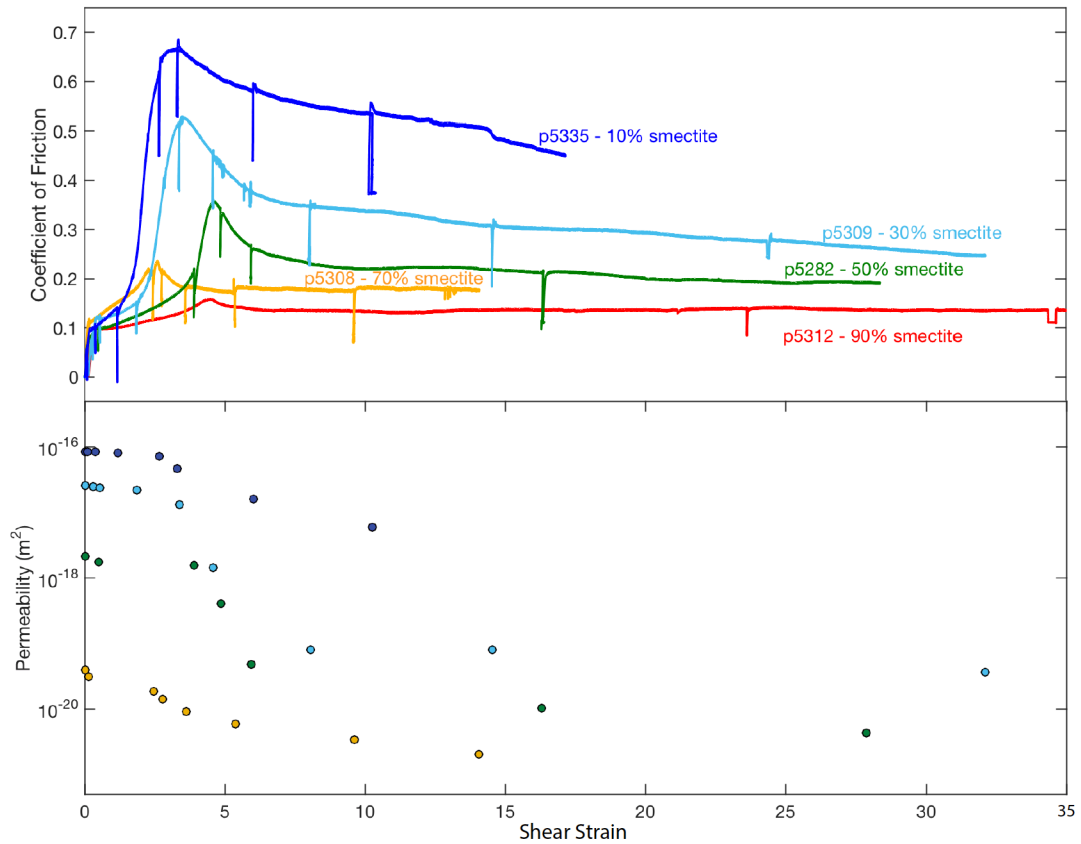


Figure 5-2: The coefficient of friction and permeability as a function of shear strain. Both the coefficient of friction and permeability decrease with increasing clay content. The coefficient of friction exhibits a local peak around a shear strain of 5, corresponding to the development of pervasive shear fabrics and then decays to a steady state value. The permeability decreases dramatically immediately after this local peak in the coefficient of friction and then also reaches a near steady state. This indicates that fabric formation is an important factor in decreasing permeability.

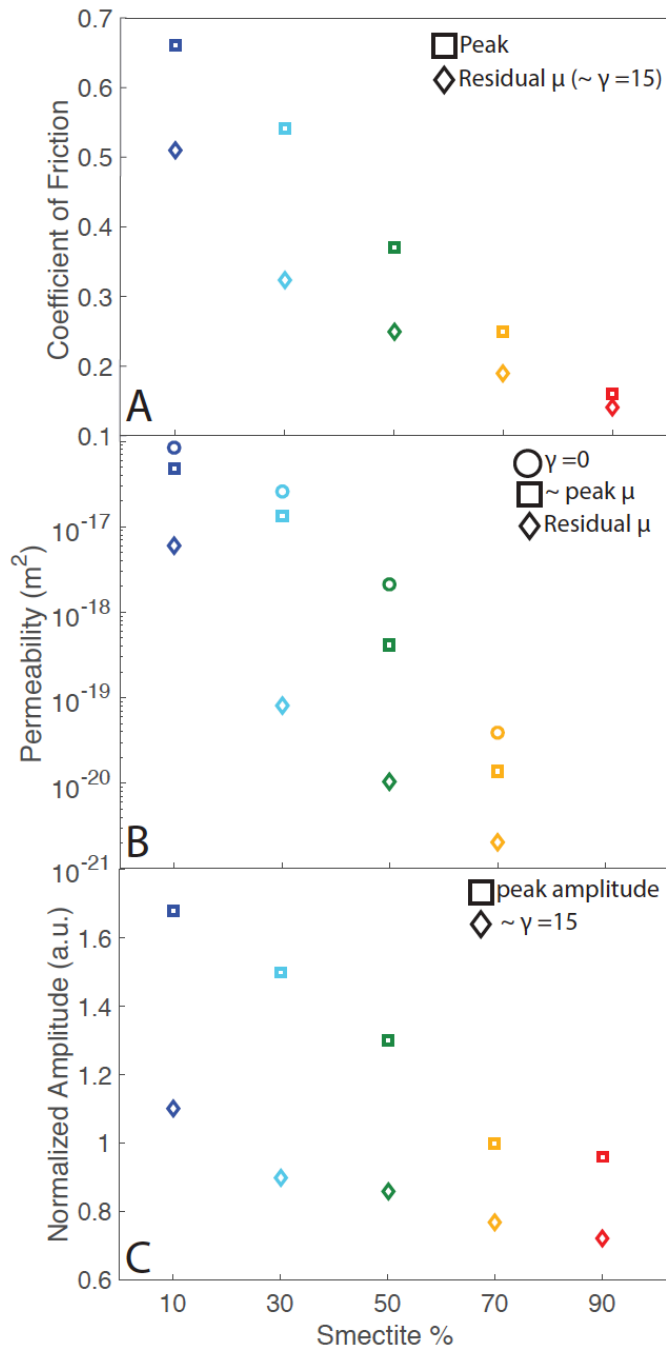


Figure 5-3: Coefficient of friction (A), permeability (B), and normalized amplitude (C), as a function of smectite in the gouge at specified shear strains values. All three variables decrease with increasing smectite content and shear strain.

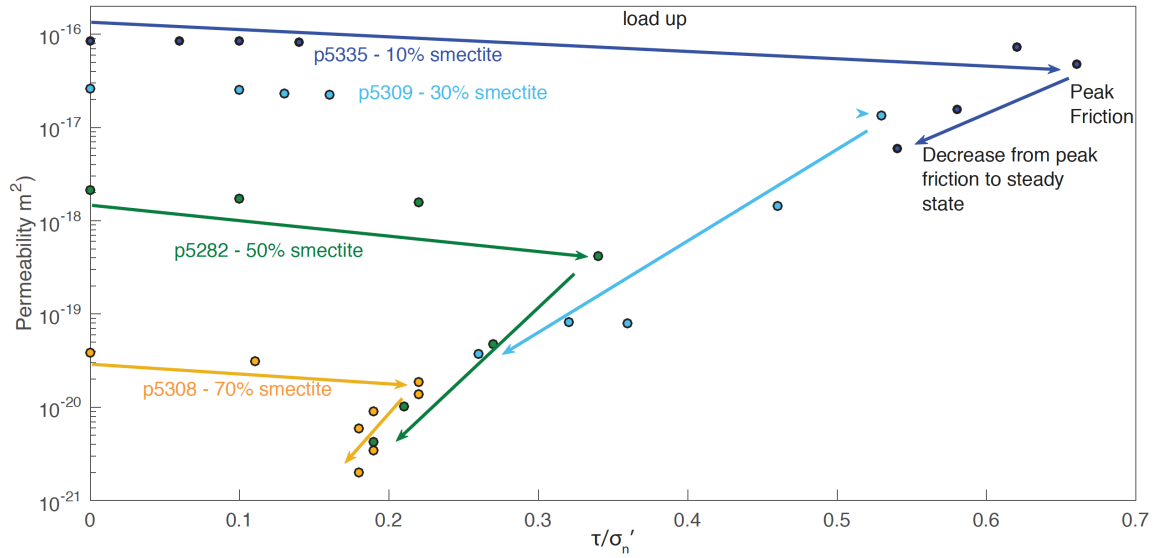


Figure 5-4: The shear stress divided by effective normal stress (our defined coefficient of friction) vs. permeability. Shear increases along the arrows. Permeability is nearly stable until peak friction where it quickly decreases.

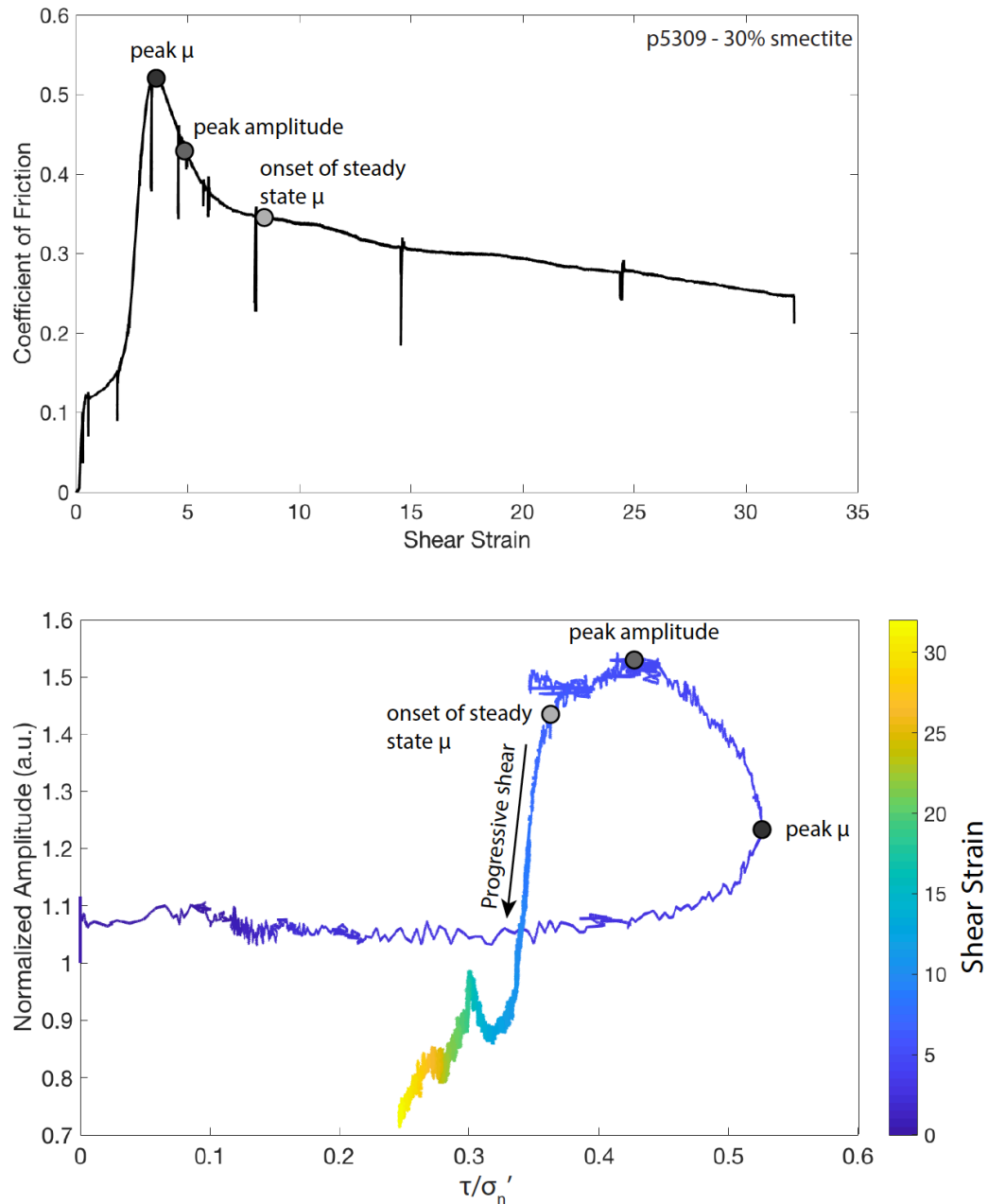


Figure 5-5: The top show shear strain vs. shear stress divided by effective normal stress (our defined coefficient of friction) and the bottom shows the coefficient of friction vs. normalized amplitude. Peak coefficient of friction (μ), peak amplitude, and the onset of steady state μ are shown on both plots with the black and gray points. The bottom plot is colored based on shear strain values. At the initiation of shear during the shear stress load up, μ is increasing whereas the amplitude is relatively stable. This is because the layer is stiffening as grains are rearranging. As shear continues and the peak μ is approached, amplitude slowly starts to increase. After peak μ , pervasive fabric formation is initiated causing a decrease in μ . However, the fabrics are not yet pervasive enough to control the amplitude as the amplitude still increases as the layer compacts (figure 5-7). As μ continues to

decrease due to continued fabric formation and evolution, amplitude finally reaches a peak as the fabrics become pervasive enough to control the response of amplitude as the fabrics are rotating near perpendicular to the direction of ultrasonic wave propagation. As the fabrics continue to evolve and rotate, the coefficient of friction reaches steady state values while the increasing complexity and geometry of the shear fabrics causes the amplitude to decrease significantly.

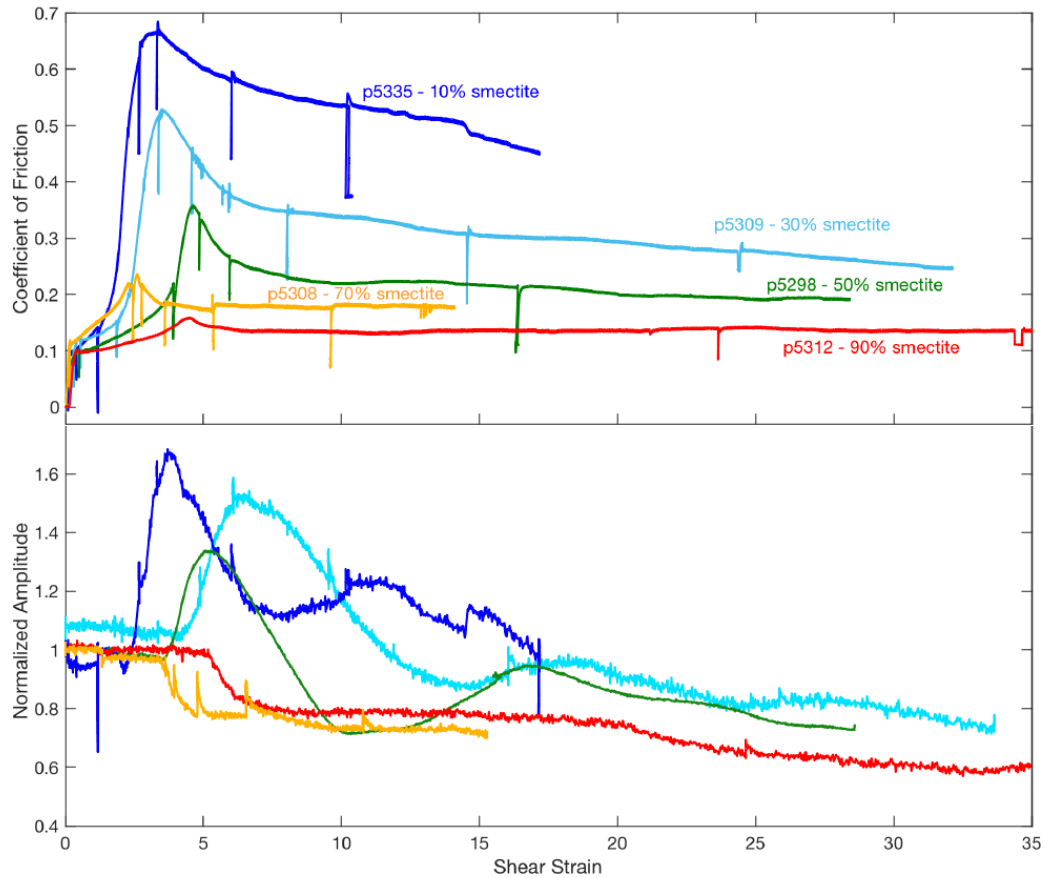


Figure 5-6: The coefficient of friction and normalized amplitude as a function of shear strain. The trend of the normalized amplitude largely mimics the coefficient of friction. However, there is a slight delay in the peak and decay of amplitude relative to the coefficient of friction as the shear fabrics become more pervasive and cause a decrease in the amplitude after the initial fabric formation which causes a decrease in the coefficient of friction. Amplitude decreases with increasing clay content. (Supplementary figure in publication draft).

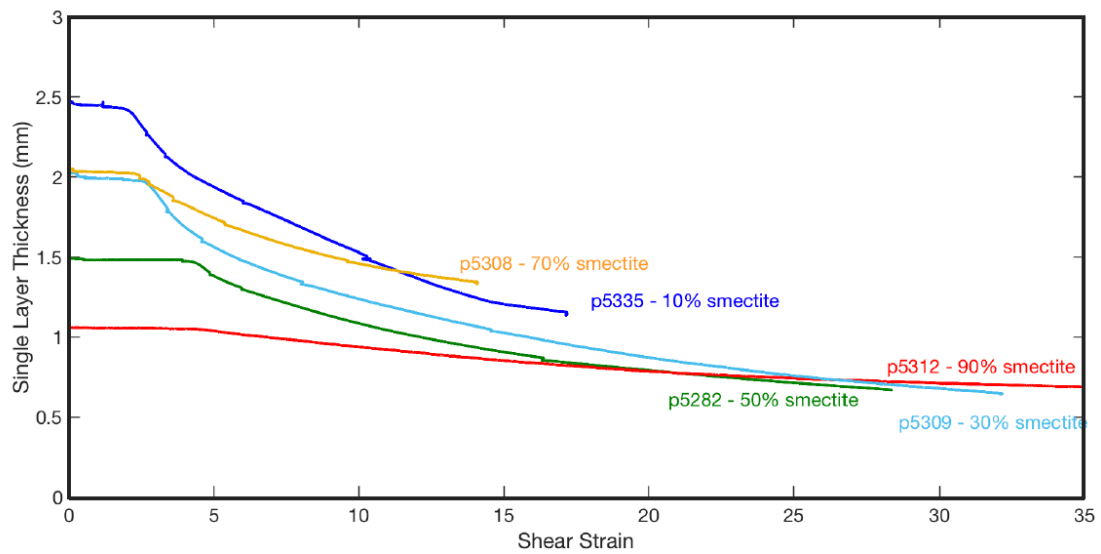


Figure 5-7: Single layer thickness in millimeters as a function of shear strain. During initial shear, layer thickness changes slowly. However, once the peak coefficient of friction is reached and fabrics form, layer thickness decreases more rapidly. (Supplementary figure in publication draft).

References

- Anthony, J.L., and Marone, C., 2005, Influence of particle characteristics on granular friction: *Journal of Geophysical Research B: Solid Earth*, v. 110, p. 1–14, doi:10.1029/2004JB003399.
- Audet, P., Bostock, M.G., Christensen, N.I., and Peacock, S.M., 2009, Seismic evidence for overpressured subducted oceanic crust and megathrust fault sealing: *Nature*, v. 457, p. 76–78, doi:10.1038/nature07650.
- Bachrach, R., Dvorkin, J., and Nur, A.M., 2000, Seismic velocities and Poisson's ratio of shallow unconsolidated sands: *Geophysics*, v. 65, p. 559–564, doi:10.1190/1.1444751.
- Bangs, N.L.B., Moore, G.F., Gulick, S.P.S., Pangborn, E.M., Tobin, H.J., Kuramoto, S., and Taira, A., 2009, Broad, weak regions of the Nankai Megathrust and implications for shallow coseismic slip: *Earth and Planetary Science Letters*, v. 284, p. 44–49, doi:10.1016/j.epsl.2009.04.026.
- Baud, P., Klein, E., and Wong, T. fong, 2004, Compaction localization in porous sandstones: Spatial evolution of damage and acoustic emission activity: *Journal of Structural Geology*, v. 26, p. 603–624, doi:10.1016/j.jsg.2003.09.002.
- Behnsen, J., and Faulkner, D.R., 2013, Permeability and frictional strength of cation-exchanged montmorillonite: *Journal of Geophysical Research: Solid Earth*, v. 118, p. 2788–2798, doi:10.1002/jgrb.50226.
- Bolton, D.C., Shokouhi, P., Rouet-Leduc, B., Hulbert, C., Rivière, J., Marone, C., and Johnson, P.A., 2019, Characterizing Acoustic Signals and Searching for Precursors during the Laboratory Seismic Cycle Using Unsupervised Machine Learning: *Seismological Research Letters*,.

- Brantut, N., Heap, M.J., Baud, P., and Meredith, P.G., 2014, Rate- and strain-dependent brittle deformation of rocks: *Journal of Geophysical Research : Solid Earth*, v. 119, p. 1818–1836, doi:10.1002/2014JB011765.Received.
- Brantut, N., Schubnel, A., Rouzaud, J.N., Brunet, F., and Shimamoto, T., 2008, High-velocity frictional properties of a clay-bearing fault gouge and implications for earthquake mechanics: *Journal of Geophysical Research: Solid Earth*, v. 113, p. 1–18, doi:10.1029/2007JB005551.
- Brenguier, F., Campillo, M., Hadziioannou, C., Shapiro, N.M., Nadeau, R.M., and Larose, E., 2008, Postseismic relaxation along the San Andreas fault at Parkfield from continuous seismological observations: *Science*, v. 321, p. 1478–1481, doi:10.1126/science.1160943.
- Browning, J., Meredith, P.G., Stuart, C.E., Healy, D., Harland, S., and Mitchell, T.M., 2017, Acoustic characterization of crack damage evolution in sandstone deformed under conventional and true triaxial loading: *Journal of Geophysical Research: Solid Earth*, v. 122, p. 4395–4412, doi:10.1002/2016JB013646.
- Budiansky, B., and O'connell, R.J., 1976, Elastic moduli of a cracked solid: *International Journal of Solids and Structures*, v. 12, p. 81–97, doi:10.1016/0020-7683(76)90044-5.
- Byerlee, J., 1990, Friction, overpressure and fault normal compression: v. 17, p. 2109–2112.
- Carpenter, B.M., Marone, C., and Saffer, D.M., 2011, Weakness of the San Andreas Fault revealed by samples from the active fault zone: *Nature Geoscience*, v. 4, p. 251–254, doi:10.1038/ngeo1089.
- Carpenter, B.M., Saffer, D.M., and Marone, C., 2012, Frictional properties and sliding stability of the San Andreas fault from deep drill core: *Geology*, v. 40, p. 759–762, doi:10.1130/G33007.1.
- Carpenter, B.M., Scuderi, M.M., Collettini, C., and Marone, C., 2014, Frictional heterogeneities on carbonate-bearing normal faults: Insights from the Monte Maggio Fault, Italy: *Journal of Geophysical Research: Solid Earth*, p. 9062–9076, doi:10.1002/2014JB011176.Received.

- Collettini, C., Viti, C., and Marone, C., 2009, Fault zone fabric and fault weakness: v. 462, doi:10.1038/nature08585.
- Crawford, B.R., Faulkner, D.R., and Rutter, E.H., 2008, Strength, porosity, and permeability development during hydrostatic and shear loading of synthetic quartz-clay fault gouge: *Journal of Geophysical Research*, v. 113, p. B03207, doi:10.1029/2006JB004634.
- David, E.C., Brantut, N., Schubnel, A., and Zimmerman, R.W., 2012, Sliding crack model for nonlinearity and hysteresis in the uniaxial stress-strain curve of rock: *International Journal of Rock Mechanics and Mining Sciences*, v. 52, p. 9–17, doi:10.1016/j.ijrmms.2012.02.001.
- Deng, X., and Underwood, M.B., 2001, Abundance of smectite and the location of a plate-boundary fault, Barbados accretionary prism: *Bulletin of the Geological Society of America*, v. 113, p. 495–507, doi:10.1130/0016-7606(2001)113<0495:AOSATL>2.0.CO;2.
- Dieterich, J.H., 1972, Time-dependent friction in rocks: *Journal of Geophysical Research* (1896-1977), v. 77, p. 3690–3697, doi:10.1029/JB077i020p03690.
- Digby, P.J., 1981, The effective elastic moduli of porous granular rocks: *Journal of Applied Mechanics*, v. 48, p. 803–808, doi:10.1115/1.3157738.
- Durán, E.L., Adam, L., and Wallis, I.C., 2018, A robust methodology for time picking and error analysis of ultrasonic waveforms and rock densities in the laboratory: *GEOPHYSICS*, v. 84, p. MR85–MR97, doi:10.1190/geo2018-0331.1.
- Dvorkin, J., Prasad, M., Sakai, A., and Lavoie, D., 1999, Elasticity of marine sediments: Rock physics modeling: *Journal of Geophysical Research*, v. 26, p. 1781–1784.
- Ellsworth, W.L., 2013, Injection-Induced Earthquakes: *Science*, v. 341, p. 250–260, doi:10.1785/gssrl.83.2.250.
- van der Elst, N.J., Savage, H.M., Keranen, K.M., and Abers, G.A., 2013, Enhanced remote

- earthquake triggering at fluid-injection sites in the midwestern United States: *Science*, v. 341, p. 164–167, doi:10.1126/science.1112699.
- Elsworth, D., Spiers, C.J., and Niemeijer, A.R., 2016, Understanding induced seismicity: *Science*, v. 354, p. 1380–1381, doi:10.1126/science.aal2584.
- Erguler, Z.A., and Ulusay, R., 2009, Water-induced variations in mechanical properties of clay-bearing rocks: *International Journal of Rock Mechanics and Mining Sciences*, v. 46, p. 355–370, doi:10.1016/j.ijrmms.2008.07.002.
- Eshelby, J.D., 1961, Elastic Inclusions and Inhomogeneities, *in Progress in Solid Mechanics*, p. Vol. 2.
- Eshelby, J.D., 1957, The Determination of the Elastic Field of an Ellipsoidal Inclusion, and Related Problems: *Proceedings of the Royal Society A: Mathematical, Physical and Engineering Sciences*, v. 241, p. 376–396, doi:10.1098/rspa.1957.0133.
- Eshelby, J.D., 1963, The Distribution of Dislocations in an Elliptical Glide Zone: *Physica Status Solidi*, v. 3, p. 2057–2060, doi:10.1046/j.1365-8711.2000.03496.x.
- Faulkner, D.R., Jackson, C. a. L., Lunn, R.J., Schlische, R.W., Shipton, Z.K., Wibberley, C. a. J., and Withjack, M.O., 2010, A review of recent developments concerning the structure, mechanics and fluid flow properties of fault zones: *Journal of Structural Geology*, v. 32, p. 1557–1575, doi:10.1016/j.jsg.2010.06.009.
- Faulkner, D.R., Lewis, A.C., and Rutter, E.H., 2003, On the internal structure and mechanics of large strike-slip fault zones: Field observations of the Carboneras fault in southeastern Spain: *Tectonophysics*, v. 367, p. 235–251, doi:10.1016/S0040-1951(03)00134-3.
- Faulkner, D.R., and Rutter, E.H., 2001, Can the maintenance of overpressured fluids in large strike-slip fault zones explain their apparent weakness? *Geology*, v. 29, p. 503–506, doi:10.1130/0091-7613(2001)029<0503:CTMOOF>2.0.CO;2.

- Faulkner, D.R., and Rutter, E.H., 2003, The effect of temperature, the nature of the pore fluid, and subyield differential stress on the permeability of phyllosilicate-rich fault gouge: *Journal of Geophysical Research: Solid Earth*, v. 108, p. 1–12, doi:10.1029/2001jb001581.
- Fortin, J., Guéguen, Y., and Schubnel, A., 2007, Effects of pore collapse and grain crushing on ultrasonic velocities and V_p/V_s : *Journal of Geophysical Research: Solid Earth*, v. 112, p. 1–16, doi:10.1029/2005JB004005.
- Fortin, J., Schubnel, A., and Guéguen, Y., 2005, Elastic wave velocities and permeability evolution during compaction of Bleurswiller sandstone: *International Journal of Rock Mechanics and Mining Sciences*, v. 42, p. 873–889, doi:10.1016/j.ijrmms.2005.05.002.
- Garia, S., Pal, A.K., Ravi, K., and Nair, A.M., 2019, A comprehensive analysis on the relationships between elastic wave velocities and petrophysical properties of sedimentary rocks based on laboratory measurements: *Journal of Petroleum Exploration and Production Technology*, doi:10.1007/s13202-019-0675-0.
- Gettemy, G.L., Tobin, H.J., Hole, J.A., and Sayed, A.Y., 2004, Multi-scale compressional wave velocity structure of the San Gregorio Fault zone: *Geophysical Research Letters*, v. 31, p. L06601, doi:10.1029/2003GL018826.
- Goldsby, D.L., and Kohlstedt, D.L., 2001, Superplastic deformation of ice: Experimental observations: *Journal of Geophysical Research: Solid Earth*, v. 106, p. 11017–11030, doi:10.1029/2000jb900336.
- Hadley, K., 1976, Comparison of calculated and observed crack densities and seismic velocities in westerly granite: *Journal of Geophysical Research*, v. 81.
- Haines, S.H., Kaproth, B., Marone, C., Saffer, D., and van der Pluijm, B., 2013, Shear zones in clay-rich fault gouge: A laboratory study of fabric development and evolution: *Journal of Structural Geology*, v. 51, p. 206–225, doi:10.1016/j.jsg.2013.01.002.
- Haines, S.H., van der Pluijm, B. a., Ikari, M.J., Saffer, D.M., and Marone, C., 2009, Clay fabric intensity in natural and artificial fault gouges: Implications for brittle fault zone processes

and sedimentary basin clay fabric evolution: *Journal of Geophysical Research*, v. 114, p. B05406, doi:10.1029/2008JB005866.

den Hartog, S.A.M., Niemeijer, A.R., and Spiers, C.J., 2012, New constraints on megathrust slip stability under subduction zone P-T conditions: *Earth and Planetary Science Letters*, v. 353–354, p. 240–252, doi:10.1016/j.epsl.2012.08.022.

Heap, M.J., Brantut, N., Baud, P., and Meredith, P.G., 2015, Time-dependent compaction band formation in sandstone: *Journal of Geophysical Research: Solid Earth*, v. 120, p. 4808–4830, doi:10.1002/2015JB012022.

Hubbert, M.K., and Rubey, W.W., 1959, Role of Fluid Pressure in Mechanics of Overthrust Faulting: *GSA Bulletin*, v. 70, p. 115–166, doi:10.1130/0016-7606(1959)70[115:rofpim]2.0.co;2.

Hudson, J.A., 1986, A higher-order approximation to the wave propagation constants for a cracked solid: *Geophysical Journal of the Royal Astronomical Society*, v. 87, p. 265–274, <http://ezaccess.libraries.psu.edu/login?url=http://search.ebscohost.com/login.aspx?direct=true&db=geh&AN=1987-021088&site=ehost-live&scope=site>.

Hüpers, A. et al., 2017, Release of mineral-bound water prior to subduction tied to shallow seismogenic slip off Sumatra: *Science*, v. 356, p. 841 LP – 844, <http://science.sciencemag.org/content/356/6340/841.abstract>.

Ikari, M.J., Marone, C., and Saffer, D.M., 2011, On the relation between fault strength and frictional stability: *Geology*, v. 39, p. 83–86, doi:10.1130/G31416.1.

Ikari, M.J., Niemeijer, A.R., and Marone, C., 2015, Experimental investigation of incipient shear failure in foliated rock: *Journal of Structural Geology*, v. 77, p. 82–91, doi:10.1016/j.jsg.2015.05.012.

Ikari, M.J., and Saffer, D.M., 2012, Permeability contrasts between sheared and normally consolidated sediments in the Nankai accretionary prism: *Marine Geology*, v. 295–298, p. 1–13, doi:10.1016/j.margeo.2011.11.006.

- Ikari, M.J., Saffer, D.M., and Marone, C., 2007, Effect of hydration state on the frictional properties of montmorillonite-based fault gouge: *Journal of Geophysical Research: Solid Earth*, v. 112, p. 1–12, doi:10.1029/2006JB004748.
- Ikari, M.J., Saffer, D.M., and Marone, C., 2009, Frictional and hydrologic properties of clay-rich fault gouge: *Journal of Geophysical Research*, v. 114, p. B05409, doi:10.1029/2008JB006089.
- Jefferies, S.P., Holdsworth, R.E., Wibberley, C.A.J., Shimamoto, T., Spiers, C.J., Niemeijer, A.R., and Lloyd, G.E., 2006, The nature and importance of phyllonite development in crustal-scale fault cores: An example from the Median Tectonic Line, Japan: *Journal of Structural Geology*, v. 28, p. 220–235, doi:10.1016/j.jsg.2005.10.008.
- Jia, X., Caroli, C., and Velicky, B., 1999, Ultrasound propagation in externally stressed granular media: *Physical Review Letters*, v. 82, p. 1863–1866, doi:10.1103/PhysRevLett.82.1863.
- Kaproth, B.M., Kacwicz, M., Muhuri, S., and Marone, C., 2016, Permeability and frictional properties of halite-clay-quartz faults in marine-sediment: The role of compaction and shear: *Marine and Petroleum Geology*, v. 78, p. 222–235, doi:10.1016/j.marpetgeo.2016.09.011.
- Kaproth, B., and Marone, C., 2014, Evolution of elastic wave speed during shear-induced damage and healing within laboratory fault zones: *Journal of Geophysical Research: Solid Earth*, v. 119, p. 4821–4840, doi:10.1002/2013JB010639.Received.
- Kenigsberg, A.R., Rivière, J., Marone, C., and Saffer, D.M., 2019a, Evolution of Elastic and Mechanical Properties during Fault Shear: The Roles of Clay Content, Fabric Development, and Porosity:
- Kenigsberg, A.R., Rivière, J., Marone, C., and Saffer, D.M., 2019b, The Effects of Shear Strain, Fabric, and Porosity Evolution on Elastic and Mechanical Properties of Clay-Rich Fault Gouge.:
- Khidas, Y., and Jia, X., 2012, Probing the shear-band formation in granular media with sound waves: *Physical Review E - Statistical, Nonlinear, and Soft Matter Physics*, v. 85, p. 1–6,

doi:10.1103/PhysRevE.85.051302.

Kilgore, B., Beeler, N.M., Lozos, J., and Oglesby, D., 2017, Rock friction under variable normal stress: *Journal of Geophysical Research: Solid Earth*, v. 122, p. 7042–7075, doi:10.1002/2017JB014049.

Knipe, R.J., 1992, Faulting processes and fault seal, *in* Larsen, R.M., Brekke, H., Larsen, B.T., and Talleraas, E.B.T.-S. and T.M. and its A. to P.G. eds., *Norwegian Petroleum Society Special Publications*, Amsterdam, Elsevier, v. 1, p. 325–342, doi:<https://doi.org/10.1016/B978-0-444-88607-1.50027-9>.

Knuth, M., and Marone, C., 2007, Friction of sheared granular layers: Role of particle dimensionality, surface roughness, and material properties: *Geochemistry, Geophysics, Geosystems*, v. 8, doi:10.1029/2006GC001327.

Knuth, M.W., Tobin, H.J., and Marone, C., 2013, Evolution of ultrasonic velocity and dynamic elastic moduli with shear strain in granular layers: *Granular Matter*, v. 15, p. 499–515, doi:10.1007/s10035-013-0420-1.

Kopf, A., and Brown, K.M., 2003, Friction experiments on saturated sediments and their implications for the stress state of the Nankai and Barbados subduction thrusts: *Marine Geology*, v. 202, p. 193–210, doi:10.1016/S0025-3227(03)00286-X.

Lauer, R.M., Saffer, D.M., and Harris, R.N., 2017, Links between clay transformation and earthquakes along the Costa Rican subduction margin: *Geophysical Research Letters*, v. 44, p. 7725–7732, doi:10.1002/2017GL073744.

Leeman, J.R., Marone, C., and Saffer, D.M., 2018, Frictional Mechanics of Slow Earthquakes: *Journal of Geophysical Research: Solid Earth*, v. 123, p. 7931–7949, doi:10.1029/2018JB015768.

Leeman, J.R., Saffer, D.M., Scuderi, M.M., and Marone, C., 2016, Laboratory observations of slow earthquakes and the spectrum of tectonic fault slip modes: *Nature Communications*, v. 7, p. 1–6, doi:10.1016/0360-3016(81)90183-8.

- Leeman, J., Scuderi, M.M., Marone, C., and Saffer, D., 2015, Stiffness evolution of granular layers and the origin of repetitive, slow, stick-slip frictional sliding: *Granular Matter*, v. 17, p. 447–457, doi:10.1007/s10035-015-0565-1.
- Li, J., Shillington, D.J., Bécel, A., Nedimović, M.R., Webb, S.C., Saffer, D.M., Keranen, K.M., and Kuehn, H., 2015, Dondip variations in seismic reflection character: Implications for fault structure and seismogenic behavior in the Alaska subduction zone: *Journal of Geophysical Research: Solid Earth*, v. 120, p. 7883–7904, doi:10.1002/2015JB012455.Received.
- Li, Y., and Vidale, J.E., 2001, Healing of the shallow fault zone from 1994-1998 after the 1992 M7.5 Landers, California, earthquake: *Geophysical Research Letters*, v. 28, p. 2999–3002.
- Li, Y., Vidale, J.E., Aki, K., Xu, F., and Burdette, T., 1998, Evidence of Shallow Fault Zone Strengthening After the 1992 M 7 . 5 Landers , California , Earthquake: *Science*, v. 217–220, p. 1996–1999.
- Li, Y.G., Vidale, J.E., and Cochran, E.S., 2004, Low-velocity damaged structure of the San Andreas Fault at Parkfield from fault zone trapped waves: *Geophysical Research Letters*, v. 31, p. 1–5, doi:10.1029/2003GL019044.
- Lockner, D.A., Morrow, C., Moore, D., and Hickman, S., 2011, Low strength of deep San Andreas fault gouge from SAFOD core: *Nature*, v. 472, p. 82, <https://doi.org/10.1038/nature09927>.
- Logan, J., Dengo, C., Higgs, N., Wang, Z.-Z., 1992, Fabrics of Experimental Fault Zones: Their Development and Relationship to Mechanical Behavior: *Fault Mechanics and Transport Properties of Rocks*, v. 51, p. 33–67.
- Logan, J.M., Friedman, M., Higgs, N., Dengo, C., and Shimamoto, T., 1979, Experimental studies of simulated gouge and their application to studies of natural fault gouges: *Analysis of Actual Fault Zones in Bedrock*,.
- Logan, J.M., and Rauenzahn, K.A., 1987, Frictional dependence of gouge mixtures of quartz and

montmorillonite on velocity, composition and fabric: *Tectonophysics*, v. 144, p. 87–108, doi:10.1016/0040-1951(87)90010-2.

Mair, K., and Marone, C., 1999, Friction of simulated fault gouge for a wide range of velocities and normal stresses: *Journal of Geophysical Research*, v. 104, p. 28899–28914.

Marone, C., 1998, Laboratory-Derived Friction Laws and Their Application To Seismic Faulting: *Annual Review of Earth and Planetary Sciences*, v. 26, p. 643–696, doi:10.1146/annurev.earth.26.1.643.

Mavko, G., Mukerji, T., and Dvorkin, J., 2009, *The Rock Physics Handbook: Tools for Seismic Analysis of Porous Media*: Cambridge University Press.

Mavko, G., and Nur, A., 1979, Wave attenuation in partially saturated rocks: *Geophysics*, v. 44, p. 161–178.

McGarr, A. et al., 2015, Coping with earthquakes induced by fluid injection: *Science*, v. 347, p. 830–831, doi:10.1126/science.aaa0494.

McNeill, L.C., Dugan, B., Petronotis, K.E., and 362, S.E., 2017, *Sumatra Subduction Zone: Proceedings of the International Ocean Discovery Program, 362*: College Station, TX (International Ocean Discovery Program), v. 362.

Mooney, W.D., and Ginzburg, A., 1986, Seismic Measurements of the Internal Properties of Fault Zones: *PAGEOPH*, v. 124.

Moore, D.E., and Lockner, D. a., 2004, Crystallographic controls on the frictional behavior of dry and water-saturated sheet structure minerals: *Journal of Geophysical Research*, v. 109, p. B03401, doi:10.1029/2003JB002582.

Moore, J.C., and Saffer, D., 2001, Updip limit of the seismogenic zone beneath the accretionary prism of Southwest Japan: An effect of diagenetic to low-grade metamorphic processes and

increasing effective stress: *Geology*, v. 29, p. 183–186, doi:10.1130/0091-7613(2001)029<0183:ULOTSZ>2.0.CO;2.

Moore, D., Summers, R., and Byerlee, J., 1989, Sliding behavior and deformation textures of heated illite gouge: *Journal of Structural Geology*, v. 11, p. 329–342, doi:[https://doi.org/10.1016/0191-8141\(89\)90072-2](https://doi.org/10.1016/0191-8141(89)90072-2).

Morrow, C.A., Moore, D.E., and Lockner, D.A., 2017, Frictional strength of wet and dry montmorillonite: *Journal of Geophysical Research: Solid Earth*, v. 122, p. 3392–3409, doi:10.1002/2016JB013658.

Morrow, C. a., Shi, L.Q., and Byerlee, J.D., 1984, Permeability of fault gouge under confining pressure and shear stress: *Journal of Geophysical Research*, v. 89, p. 3193, doi:10.1029/JB089iB05p03193.

Niemeijer, A., Marone, C., and Elsworth, D., 2010, Fabric induced weakness of tectonic faults: *Geophysical Research Letters*, v. 37, p. n/a-n/a, doi:10.1029/2009GL041689.

Nur, A., Mavko, G., Dvorkin, J., and Galmudi, D., 1998, Critical porosity : A key to relating physical properties to porosity in rocks: *The leading edge*, v. 17, p. 357–362.

Popp, T., and Kern, H., 1998, Ultrasonic wave velocities, gas permeability and porosity in natural and granular rock salt: *Physics and Chemistry of the Earth*, v. 23, p. 373–378, doi:10.1016/S0079-1946(98)00040-8.

Rice, J.R., 1992, Fault stress states, pore pressure distributions, and the weakness of the San Andreas Fault, *in* *Fault Mechanics and Transport Properties of Rocks*, p. 475–503.

Rivière, J., Lv, Z., Johnson, P.A., and Marone, C., 2018, Evolution of b-value during the seismic cycle: Insights from laboratory experiments on simulated faults: *Earth and Planetary Science Letters*, v. 482, p. 407–413, doi:10.1016/j.epsl.2017.11.036.

- Rivière, J., Pimienta, L., Scuderi, M., Candela, T., Shokouhi, P., Fortin, J., Schubnel, A., Marone, C., and Johnson, P.A., 2016, Frequency, pressure, and strain dependence of nonlinear elasticity in Berea Sandstone: *Geophysical Research Letters*, v. 43, p. 3226–3236, doi:10.1002/2016GL068061.
- Rosenberger, K., McNamara, K., Underwood, M.B., and Vrolijk, P., 2019, Data Report: clay mineral assemblages in the Sumatra Seismogenic Zone, IODP Sites U1480 and U1481: In prep.,.
- Ryan, K.L., Rivière, J., and Marone, C., 2018, The Role of Shear Stress in Fault Healing and Frictional Aging: *Journal of Geophysical Research: Solid Earth*, v. 123, p. 10,479–10,495, doi:10.1029/2018JB016296.
- Saffer, D.M., Frye, K.M., Marone, C., and Mair, K., 2001, Laboratory results indicating complex and potentially unstable frictional behavior of smectite clay: *Geophysical Research Letters*, v. 28, p. 2297–2300, doi:10.1029/2001GL012869.
- Saffer, D.M., and Marone, C., 2003, Comparison of smectite- and illite-rich gouge frictional properties: Application to the updip limit of the seismogenic zone along subduction megathrusts: *Earth and Planetary Science Letters*, v. 215, p. 219–235, doi:10.1016/S0012-821X(03)00424-2.
- Samuelson, J., Elsworth, D., and Marone, C., 2009, Shear-induced dilatancy of fluid-saturated faults: Experiment and theory: *Journal of Geophysical Research: Solid Earth*, v. 114, p. 1–15, doi:10.1029/2008JB006273.
- Savage, H.M., Rabinowitz, H.S., Spagnuolo, E., Aretusini, S., Polissar, P.J., and Di Toro, G., 2018, Biomarker thermal maturity experiments at earthquake slip rates: *Earth and Planetary Science Letters*, v. 502, p. 253–261, doi:10.1016/j.epsl.2018.08.038.
- Schleicher, A.M., Van Der Pluijm, B.A., Solum, J.G., and Warr, L.N., 2006, Origin and significance of clay-coated fractures in mudrock fragments of the SAFOD borehole (Parkfield, California): *Geophysical Research Letters*, v. 33, p. 1–5, doi:10.1029/2006GL026505.

- Scholz, C.H., 2002, *The mechanics of earthquakes and faulting*: Cambridge University Press, 508 p.
- Schubnel, A., Nishizawa, O., Masuda, K., Lei, X., Xue, Z., and Guéguen, Y., 2003, Velocity measurements and crack density determination during wet triaxial experiments on Oshima and Toki granites: *Pure and Applied Geophysics*, v. 160, p. 869–887, doi:10.1007/pl00012570.
- Scott, T.E., Ma, Q., and Roegiers, J.C., 1993, Acoustic velocity changes during shear enhanced compaction of sandstone: *International Journal of Rock Mechanics and Mining Sciences and*, v. 30, p. 763–769, doi:10.1016/0148-9062(93)90020-E.
- Scott, D.R., Marone, C.J., and Sammis, C.G., 1994, The apparent friction of granular fault gouge in sheared layers: *Journal of Geophysical Research*, v. 99, p. 7231–7246.
- Scuderi, M.M., Collettini, C., Viti, C., Tinti, E., and Marone, C., 2017, Evolution of shear fabric in granular fault gouge from stable sliding to stick slip and implications for fault slip mode: *Geology*, v. 45, p. 731–734, doi:10.1130/G39033.1.
- Segall, P., and Lu, S., 2015, Injection-induced seismicity : Poroelastic and earthquake nucleation effects: *Journal of Geophysical Research: Solid Earth*, v. 120, p. 5082–5103, doi:10.1002/2015JB012060.Received.
- Segall, P., and Rice, J.R., 2006, Does shear heating of pore fluid contribute to earthquake nucleation? *Journal of Geophysical Research: Solid Earth*, v. 111, p. 1–17, doi:10.1029/2005JB004129.
- Shreedharan, S., Rivière, J., Bhattacharya, P., and Marone, C., 2019, Frictional State Evolution during Normal Stress Perturbations Probed with Ultrasonic Waves: *Journal of Geophysical Research: Solid Earth*, v. 124, doi:10.1029/2018JB016885.
- Sisbon, R.H., 1977, Fault rocks and fault mechanisms: *Journal of the Geological Society*, v. 133, p. 191, doi:10.1144/gsjgs.133.3.0191.

- Sleep, N.H., and Blanpied, M.L., 1992, Creep, compaction and the weak rheology of major faults: *Nature*, v. 359, p. 687–692, doi:10.1038/359687a0.
- Summers, R., and Byerlee, J., 1977, A Note on the Effect of Fault Gouge Composition on the Stability of Frictional Sliding: v. 14, p. 155–160.
- Tembe, S., Lockner, D. a., and Wong, T.-F., 2010, Effect of clay content and mineralogy on frictional sliding behavior of simulated gouges: Binary and ternary mixtures of quartz, illite, and montmorillonite: *Journal of Geophysical Research*, v. 115, p. B03416, doi:10.1029/2009JB006383.
- Di Toro, G., Goldsby, D.L., and Tullis, T.E., 2004, Friction falls towards zero in quartz rock as slip velocity approaches seismic rates: *Nature*, v. 427, p. 436–439, doi:10.1038/nature02249.
- Tudge, J., and Tobin, H.J., 2013, Velocity-porosity relationships in smectite-rich sediments: Shikoku Basin, Japan: *Geochemistry, Geophysics, Geosystems*, v. 14, p. 5194–5207, doi:10.1002/2013GC004974.
- Tullis, T.E., 1996, Rock friction and its implications for earthquake prediction examined via models of Parkfield earthquakes: *Proceedings of the National Academy of Sciences of the United States of America*, v. 93, p. 3803–3810.
- Ujiie, K. et al., 2013, Low Coseismic Shear Stress on the Tohoku-Oki Megathrust Determined from Laboratory Experiments: *Science*, v. 342, p. 1211–1214, doi:10.1126/science.1243485.
- Unsworth, M., and Bedrosian, P.A., 2004, Electrical resistivity structure at the SAFOD site from magnetotelluric exploration: *Geophysical Research Letters*, v. 31, p. 10–13, doi:10.12693/AGU133.704.
- Uyanık, O., Sabbağ, N., Uyanık, N.A., and Öncü, Z., 2019, Prediction of mechanical and physical properties of some sedimentary rocks from ultrasonic velocities: *Bulletin of Engineering Geology and the Environment*, doi:10.1007/s10064-019-01501-6.

- Vrolijk, P., and van der Pluijm, B. a., 1999, Clay gouge: *Journal of Structural Geology*, v. 21, p. 1039–1048, doi:10.1016/S0191-8141(99)00103-0.
- Vrolijk, P.J., Urai, J.L., and Kettermann, M., 2016, Clay smear: Review of mechanisms and applications: *Journal of Structural Geology*, v. 86, p. 95–152, doi:10.1016/j.jsg.2015.09.006.
- Walsh, F.R., and Zoback, M.D., 2015, Oklahoma's recent earthquakes and saltwater disposal: *Science Advances*, v. 1, p. e1500195–e1500195, doi:10.1126/sciadv.1500195.
- Wang, C., Mao, N., and Wu, F.T., 1980, Mechanical properties of clays at high pressure: *Journal of Geophysical Research*, v. 85, p. 1462–1468.
- Wibberley, C.A.J., and Shimamoto, T., 2005, Earthquake slip weakening and asperities explained by thermal pressurization: *Nature*, v. 436, p. 689–692, doi:10.1038/nature03901.
- Wibberley, C.A.J., and Shimamoto, T., 2003, Internal structure and permeability of major strike-slip fault zones: the Median Tectonic Line in Mie Prefecture, Southwest Japan: *Journal of str.*, v. 25, p. 59–78, doi:10.1016/S0191-8141(02)00014-7.
- Wojatschke, J., Scuderi, M.M., Warr, L.N., Carpenter, B.M., Saffer, D., and Marone, C., 2016, Experimental constraints on the relationship between clay abundance, clay fabric, and frictional behavior for the Central Deforming Zone of the San Andreas Fault: *Geochemistry Geophysics Geosystems*, v. 17, p. 3865–3881, doi:10.1002/2016GC006406.
- Wu, F.T., 1978, Mineralogy and Physical Nature of Clay Gouge: *Pure and Applied Geophysics PAGEOPH*, v. 116, p. 655–689.
- Wu, F.T., Blatter, L., and Roberson, H., 1975, Clay Gouges in the San Andreas Fault System and their Possible Implications: *Pure and Applied Geophysics PAGEOPH*, v. 113, p. 8795.
- Yielding, G., Freeman, B., and Needham, D.T., 1997, Quantitative fault seal prediction: *AAPG Bulletin*, v. 81, p. 897–917.

Zhang, J., Wong, T.-F., and Davis, D.M., 1990, Micromechanics of pressure-induced grain crushing in porous rocks: *Journal of Geophysical Research*, v. 95, p. 341, doi:10.1029/jb095ib01p00341.

VITA

Abby Kenigsberg

EDUCATION

Ph. D. Geosciences, The Pennsylvania State University, 2019

B.S. General Geology, The University of Texas at Austin, 2014

RESEARCH AND PROFESSIONAL EXPERIENCE

Chevron Earth Science Intern, Upstream Capabilities, Drilling and Completions, G&G Ops Technical Assurance Team, May 2018 – August 2018

Structural Geologist, International Ocean Discovery Program (IODP) Expedition 362, August 2016 – October 2016

Research Assistant, The Pennsylvania State University, 2015 – 2019

Teaching Assistant, Physical Geology and Natural Disasters, Pennsylvania State University, 2014 – 2018

Officer for Association for Women Geoscientists (AWG) Penn State Student Chapter

President, 2016 – 2018 and Secretary, 2015 - 2016 and 2018 - 2019

HONORS AND AWARDS

Penn State Geosciences Graduate Colloquium, 1st Place Energy Related Presentation, 2019

Penn State Geosciences Graduate Colloquium, 1st Pre-Comps. Exam Oral Presentation, 2018

GDL Foundation Fellowship, June 2016

Shell Geosciences Energy Facilitation Award, Penn State, May 2015, 2016, 2017, and 2018

Post Expedition Award, U.S. Science Support Program, NSF, January 2017

ConocoPhillips Graduate Fellowship, Penn State, August 2015 – May 2016

Chevron Graduate Student Scholarship, Penn State, December 2014 and 2015

Geological Society of America Graduate Research Grant, April 2015

PUBLICATIONS

Kenigsberg, A. R., Jacques Rivière, Chris Marone, Demian M. Saffer, The Effects of Shear Strain, Fabric, and Porosity Evolution on Elastic and Mechanical Properties of Clay-Rich Fault Gouge, Submitted to Journal of Geophysical Research (in revision)

Kenigsberg, A. R., Jacques Rivière, Chris Marone, Demian M. Saffer, A Method for Travel Time Calibration and Determination of Absolute Ultrasonic Velocities in Experimental Shear Zones, Submitted to the International Journal of Rock Mechanics and Mining Sciences (under review)

Kenigsberg, A. R., Jacques Rivière, Chris Marone, Demian M. Saffer, Evolution of Elastic and Mechanical Properties during Fault Shear: The Roles of Clay Content, Fabric Development, and Porosity (in prep.)

Hüpers, A., (32 others including **Kenigsberg, A. R.**) (2017) Release of mineral-bound water prior to subduction tied to shallow seismogenic slip off Sumatra, *Science*, Vol. 356, Issue 6340, pp. 841-844, DOI: 10.1126/science.aal3429

Lisa C. McNeill, Brandon Dugan, (33 others including **Kenigsberg, A. R.**) (2017) Understanding Himalayan erosion and the significance of the Nicobar Fan, *Earth and Planetary Science Letters*, Vol. 475, Pages 134-142, ISSN 0012-821X, <http://dx.doi.org/10.1016/j.epsl.2017.07.019>.